

Massively Parallel Optical Manipulation of Single Cells, Micro- and Nano-particles on
Optoelectronic Devices

by

Pei-Yu Chiou

B.S. (National Taiwan University) 1998
M.S. (University of California at Los Angeles) 2004

A dissertation submitted in partial satisfaction of the
requirement for the degree of

Doctor of Philosophy

in

Engineering-Electrical Engineering and Computer Sciences

in the

GRADUATION DIVISION

of the

UNIVERSITY OF CALIFORNIA AT BERKELEY

Committee in charge:

Professor Ming C. Wu, chair
Professor Connie J. Chang-Hasnain
Professor Luke P. Lee

Fall 2005

The dissertation of Pei-Yu Chiou is approved:

Professor Ming C. Wu, Chair Date

Professor Connie J. Chang-Hasnain Date

Professor Luke P. Lee Date

University of California, Berkeley

Fall 2005

Massively Parallel Optical Manipulation of Single Cells, Micro- and Nano-particles on
Optoelectronic Devices

Copyright © 2005

by

Pei-Yu Chiou

Abstract

Massively Parallel Optical Manipulation of Single Cells, Micro- and Nano-particles on Optoelectronic Devices

by

Pei-Yu Chiou

Doctor of Philosophy in Electrical Engineering and Computer Sciences

University of California, Berkeley

Professor Ming C. Wu, chair

The ability to manipulate biological cells and micrometer-scale particles plays an important role in many biological and colloidal science applications. However, conventional manipulation techniques, such as optical tweezers, electrokinetic forces (electrophoresis, dielectrophoresis (DEP), and traveling-wave dielectrophoresis), magnetic tweezers, acoustic traps, and hydrodynamic flows, cannot achieve high resolution and high throughput at the same time. Optical tweezers offers high resolution for trapping single particles, but has a limited manipulation area due to tight focusing requirements, while electrokinetic forces and other mechanisms provide high throughput, but lack the flexibility or the spatial resolution necessary for controlling individual particles.

In the dissertation, I present a novel concept called optoelectronic tweezers (OET).

Using light-driven electrokinetic mechanisms (dielectrophoresis, ac electroosmosis),

OET permits high-resolution patterning of electric fields on a photoconductive surface for manipulating single cells, micro- and nano-particles with light intensity of 10 nW/cm^2 ,

which is 100,000 times less than with optical tweezers. It opens up the possibility of optical manipulation using an incoherent light source such as light emitting diode (LED) or a halogen lamp. Integrating with a digital micromirror or a liquid crystal spatial light modulator, we have demonstrated parallel manipulation of 31,000 particle traps on a $1.3 \times 1.0 \text{ mm}^2$ area. Using OET technique, we have demonstrated optical manipulation on various polystyrene particles with size range from $45 \text{ }\mu\text{m}$ to 500 nm , bacteria (*E. Coli*), cancer cells (HeLa), and human white blood and red blood cells. With direct optical imaging control, multiple manipulation functions can be combined to achieve complex, multi-step manipulation protocols.

Professor Ming C. Wu, Chair

Date

To my parent

TABLE OF CONTENTS

Chapter 1

Introduction

| | | |
|-------|---|----|
| 1.1. | Introduction of Tools for Cell, Micro- and Nano-Particle Manipulation | 1 |
| 1.2. | Dielectrophoresis (DEP) | 6 |
| 1.2.1 | CM Factor of Multi-Layer Particles | 7 |
| 1.2.2 | Effect of Surface Conductance on Nanoparticles | 11 |
| 1.3. | Electroosmosis | 13 |
| 1.3.1 | Electric Double Layer | 13 |
| 1.3.2 | Electroosmosis | 17 |
| 1.3.3 | AC electroosmosis | 20 |
| 1.4. | Reference | 21 |

Chapter 2

Principle of Optoelectronic Tweezers (OET)

| | | |
|-------|--|----|
| 2.1. | Introduction | 26 |
| 2.2. | Amorphous silicon as a photosensitive material | 29 |
| 2.3. | OET Device Design | 32 |
| 2.4. | OET Device Fabrication | 34 |
| 2.5. | Simulated Electric Field Distribution | 35 |
| 2.6. | OET Manipulation of Polystyrene Beads | 42 |
| 2.7. | OET Trapping of Live Bacteria (E. Coli) | 47 |
| 2.8. | AC Frequency Range for OET Operation | 56 |
| 2.9. | Photocurrent Measurement and Simulation of OET | 59 |
| 2.10. | Reference | 70 |

Chapter 3

Scanning OET for Microparticle Sorting

| | | |
|-----|--------------------------------|----|
| 3.1 | Introduction | 72 |
| 3.2 | Sorting Mechanism | 72 |
| 3.3 | Experimental Setup and Results | 75 |
| 3.4 | Reference | 78 |

Chapter 4

Optical Image Driven OET for Massively Parallel Manipulation

| | | |
|------|--|----|
| 4.1. | Introduction | 80 |
| 4.2. | System of Direct Optical Image Driven OET using a LED | 81 |
| 4.3. | Virtual Particle Concentrator and Conveyer | 82 |
| 4.4. | Selective Concentration of Live White Blood Cells | 84 |
| 4.5. | Massively Parallel Optical Manipulation of Microscopic Particles | 85 |
| 4.6. | Integrated Dynamic Optical Patterns for Multi-Step Manipulation | 88 |
| 4.7. | Long-Term Photodegradation of Photoconductivity in Amorphous Silicon | 91 |
| 4.8. | Reference | 92 |

Chapter 5

Image Feedback Controlled OET for Automatic Processing

| | | |
|------|--|-----|
| 5.1. | Introduction | 94 |
| 5.2. | Microvision-Activated OET system | 94 |
| 5.3. | Particle Recognition Process | 96 |
| 5.4. | Automatic Generation of Optical Patterns for Functional Manipulation | 100 |
| 5.5. | Continuous Sorting of Particles and Cells Based on Size and Color | 104 |
| 5.6. | Reference | 114 |

Chapter 6

Light-patterned AC Electroosmosis for Nanoparticle Manipulation

| | | |
|------|--|-----|
| 6.1. | Introduction | 115 |
| 6.2. | Analytical Model of Light-Patterned AC Electroosmotic Flow | 116 |
| 6.3. | Numerical Simulation of Light-Patterned AC Electroosmotic Flow | 123 |

| | | |
|-------------------|---|-----|
| 6.4. | Light-Patterned AC Electroosmosis for Nanoparticle Trapping | 130 |
| 6.5. | Reference | 135 |
| | | |
| Chapter 7 | | |
| Conclusion | | 136 |

Acknowledgement

I would like to thank Prof. Ming C. Wu for his mentoring in the past five years. My research would not be as fruitful as what has been included in this dissertation without his continuous encouraging and supporting in the difficult time during the process. I would also like to thank Prof. Chih-Ming Ho (in UCLA MAE department) and the CMISE center for giving me so much multi-discipline training experience and exposure to researchers from other fields. This provided me a much broader view of the research environment and inspired many novel ideas in my mind than I could expect. I would also like to thank Prof. Connie Chang Hasnian for her kindness of being my qualify committee chair and also the committee of my dissertation. I would also like to thank Prof. Luke Lee for being my committee in my qualify exam and dissertation. His positive feedback to my research is my biggest reward as a Ph.D student.

In the past five years, I have received numerous help from my labmates in IPL. I would like to give my special thanks to Aaron T. Ohta for his great help in both research and English writing.

As an engineering student who is new to biological field, my dear friend Yu-Ching (Kelly) Yang has being my greatest help in bridging the knowledge between the biological and engineering fields. She is my tutor in biology in research and my mental companion in life.

Finally, I would like to thank my parent for their support for my study so far away from home.

CHAPTER 1

INTRODUCTION

1.1. Introduction of Tools for Cell, Micro- and Nano-Particle Manipulation

Tools for manipulating small particles such as cells, micro-particles and nano-particles play important roles in the fields of biological research and colloid science. These tools are used to perform important functions such as the sorting, addressing, transporting, and trapping of cells and particles in these fields. Several mechanisms have been applied to manipulate small particles are versatile, including optical tweezers [1], electrophoresis [2], dielectrophoresis [3], magnetic tweezers [4], acoustic force [5], and hydrodynamic force [6]. Each technique has its advantages and unique features. For example, optical tweezers provides precise trapping of single particles, but the number of particles that can be manipulated in parallel is limited. Electrokinetic mechanisms (electrophoresis and dielectrophoresis) can achieve high throughput, but control at the single-cell or single-particle level is limited. The same is true for other mechanisms such as magnetic tweezers, or hydrodynamic forces. The restriction comes from the limitation of addressing these forces to individual cells without interference with each other. Tools that can simultaneously achieve high resolution and high throughput are missing.

Optical tweezers was first proposed by Ashkin in 1986[7]. It has become a powerful tool in biological fields for trapping cells and characterizing the forces of biomolecules and molecular motors. The optical force originates from the transfer of the photon momentum from the incident light beam to the manipulated particle. The first optical radiation force was observed by Ashkin in 1970, showing that a focused laser beam can affect the dynamics of small transparent particles[8]. Two forces were identified; the radiation force pushes the particle in the direction of light propagation, and the gradient force attracts the particle in the direction of the intensity gradient, as shown in Fig.1-1.

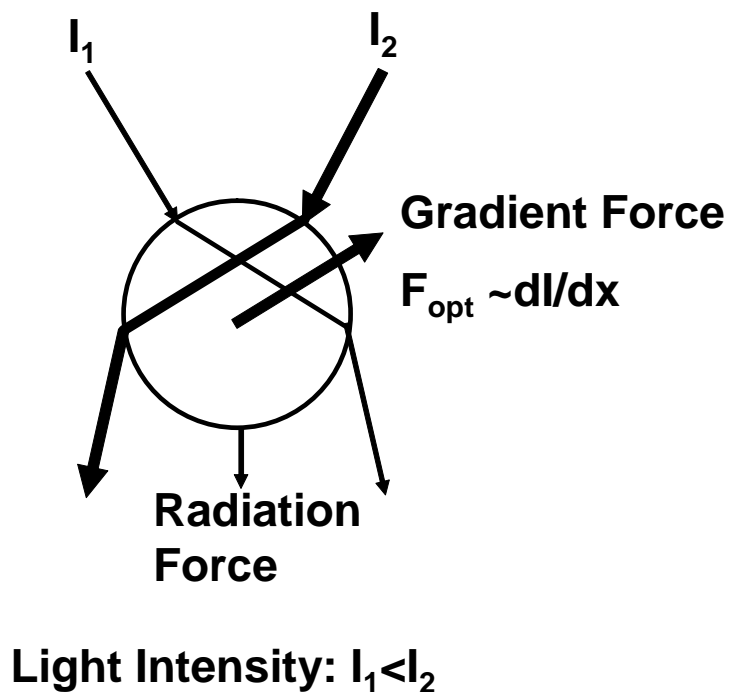


Fig.1-1. The illustration of the optical forces generated by a focused laser beam using the ray optics method. The particle is confined in the focal point in both the lateral and vertical directions.

To form a stable particle trap in the focal point, the gradient force needs to overcome the scattering force that pushes the particle out of the trap point. An objective lens with high numerical aperture (typically N.A. > 1) is required to form a tightly focused laser beam in which the gradient force dominates at the focal point [1]. The first single beam optical tweezers was demonstrated in 1986, with the trapping of a submicron silica sphere using a highly focused 514 nm argon laser [7]. For biological cell manipulation, a tightly focused laser beam with wavelength at the near infrared window is used to prevent optical damage to the cell due to the heat generated from absorption of the strong incident laser beam [9, 10]. The force generated by optical tweezers can be up to the nanonewton level, depending on the optical power and the efficiency of the optical trap. The force of the optical trap can be expressed by $F = Q \frac{nP}{c}$, where c/n is the speed of light in the medium, P is the optical power and Q is the trap efficiency[11]. For a spherical particle with a radius equal to the wavelength of light, the efficiency is ~ 0.1 and the optical force is ~ 0.5 pN/mW. For particles much smaller than the wavelength, the efficiency decreases as the optical force in this size range is proportional to the volume of the particles.

However, optical tweezers has some limitations. The effective manipulation area is limited by the field of view of the high N.A. objective lens. For a 100 \times oil immersion lens, the effective area is less than $100 \times 100 \mu\text{m}^2$, limiting the capability of parallel manipulation to a small number of cells (the size of a mammalian cell is $\sim 10 \mu\text{m}$). Increasing the manipulation area by using a low N.A. objective lens is possible, but sacrifices the strength of the gradient force, resulting in a less stable trap. A further limitation is the high light intensity requirement for optical traps. The minimum optical

power required to overcome the Brownian motion of the trapped particle, forming a stable optical trap, is ~ 1 mW [12]. The power required for multiple traps is proportional to the number of traps. To operate a typical holographic optical tweezers setup, a high-power laser with 200 mW to 4W output power is required [12, 13]. The maximum laser power is limited by the photodamage threshold of light-sensitive components such as the spatial light modulator.

Magnetic forces are frequently used for the sorting of biological cells because magnetic fields have less effects on the manipulated cells than electrical or optical fields. Magnetic beads are polymer spheres containing a large number of superparamagnetic nanoparticles. The surface of the magnetic bead can be functionalized with antibodies, peptides, or lectins, to attach to or be engulfed by cells [14-16]. The target cells recognized by these biomarkers are attached by the magnetic beads and can be sorted out by applying a magnetic field. To achieve high-resolution manipulation using a magnetic field, a microelectromagnetic template has been proposed to manipulate single cells as shown in Fig.1-2 [4]. By controlling the applied electric currents to the programmed wires in the matrix, a highly localized magnetic field profile can be created to address the cells that have been pretreated with functionalized magnetic beads. The force generated in the magnetic field can be expressed as $F = m \cdot \nabla B$, where m is the magnetic moment and B is the magnetic flux. Due to the supermagnetic nature of the beads, the magnetic moment is proportional to the field, $m = V\chi B / \mu_0$, where V is the volume of the magnetic bead, χ is the susceptibility of the bead, and μ_0 is the permeability in the vacuum [4]. The magnetic trap force is $F = \frac{1}{2\mu_0} V\chi \nabla B^2$. For the applied current shown in Fig.1-2(b), a peak magnetic flux of 10 mT and a maximum magnetic force of 40 pN are created.

There are, however, some limitations of using magnetic tweezers. The attachment of magnetic beads to cells may affect the cells' intrinsic properties, which may prevent the user from observing the original cell responses. Although the microelectromagnetic template has shown the potential to manipulate single cells, parallel manipulation of

multiple cells still remains challenging due to the cross-interference of traps at high density of the cells.

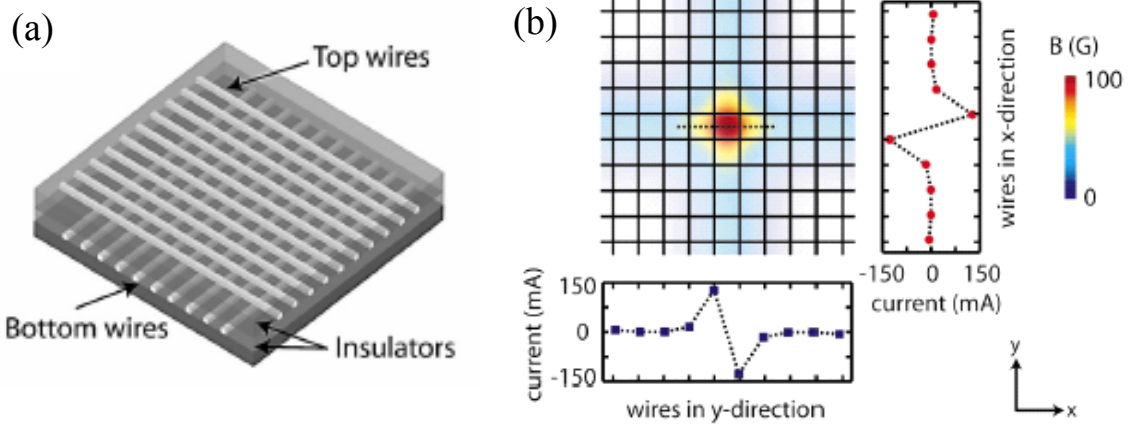


Fig.1-2 The microelectromagnetic template for cell manipulation using electromagnetic force. (a) Device structure showing two perpendicular layers of metal wires, which form the magnetic matrix. (b) Electric currents are applied to create a localized magnetic field.

Electrokinetics is the most commonly used technique for manipulating micro- and nanoscale particles in microfluidic devices, as progress in microfabrication technology has made the patterning of arbitrarily-shaped electrodes routine. The electrostatic forces can be precisely addressed to control microparticles by the high-resolution electrodes on a microfluidic device. Two frequently used electrokinetic mechanisms are electrophoresis [2, 17] and dielectrophoresis [18, 19]. Electrophoresis refers to the particle motion induced by an electric field on particles with net charges. In electrophoresis, a d.c. electric field is usually applied to sort out nanoscale particles such as DNA or proteins, based on their electrophoretic mobility. Particles with a higher mobility can move faster under the same electric field strength, $v = \mu E$, where v is the velocity, μ is the electrophoretic mobility, and E is the electric field [2].

The other frequently used electrokinetic mechanism is dielectrophoresis (DEP), which refers to the particle motion due to the force generated by a non-uniform electric field acting upon field-induced dipoles of the particles. The magnitude of this dielectrophoretic force is proportional to the volume of the manipulated particles and the

gradient of the electric field intensity (E^2). Dielectrophoresis has been used to trap and sort micro- and nano-meter particles such as cells, bacteria, and viruses [18, 20-23].

Electrokinetic mechanisms are convenient tools for cell manipulation in multi-particle or batch modes. However, to manipulate single cells that are randomly distributed on a surface, it needs high-resolution, pre-patterned electrode pixels to address single cells. The chip also needs to cover sufficiently large areas to allow dispersion of single cells. The wiring and addressing of these electrodes becomes one of the challenges of using electrokinetic mechanisms for single cell manipulation. To solve this issue, a complementary metal oxide semiconductor (CMOS) DEP has been proposed for parallel manipulation of more than 10,000 electrodes[24]. However, the CMOS DEP chip might be cost effective for many biological applications, especially for disposable devices for the prevention of cross-contamination.

To summarize, optical tweezers offers high resolution for trapping single particles, but has a limited manipulation area due to tight focusing requirements, while electrokinetic forces and other mechanisms provide high throughput, but lack the flexibility or the spatial resolution necessary for controlling individual cells. In this dissertation, I propose optical image-driven electrokinetic mechanisms for massively parallel real-time manipulation of single cells, micro- and nano-particles in real-time on optoelectronic devices. This novel mechanism permits optical manipulation with a light intensity 100,000 times less than optical tweezers and dramatically increases the effective manipulation area for parallel manipulation using light. The light-driven electrokinetic mechanisms also avoid the wiring issues present in addressing electrokinetic mechanisms using patterned electrodes, promising the parallel manipulation of single cells on a low cost, disposable, silicon-coated glass slide. Details of the applied electrokinetic mechanisms are discussed in the following sessions.

1.2. Dielectrophoresis (DEP)

Dielectrophoresis refers to the motion of a particle induced by the interaction between a non-uniform electric field and the induced electric dipole of the particle. The magnitude of DEP force can be expressed as [25]

$$\langle F_{dep}(t) \rangle = 2\pi a^3 \varepsilon_m \operatorname{Re}[K^*(\omega)] \nabla(E_{rms}^2) \quad (1.1)$$

$$K^*(\omega) = \frac{\varepsilon_p^* - \varepsilon_m^*}{\varepsilon_p^* - 2\varepsilon_m^*}, \varepsilon_p^* = \varepsilon_p - j \frac{\sigma_p}{\omega}, \varepsilon_m^* = \varepsilon_m - j \frac{\sigma_m}{\omega} \quad (1.2)$$

where $\langle F_{dep}(t) \rangle$ represents the time-average of the function $F_{dep}(t)$, E_{rms} is the root-mean-square magnitude of the imposed a.c. electric field, a is the particle radius, ε_m and ε_p are the permittivities of the surrounding medium and the particle, respectively, σ_m and σ_p are the conductivities of the medium and the particle, respectively, ω is the angular frequency of the applied electric field, and $K^*(\omega)$ is the Clausius-Mossotti (CM) factor.

1.2.1 CM Factor of Multi-layer Particles

The Clausius-Mossotti factor of a particle represents its frequency response to an external electric field. It is the particle's dielectric signature, which characterizes the particle's size, composition, structure, and surface charge concentration. For a spherical particle with multiple shells, each with different dielectric constant and conductivity, as shown in Fig.1-3, the CM factor can be derived from an equivalent complex permittivity as[25]

$$K^*(\varepsilon_2', \varepsilon_1) = \frac{\varepsilon_2' - \varepsilon_1}{\varepsilon_2' + 2\varepsilon_1} \quad (1.3)$$

$$\varepsilon_2' = \varepsilon_2 \left\{ \frac{a^3 + 2 \left(\frac{\varepsilon_3 - \varepsilon_2}{\varepsilon_3 + 2\varepsilon_2} \right)}{a^3 - \left(\frac{\varepsilon_3 - \varepsilon_2}{\varepsilon_3 + 2\varepsilon_2} \right)} \right\} \quad (1.4)$$

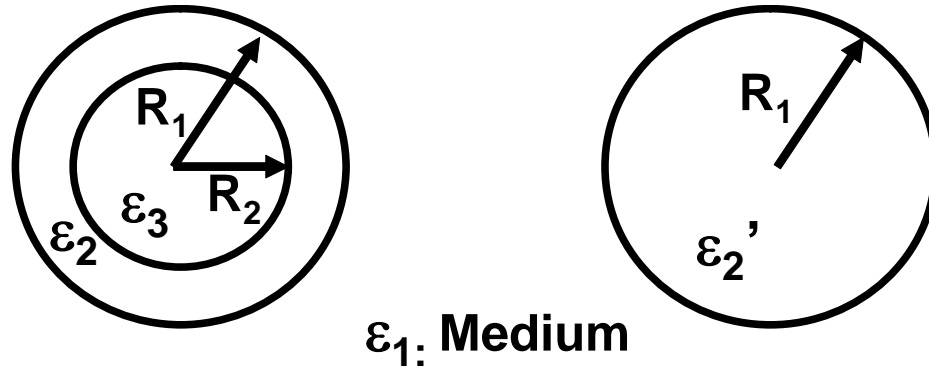


Fig.1-3 Spherical dielectric shells with radii of R_1 and R_2 and shell permittivities of ϵ_2 and ϵ_3 , respectively.

where $\epsilon_1, \epsilon_2, \epsilon_3$ are the complex permittivities of the medium and the shells of the particle, $a=R_1/R_2$, and ϵ_2' is the new equivalent permittivity of the particle. The real part of $K^*(\omega)$, $\text{Re}[K^*(\omega)]$, has a value between 1 and $-1/2$, depending on the polarizability of the medium and the particle at a certain frequency. If $\text{Re}[K^*(\omega)] > 0$, the induced electric dipole is collinear with the electric field as shown in Fig.1-4(a). The particle will move towards the strong electric field region, a phenomenon known as positive DEP. On the other hand, if $\text{Re}[K^*(\omega)] < 0$, the induced electric dipole is anti-parallel to the electric field as shown in Fig.1-4(b). The particle moves towards the weaker electric field region, known as negative DEP.

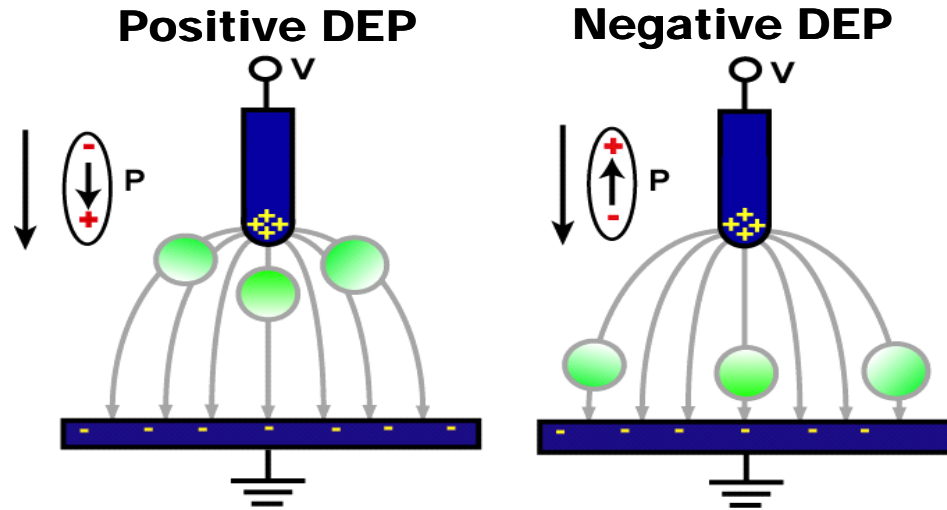


Fig.1-4 Illustration of positive and negative DEP forces. (a) For positive DEP, the field induced electric dipole on the particle is collinear with the direction of the applied electric field. The particles move towards the strong electric field region. (b) For negative DEP, the dipole direction is anti-parallel to the applied electric field and the particles are pushed towards the weaker electric field region.

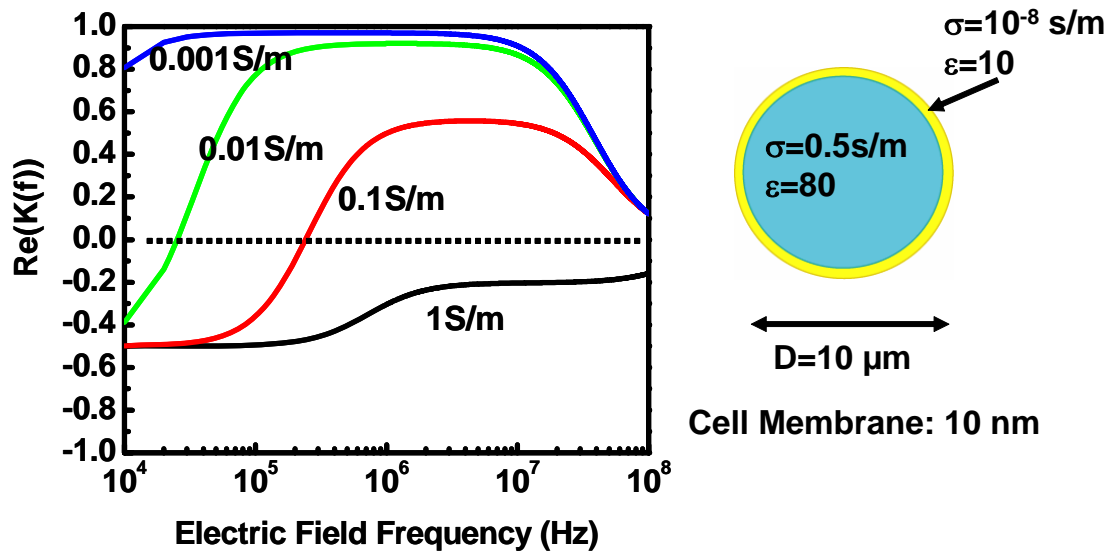


Fig.1-5 The simulated real part CM factor of a 10- μm mammalian cell in mediums with liquid conductivities of 1 mS/m, 10 mS/m, 100 mS/m, and 1 S/m. The cell membrane is assumed to have a 10 nm thickness and a low conductivity. Inside the cell membrane, the liquid conductivity is assumed to have a constant value of 0.5 S/m.

Figure 1-5 shows the frequency-dependent values of the real part of the CM factor of a simulated mammalian cell in various medium conductivities. In order to simulate the cell using Eq. (1.1), the cell is represented by a simple dielectric model. A typical mammalian cell is around 10 μm in diameter. The cell membrane is formed by a lipid bilayer and has a thickness around 10 nm. In a live cell, this membrane is selectively permeable to ions and can be modeled as a low conductivity layer. Inside the cell membrane are the subcellular structures and cytoplasm, which consist of ions, proteins, and sugars. The average liquid conductivity inside the cell membrane is assumed to be 0.5 S/m.

At low frequencies, the real-part of the CM factor is negative, meaning the induced DEP force is negative. In this range, the cell membrane is fully charged with ions, and a large electric field across the membrane can rupture the cell. When the applied frequency increases, the real part of the CM factor starts to move to positive regime, as the ions in the medium do not have time to charge the membrane capacitance. The frequency at which the real part of the CM factor begins to increase is characterized by the time constant $\tau_1 = RC_{\text{mem}} / \sigma_m$, where R is the radius of the cell, C_{mem} is the cell membrane capacitance, and σ_m is the medium conductivity outside the cell membrane. For a 0.1 S/m medium conductivity, this transition starts at 20 kHz. At 200 kHz, the electrical impedance of the membrane capacitance is comparable to the liquid medium, resulting in the real part of the CM factor having a value of zero. This frequency is called cross-over frequency, and no DEP force is induced. As the frequency is increased further, the real part of the CM factor saturates at a constant value, which is determined by the conductivity terms of the media in the cell interior and outside the cell membrane, $(\sigma_c - \sigma_m) / (\sigma_c + 2\sigma_m)$, where σ_c and σ_m are the conductivity of the cytoplasm and the extracellular medium, respectively. If the medium is less conductive than the cell, this value will be positive; on the other hand, if the medium is more conductive, the value at higher frequencies would be negative, and the cell does not have a positive DEP regime, as seen in the 1 S/m curve of Fig. 1-5. As the frequency increases above 10 MHz, these CM factors move into another dispersion regime in which the membrane capacitance becomes more conductive than the cytoplasm. This frequency can be characterized by the time constant $\tau_{\text{mem}} = RC_{\text{mem}} / \sigma_c$, where R is the radius of the cell, C_m is the capacitance of the

cell membrane, and σ_c is the conductivity of the cytoplasm. The time constant τ_{mem} is cell size-dependent and is equal to 8.8×10^{-8} sec for a 10- μ m cell. Another time constant, $\tau_m = \epsilon_m / \sigma_m$ also plays an important role at this frequency range. For a 0.01 S/m aqueous medium, τ_m has a value of 7×10^{-8} sec. When the applied frequency is higher than $f = 1 / (2\pi\tau_m)$, the medium conductivity is dominated by the dielectric term, which increases with the frequency [25]. This results in the decrease of the positive CM factors at frequencies above 10 MHz for media with conductivities of 0.001 S/m, 0.01 S/m, and 0.1 S/m (Fig.1-5).

This multi-layer model can also predict the frequency-dependent CM factor for bacteria, by adding one more layer to account for the cell wall (if necessary).

1.2.2 Effect of Surface Conductance on Nanoparticles

The surface conductance of a particle can profoundly affect its CM factor and DEP response, especially for insulating particles that have a low intrinsic conductivity, such as latex beads. The surface conductance originates from concentrated charged ions in the electric double layer on a particle surface.

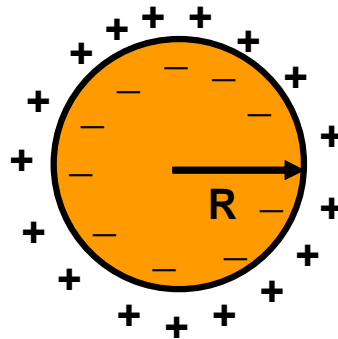


Fig.1-6. The electric double layer at the particle surface is a heterogeneous layer between the particle and the bulk liquid medium. The concentrated charged ions give rise to a higher liquid conductivity at this thin layer as compared to the bulk medium.

As shown in Fig. 1-6, the liquid conductivity in this charge-concentrated layer is more conductive than that of the bulk medium. For a particle that has a low intrinsic

conductivity, the overall particle conductivity is dominated by the surface conductance, resulting in a frequency-dependent CM factor that is similar to that of a conductive particle. The new effective particle conductivity, modified by the surface conductance, can be expressed as [26]

$$\sigma_p = \sigma_{\text{int}} + \frac{2\rho\mu}{R} \quad (1.5)$$

where σ_p , σ_{int} , ρ , μ , R are the particle's effective conductivity, particle's intrinsic conductivity, surface charge density, ion mobility, and the radius of the particle, respectively. Nanoscopic particles are more sensitive to the surface conductance than the microscopic particles. The simulated results of the $\text{Re}[K^*(\omega)]$ and the crossover frequencies of particles with different effective conductivities are shown in Fig. 1-7[27]. The surface conductance can profoundly affect the cross-over frequency, as shown in Fig.1-7(b).

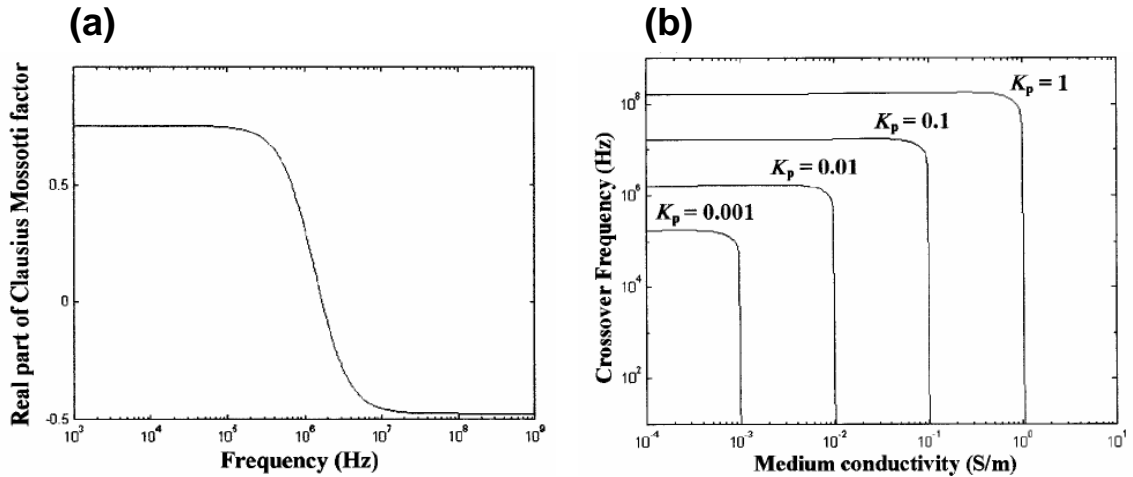


Fig.1-7 The frequency-dependent CM factors for nanoscopic polystyrene particles [27]. (a) The simulated real-part of the CM factor of a particle having an effective conductivity of 10^{-2} S/m in medium with conductivity of 10^{-3} S/m. The relative permittivity of the particle and the suspending medium were 2.55 and 78.5, respectively. (b) The variation in crossover frequency with medium conductivity as a function of particle conductivity, K_p .

1.3. Electroosmosis

1.3.1 Electric Double Layer

In an electrochemical system where no charge can be transferred across the electrode-solution interface, the electrode is called an ideal polarized electrode. The electrode-solution interface behaves as a capacitor. As a potential is applied to the electrode, charges will start to accumulate in the capacitor until the potential drop across the capacitor is equal to the applied potential. During the charging process, charging current is induced in the liquid, whose magnitude is limited by the resistance of the bulk liquid medium. The charge on the metal, q^m , represents the excess or deficiency of electrons accumulating in a very thin layer (< 0.01 nm) on the metal surface. The charge in the solution, q^s , is made up of an excess of cations or anions in the vicinity of the electrode surface. The whole array of charged species existing at the metal-solution interface is called the electrical double layer (EDL) [28].

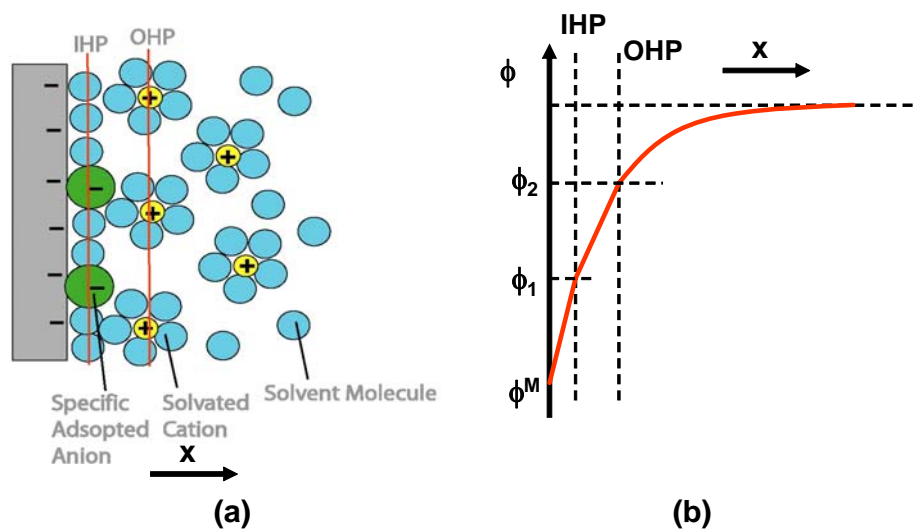


Fig.1-8 The electric double layer (EDL) at the electrode-solution interface. (a) The multiplayer structure of the double layer. (b) The potential profile in the double layer. The potential in the bulk liquid layer is grounded for reference.

The double layer in the solution consists of several layers as shown in Fig.1-8(a). The inner layer, which is closest to the electrode, contains solvent molecules and other

species that are specifically absorbed. This layer is also called the compact, Helmholtz, or Stern layer. The locus of the electrical charge centers of the specifically absorbed ions is called the inner Helmholtz plane (IHP). The solvated ions can only approach the electrode at a distance beyond the IHP. The locus of the electrical centers of the closest solvated ions is called the outer Helmholtz plane (OHP). The solvated ions and the electrode interact via only long-range electrostatic forces, which is independent of the chemical properties of the ions. The solvated ions are nonspecifically absorbed. Due to thermal agitation, these ions extend from the OHP to the bulk solution, and form a three-dimensional region called the diffuse layer. In equilibrium, the sum of the total charges of the specifically absorbed ions and the nonspecifically absorbed ions is equal to that of the charges on the electrode.

Even though the charge on the electrode is confined to the surface, it may take a significant distance to accumulate enough ions in the diffuse double layer to counterbalance the charges on the electrode, especially in solutions with a low electrolyte concentration. The highest concentration of excess charges is adjacent to the electrode, as there is a strong electrostatic force attracting these ions. The ion concentration becomes progressively less at longer distances, since the electric field is partially screened by the ions that are accumulated closer to the electrode. Gouy and Chapman have offered a statistical mechanics approach to describe the relation between the applied potential and the ion distribution in the diffuse double layer. In their approach, the Poisson equation in electrostatic and the Boltzmann distribution in statistical mechanics are coupled to yield the Poisson-Boltzmann equation to describe the system[29, 30]:

$$\frac{d^2\phi}{dx^2} = -\frac{e}{\epsilon\epsilon_0} \sum_i n_i^o z_i \exp\left(\frac{-z_i e \phi}{kT}\right) \quad (1.6)$$

where ϕ is the potential measured with respect to the bulk solution, e is the electron charge, n_i^o is the bulk concentration of ion i , z_i is the number of the valence electrons of ion I (for example, the valence of K^+ is 1), k is the Boltzmann constant, and T is the temperature. At the electrode surface, $x=0$. Solving Eq.(1.6) generates a potential profile expressed as

$$\frac{\tanh(ze\phi/4kT)}{\tanh(ze\phi_0/4kT)} = e^{-\kappa x} \quad (1.7)$$

$$\text{where } k = \left(\frac{2n^0 z^2 e^2}{\epsilon \epsilon_0 kT} \right)^{1/2} \quad (1.8)$$

and ϕ_0 is the potential at $x=0$, relative to the bulk solution. The value $1/\kappa$ is defined as the thickness of the diffuse layer, which depends on the electrolyte concentration. The diffuse layer thickness in the high-concentration solutions is shorter than that of low-concentration solutions. The diffuse layer is as thick as 30 nm in a solution with an electrolyte concentration of 10^{-4} M. In a typical bio-buffer (a buffer solution for biological cells), the electrolyte concentration is ~ 100 mM, resulting in a double layer thickness of ~ 1 nm. Fig.1-9 shows the diffuse layer thickness as calculated from Eq.(1.8).

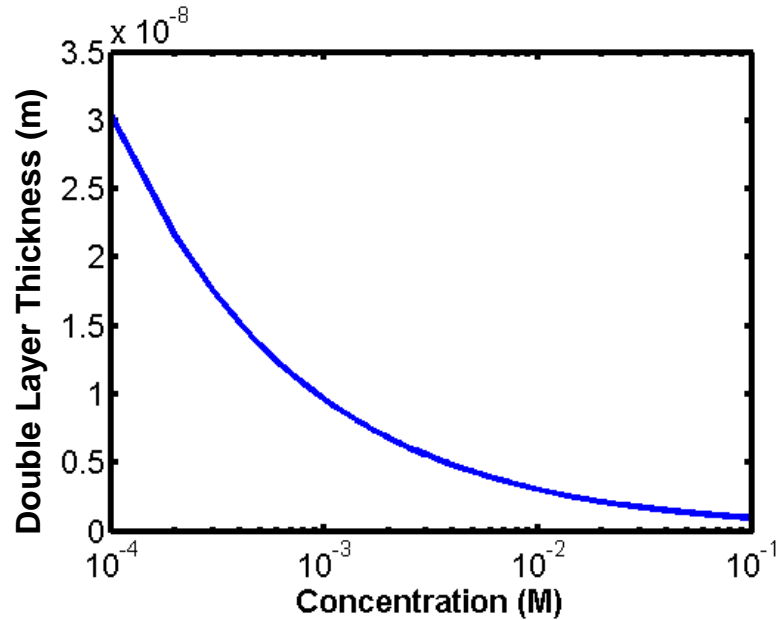


Fig.1-9 The thickness of the diffuse layer calculated from Eq.(1.8).

The charge density at the electrode surface, σ^M , or the charge in the double layer, σ^S , can be derived from Eq.(1.7) using Gauss's Law:

$$q = \varepsilon\varepsilon_o \int_{surface} E \cdot dS \quad (1.9)$$

$$q = \varepsilon\varepsilon_o \left(\frac{d\phi}{dx} \right)_{x=0} \int_{surface} dS \quad (1.10)$$

$$\sigma^M = -\sigma^S = (8kT\varepsilon\varepsilon_o n^o)^{1/2} \sinh\left(\frac{ze\phi_o}{2kT}\right) \quad (1.11)$$

By differentiating Eq. (1.11), the differential capacitance is calculated:

$$C_d = \left(\frac{2z^2 e^2 \varepsilon\varepsilon_o n^o}{kT} \right)^{1/2} \cosh\left(\frac{ze\phi_o}{2kT}\right) \quad (1.12)$$

The calculated capacitance for solutions with different electrolyte concentrations at 25°C is shown in Fig. 1-10. In the low-electrolyte solution, the differential capacitance can be approximated by a constant value when the potential is smaller than 50 mV.

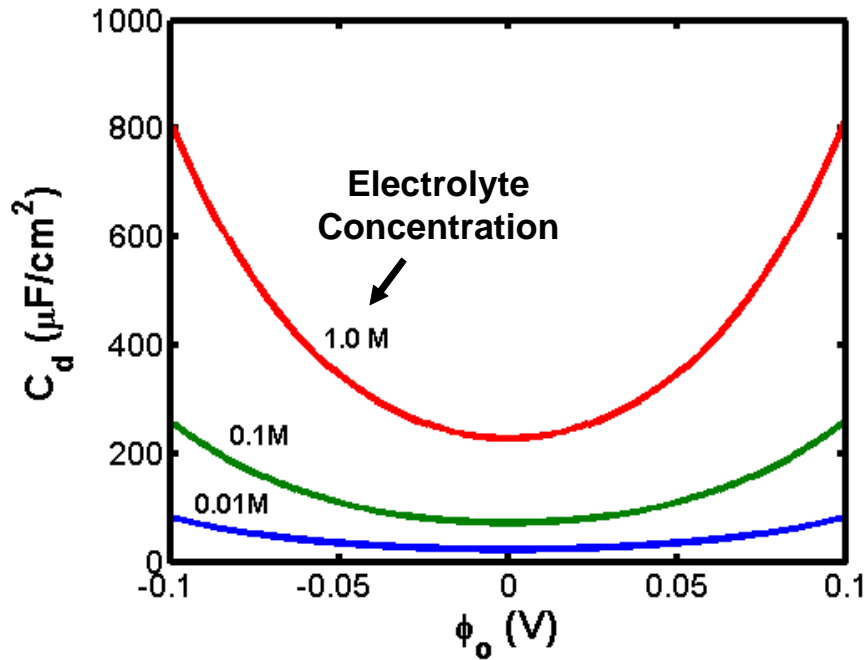


Fig.1-10 The predicted differential capacitance based on Gouy-Chapman theory. The capacitance rises rapidly as the potential increases in the solution with a high electrolyte concentration.

1.3.2 Electroosmosis

The theory of electroosmosis was first proposed by von Smoluchowski in 1921 to explain the movement of liquid adjacent to an electrode surface under the influence of an electric field applied parallel to the electrode-solution interface. If the electrode is negatively charged, there are excess positive ions in the adjacent liquid. As the positive ions move with the applied electric field, it draws the liquid along. The shear surface is a plane parallel to the electrode, at a distance δ , as shown in Fig.1-11.

The velocity of the liquid moving in the direction parallel to the electrode rises from zero at the shear surface to a maximum value of v_{slip} at some distance from the electrode. The maximum speed v_{slip} is called the slip velocity or the electroosmotic velocity of the liquid[31].

To derive the slip velocity of the liquid, an element of the volume of the liquid is considered (Fig.1-12). The equations that describe this element are:

$$E_z \rho A dx = \eta A \left(\frac{dv_z}{dx} \right)_x - \eta A \left(\frac{dv_z}{dx} \right)_{x+dx} \quad (1.13)$$

where ρ is the density of the liquid, A is the area of this liquid element, η is the viscosity of the liquid, E_z is the electric field parallel to the surface, and v_z is the velocity of the liquid element. The left hand side of Eq. (1.13) represents the electrostatic force pushing the liquid element in the z direction. The two terms in the right hand side of Eq. (1.8) represents the shear stress at the two surfaces of the liquid element. Eq.(1.13) represents the steady state situation where the electrostatic force and the shear stress are equal.

$$E_z \rho dx = \eta \left(\frac{d^2 v_z}{dx^2} \right) dx \quad (1.14)$$

Using Poisson's equation for ρ results in:

$$E_z (4\pi\epsilon_0) \frac{\epsilon}{4\pi} \frac{d^2 \psi}{dx^2} dx = \eta \left(\frac{d^2 v_z}{dx^2} \right) dx \quad (1.15)$$

This equation can be integrated twice from the shear plane where $v_z=0$ and $\psi=\zeta$ to a point in the bulk liquid layer where $v_z=v_{slip}$, $\psi=0$, $d\psi/dx=0$, and $dv_z/dx=0$. The ζ potential is defined as the potential difference between the bulk liquid and the shear plane where the velocity equals to zero.

The result is:

$$v_{slip} = -\frac{\epsilon \zeta E_z}{\eta} \quad (1.16)$$

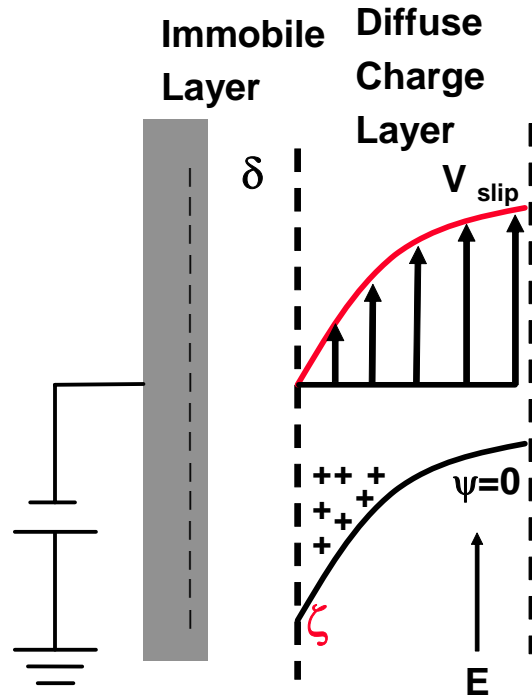


Fig.1-11 Illustration of the electroosmotic flow driven by the Coulomb force created by the coupling of the surface double layer charges and the tangential electric field. The slip velocity, v_{slip} , is proportional to electric field strength and the zeta potential.

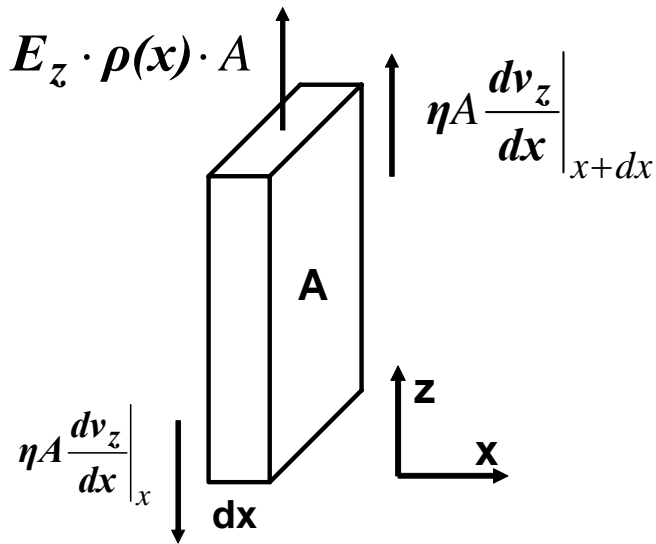


Fig.1-12 The forces on an element of the liquid with area A and containing a charge of ρA .

1.3.3 AC Electroosmosis

During DEP manipulation, an abnormal particle motion is observed when operating in low ac frequencies. This abnormal particle motion could not be explained by the DEP forces [32, 33]. Recent publications have shown that a steady fluidic flow could also be induced near microelectrodes at low frequency DEP manipulation conditions [34-36]. This flow is generated by the coupling between the double layer charges on the electrodes and the tangential component of the applied electric field. Fig.1-13 illustrates the equivalent circuit model and the direction of the induced Coulomb forces for driving the electroosmotic flow at the electrode surface. The double layer on top of the electrode behaves as a capacitor, resulting in a short circuit at high frequency operation. A very small amount of the applied voltage drops across the double layer and only a few charged ions are stored at the electrode interface. Most of the voltage drops across the bulk liquid medium, resulting in DEP manipulation. However, as the applied frequency decreases, the impedance of the double-layer capacitor becomes large enough to compete with that of the bulk liquid, and charged ions start to accumulate at the double layer. The tangential component of the electric field at the electrode interface couples with these surface charges and produces a Coulomb force, driving fluid flow at the liquid interface. Although an ac bias is applied, the polarity of the interface charges reverse with the direction of the electric field, resulting in a steady state dc force that drives the surface liquid layer continuously in the same direction. The surface flow provides a strong driving source to move the bulk liquid. This phenomenon is called ac electroosmosis.

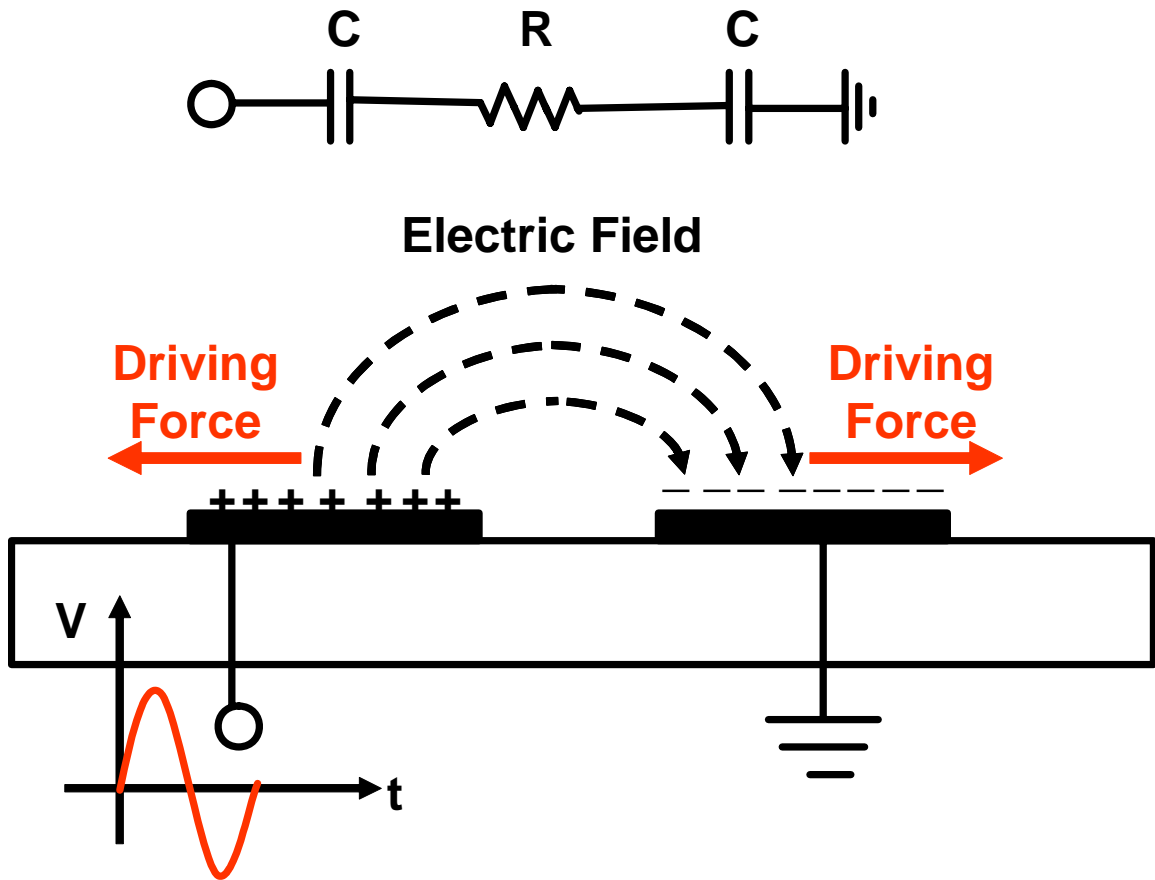


Fig.1-13 Illustration of the mechanism of ac electroosmosis. The charged ions stored at the electrode surface are driven by the tangential component of the electric field, causing fluid flow. The flowing boundary layers behave as the driving source to pump flow in the bulk liquid layer.

1.4 Reference

- [1] D. G. Grier, "A revolution in optical manipulation," *Nature*, vol. 424, pp. 810-816, 2003.
- [2] L. Kremser, D. Blaas, and E. Kenndler, "Capillary electrophoresis of biological particles: Viruses, bacteria, and eukaryotic cells," *Electrophoresis*, vol. 25, pp. 2282-2291, 2004.

- [3] M. P. Hughes, "Strategies for dielectrophoretic separation in laboratory-on-a-chip systems," *Electrophoresis*, vol. 23, pp. 2569-2582, 2002.
- [4] H. Lee, A. M. Purdon, and R. M. Westervelt, "Manipulation of biological cells using a microelectromagnet matrix," *Applied Physics Letters*, vol. 85, pp. 1063-1065, 2004.
- [5] H. M. Hertz, "Standing-Wave Acoustic Trap For Nonintrusive Positioning Of Microparticles," *Journal Of Applied Physics*, vol. 78, pp. 4845-4849, 1995.
- [6] N. Sundararajan, M. S. Pio, L. P. Lee, and A. A. Berlin, "Three-dimensional hydrodynamic focusing in polydimethylsiloxane (PDMS) microchannels," *Journal Of Microelectromechanical Systems*, vol. 13, pp. 559-567, 2004.
- [7] A. Ashkin, J. M. Dziedzic, J. E. Bjorkholm, and S. Chu, "Observation Of A Single-Beam Gradient Force Optical Trap For Dielectric Particles," *Optics Letters*, vol. 11, pp. 288-290, 1986.
- [8] A. Ashkin, "Acceleration and Trapping of Particles by Radiation Pressure," *Physical Review Letters*, vol. 24, pp. 156, 1970.
- [9] A. Ashkin and J. M. Dziedzic, "Optical Trapping And Manipulation Of Viruses And Bacteria," *Science*, vol. 235, pp. 1517-1520, 1987.
- [10] A. Ashkin, J. M. Dziedzic, and T. Yamane, "Optical Trapping And Manipulation Of Single Cells Using Infrared-Laser Beams," *Nature*, vol. 330, pp. 769-771, 1987.
- [11] J. Howard, *Mechanics of Motor Proteins and the Cytoskeleton*. Sunderland, Massachusetts: Sinauer Associates, Inc., 2001.

- [12] J. E. Curtis, B. A. Koss, and D. G. Grier, "Dynamic holographic optical tweezers," *Optics Communications*, vol. 207, pp. 169-175, 2002.
- [13] W. J. Hossack, E. Theofanidou, and J. Crain, "High speed holographic optical tweezers using a ferroelectric liquid crystal microdisplay," *Optics Express*, vol. 11, pp. 2053-2059, 2003.
- [14] A. G. J. Tibbe, B. G. de Grooth, J. Greve, P. A. Liberti, G. J. Dolan, and L. Terstappen, "Optical tracking and detection of immunomagnetically selected and aligned cells," *Nature Biotechnology*, vol. 17, pp. 1210-1213, 1999.
- [15] A. Radbruch, B. Mechtold, A. Thiel, S. Miltenyi, and E. Pfluger, "High-Gradient Magnetic Cell Sorting," in *Methods In Cell Biology, Vol 42*, vol. 42, *Methods In Cell Biology*, 1994, pp. 387-403.
- [16] J. Ugelstad, P. Stenstad, L. Kilaas, W. S. Prestvik, R. Herje, A. Berge, and E. Hornes, "Monodisperse Magnetic Polymer Particles - New Biochemical And Biomedical Applications," *Blood Purification*, vol. 11, pp. 349-369, 1993.
- [17] W. D. Volkmuth and R. H. Austin, "Dna Electrophoresis In Microlithographic Arrays," *Nature*, vol. 358, pp. 600-602, 1992.
- [18] A. T. J. Kadaksham, P. Singh, and N. Aubry, "Dielectrophoresis of nanoparticles," *Electrophoresis*, vol. 25, pp. 3625-3632, 2004.
- [19] T. Muller, A. Pfennig, P. Klein, G. Gradl, M. Jager, and T. Schnelle, "The potential of dielectrophoresis for single-cell experiments," *Ieee Engineering In Medicine And Biology Magazine*, vol. 22, pp. 51-61, 2003.

- [20] J. Tang, B. Gao, H. Z. Geng, O. D. Velev, L. C. Din, and O. Zhou, "Manipulation and assembly of SWNTS by dielectrophoresis," *Abstracts Of Papers Of The American Chemical Society*, vol. 227, pp. U1273-U1273, 2004.
- [21] M. P. Hughes, H. Morgan, and F. J. Rixon, "Measuring the dielectric properties of herpes simplex virus type 1 virions with dielectrophoresis," *Biochimica Et Biophysica Acta-General Subjects*, vol. 1571, pp. 1-8, 2002.
- [22] C. F. Chou, J. O. Tegenfeldt, O. Bakajin, S. S. Chan, E. C. Cox, N. Darnton, T. Duke, and R. H. Austin, "Electrodeless dielectrophoresis of single- and double-stranded DNA," *Biophysical Journal*, vol. 83, pp. 2170-2179, 2002.
- [23] M. Stephens, M. S. Talary, R. Pethig, A. K. Burnett, and K. I. Mills, "The dielectrophoresis enrichment of CD34(+) cells from peripheral blood stem cell harvests," *Bone Marrow Transplantation*, vol. 18, pp. 777-782, 1996.
- [24] N. Manaresi, A. Romani, G. Medoro, L. Altomare, A. Leonardi, M. Tartagni, and R. Guerrieri, "A CMOS chip for individual cell manipulation and detection," *IEEE J. Solid-State Circuits*, vol. 38, pp. 2297-2305, 2003.
- [25] T. B. Jones, *Electromechanics of particles*. New York: Cambridge University Press, 1995.
- [26] C. T. Okonski, "Electric Properties Of Macromolecules.5. Theory Of Ionic Polarization In Polyelectrolytes," *Journal Of Physical Chemistry*, vol. 64, pp. 605-619, 1960.
- [27] N. G. Green and H. Morgan, "Dielectrophoresis of submicrometer latex spheres. 1. Experimental results," *Journal Of Physical Chemistry B*, vol. 103, pp. 41-50, 1999.

- [28] A. J. Bard and L. R. Faulkner, *Electrochemical methods: fundamentals and applications*. New York: John Wiley & Sons, 2001.
- [29] D. L. Chapman, *Philosophical Magazine*, vol. 25, pp. 475, 1913.
- [30] G. Gouy, *Journal of Physical Chemistry*, vol. 9, pp. 457, 1910.
- [31] R. J. Hunter, *Zeta Potential in Colloid Science*. New York: Academic Press Inc., 1981.
- [32] A. Ramos, H. Morgan, N. G. Green, and A. Castellanos, "AC electric-field-induced fluid flow in microelectrodes," *Journal Of Colloid And Interface Science*, vol. 217, pp. 420-422, 1999.
- [33] A. Ramos, A. Gonzalez, A. Castellanos, H. Morgan, and N. G. Green, "Fluid flow driven by a.c. electric fields in microelectrodes," in *Electrostatics 1999*, vol. 163, *Institute Of Physics Conference Series*, 1999, pp. 137-140.
- [34] N. G. Green, A. Ramos, A. Gonzalez, H. Morgan, and A. Castellanos, "Fluid flow induced by nonuniform ac electric fields in electrolytes on microelectrodes. I. Experimental measurements," *Physical Review E*, vol. 61, pp. 4011-4018, 2000.
- [35] A. Gonzalez, A. Ramos, N. G. Green, A. Castellanos, and H. Morgan, "Fluid flow induced by nonuniform ac electric fields in electrolytes on microelectrodes. II. A linear double-layer analysis," *Physical Review E*, vol. 61, pp. 4019-4028, 2000.
- [36] N. G. Green, A. Ramos, A. Gonzalez, H. Morgan, and A. Castellanos, "Fluid flow induced by nonuniform ac electric fields in electrolytes on microelectrodes. III. Observation of streamlines and numerical simulation," *Physical Review E*, vol. 66, 2002.

CHAPTER 2

PRINCIPLE OF OPTOELECTRONIC TWEEZERS (OET)

2.1. Introduction

Electrokinetics has been widely applied in the manipulation of micro- and nano-particles. However, parallel manipulation of individual particles remains challenging due to wiring and interconnecting issues in addressing a large array of electrodes. One solution is to integrate the electrode array with addressing circuits on a CMOS chip, which increases the fabrication cost and limits the potential applications in many biological fields. Here, we propose a novel concept called optoelectronic tweezers (OET) that allow the control of electrokinetic mechanisms using direct optical images. Instead of using metal wires, OET uses optical beams to pattern virtual electrodes on a photoconductive material. This virtual electrode concept provides an elegant solution to wiring and interconnecting issues since the light beams can propagate freely in space without interfering with each other. By integrating the OET device with a spatial light modulator, million-pixel resolution optical images can be created and projected onto the photoconductive material for parallel manipulation of particles. Fig. 2-1 illustrates the relationship between optical tweezers, electrokinetics, and optoelectronic tweezers. Optical tweezers use direct optical forces for particle manipulation. It converts the energy from the optical domain directly to the mechanical domain, as the photon momentum of the focused optical beams is transferred to particles to deflect particle motion or to form a particle trap. However, the optical power required by optical tweezers is very high.

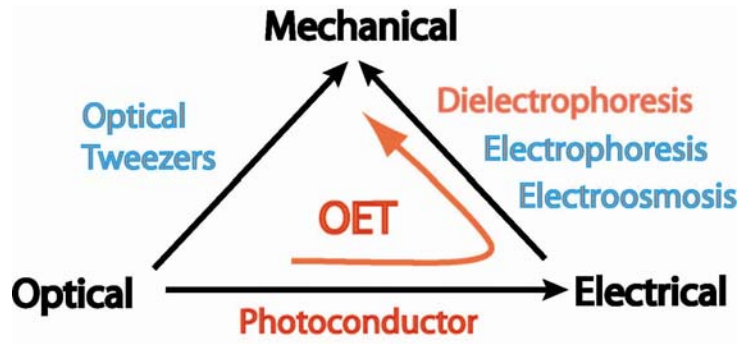


Fig. 2-1 Illustration of the energy conversion process of different manipulation mechanisms. Unlike optical tweezers and electrokinetics, OET converts optical energy to mechanical energy in an indirect way. The light in OET is used to trigger electrokinetic mechanisms for particle manipulation.

On the other hand, electrokinetics converts electrical energy directly to mechanical energy. Different electrokinetic mechanisms convert the energy in different ways. Electrophoresis controls particle motion by using Coulomb forces to attract or repel charged particles. Dielectrophoresis deflects particle motion through the interaction force between a non-uniform electric field and the field-induced electric dipoles of the particles. The particles can be either neutral or charged. Electroosmosis does not introduce a force on the particle directly. Instead, the particles are transported by the viscous force of a fluidic flow created by a liquid layer driven by surface charges and the electric field parallel to the surface. However, all of the electrokinetic mechanisms have the same wiring issues as discussed before. In order to combine the advantages of optical tweezers and electrokinetics, OET uses an indirect method of particle manipulation. The optical energy is first converted to electrical energy, triggering virtual electrodes on a

photoconductive surface. These virtual electrodes can then be used to control electrokinetic mechanisms for particle manipulation. The light-patterned virtual electrodes are reconfigurable, and can be actuated by a much lower optical power than optical tweezers. This permits OET for parallel single cell manipulation over a much larger area than with optical tweezers techniques that use focused optical field.

Light-patterned electrodes have been widely used in xerography, which was invented by Chester Carlson in 1942 [1]. In addition, optically-induced electrophoresis was used to attract charged particles on indium tin oxide (ITO) and semiconductor surfaces [2, 3] However, none of these examples has the capability of single particle manipulation.

To achieve single-cell manipulation, the light-patterned virtual electrode has to be sharply defined by the illumination light beam. This means the optically-generated electron-hole pairs must have a short diffusion length before recombining. In single crystalline silicon, the ambipolar diffusion length is $\sim 140 \mu\text{m}$. This is approximated from the diffusion length of the slow carriers ($D_{\text{ambipolar}} = 2D_n D_p / (D_n + D_p) \sim 2D_p$), holes, using the following parameters from reference [4]: hole mobility, $400 \text{ cm}^2/\text{V}\cdot\text{sec}$, and carrier lifetime, $76 \mu\text{sec}$. This means that by using crystalline silicon as a photoconductor, one cannot achieve high-resolution virtual electrodes. The carrier diffusion length has limited the minimum size of the virtual electrode to $\sim 280 \mu\text{m}$, even though the light beam can be focused to a spot size less than $1 \mu\text{m}$. Indeed, most of the indirect bandgap crystalline semiconductive materials have long diffusion lengths due to high carrier mobilities and long recombination time, and are not appropriate for patterning high-resolution virtual electrodes. For the direct bandgap III-V semiconductor such as GaAs, the short carrier

life time can reduce the diffusion length to $\sim 1 \mu\text{m}$ range even though it has high carrier mobility. The material might be cost effective.

2.2 Amorphous Silicon as a Photosensitive Material

Hydrogenated amorphous silicon (a-Si:H), which is a widely used material in the solar cell and display industries, is a good photoconductive material for patterning high-resolution virtual electrodes because of its short carrier diffusion length, and high optical absorption coefficient as compared with crystalline silicon [5, 6]. The optical and electrical properties of a-Si:H are very different from crystalline or poly-crystalline silicon. It has an optical absorption coefficient one order of magnitude larger than crystalline silicon near the maximum solar photon energy region of 500 nm. As a result, the optimal active thickness of an a-Si:H solar cell, $1 \mu\text{m}$, is much thinner than that of a single crystalline silicon solar cell [7]. The electron transport properties in a-Si:H are also profoundly affected by the high density of defect states. The electron mobility in amorphous silicon is around $10 \text{ cm}^2/\text{V}\cdot\text{sec}$, two orders of magnitude lower than that of single crystalline silicon. This results in a carrier diffusion length shorter than the diffraction limit of the optical system. Experimental data has shown that the ambipolar diffusion length in amorphous silicon is less than 100 nm [5].

The electron transport property in a-Si:H is very different from crystalline silicon because of defect states in the mid-gap and band tails of the conduction and valence bands. In amorphous silicon, the band edges are not as sharply defined as in crystalline

silicon due to the band tails. The energy band gap of amorphous silicon is around 1.85 eV, which is much higher than the 1.12 eV in crystalline silicon [8].

Figure 2-2 shows the distribution of the defect states in the energy band gap for amorphous silicon. The density of the defect states in the middle of the band gap is very high for amorphous silicon films deposited by sputtering or evaporation. The defect state density is so high that the doping of amorphous silicon is very inefficient [8]. The Fermi level is pinned at these defect states. By introducing hydrogen atoms during deposition, the defect states can be passivated, which reduces the defect density of states to the order of 10^{15} to 10^{16} $\text{cm}^{-3}\text{-eV}^{-1}$. Thus, doping becomes possible in hydrogenated amorphous silicon. The hydrogenated amorphous silicon used in this experiment (a-Si:H) is deposited by plasma enhanced chemical vapor deposition (PECVD).

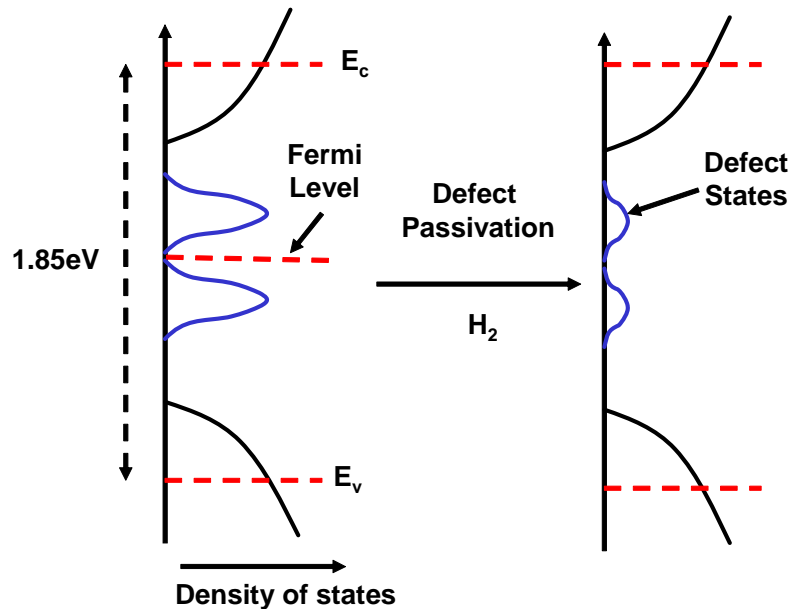


Fig. 2-2 Localized density of states in amorphous silicon. The defect density of states in the mid-gap is high, pinning the Fermi level between the two defect bands. Doping of amorphous silicon is not efficient; however, by passivating the amorphous silicon with

hydrogen atoms, the defect states can be greatly reduced to the order of 10^{15} to 10^{16} $1/\text{cm}^3\text{-eV}$, making doping possible.

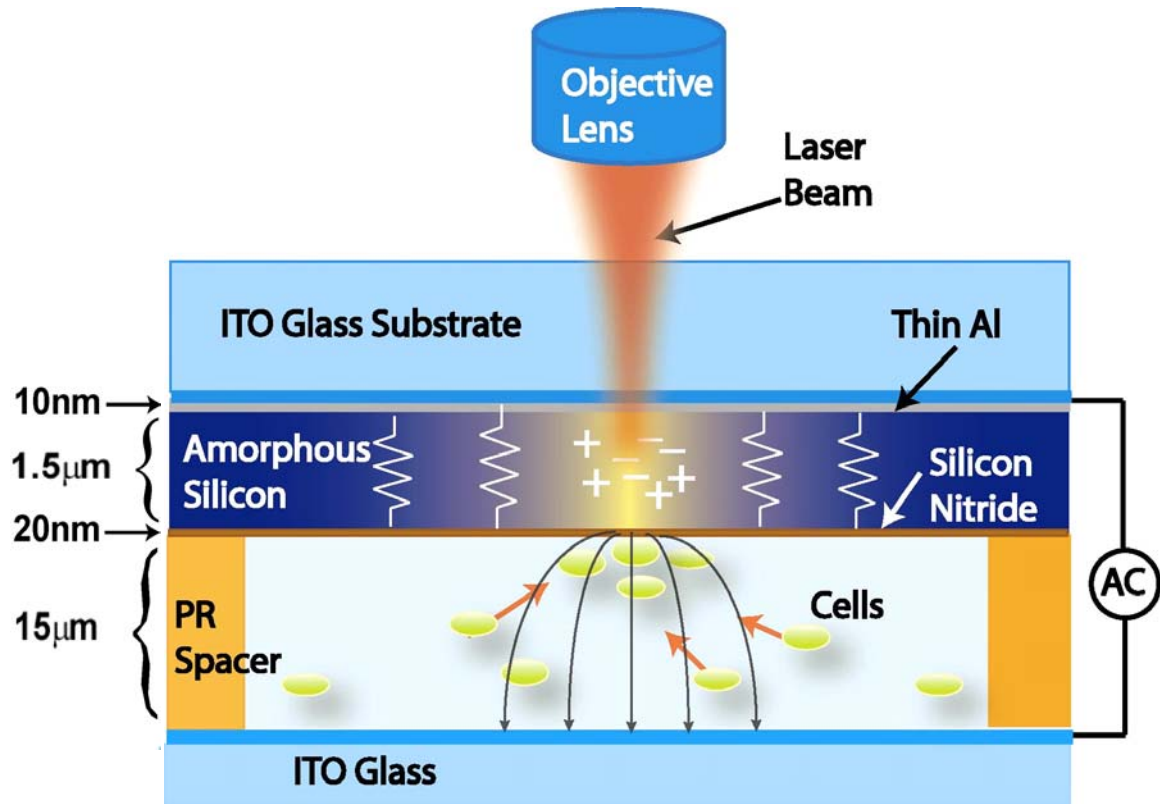


Fig.2-3 Structure of the OET device. The liquid solution is sandwiched at the chamber formed by a ITO glass and a photoconductive surface, which a glass substrated coated with multiple featureless layers including a thin Al layer to reduce the contact resistance between the ITO and the 1.5 μm amorphous silicon layer. A thin 20 nm nitride layer passivates the device to prevent potential electrolysis.

2.3 OET Device Design

The structure of the OET device is shown in Fig. 2-3. It is a sandwich structure that consists of two surfaces: transparent and conductive ITO (heavily doped Indium Tin Oxide) glass and a photoconductive surface made of ITO glass coated with multiple featureless layers including 10 nm of aluminum, 1.5 μm of intrinsic a-Si:H, and 20 nm of silicon nitride. The thickness of the chamber for the liquid solution containing the particles of interest is defined by the spacer between the top and the bottom surfaces. The chamber thickness can be adjusted to tune the electric field strength and to accommodate particles of different sizes. The aluminum layer is used to reduce the contact resistance between the ITO and the amorphous silicon layer. The thickness of this metal layer is less than 10 nm to prevent blocking of the incident light beam. The 20-nm silicon nitride layer is to prevent electrolysis during low frequency operation, which causes bubbling in the liquid layer. The insulating silicon nitride layer will not block the ac signal at high ac frequency, as it behaves as a capacitor and a high pass filter. As an ac signal is applied to the top and the bottom electrodes, the majority of the applied voltage drops across the amorphous silicon layer since it has high electrical impedance in its dark state. The dark conductivity of the amorphous silicon is around 10^{-8} S/m, allowing only a very limited electric field in the liquid layer, which produces no DEP force. When a light beam illuminates the amorphous silicon layer, the light-generated electron-holes pairs increase the conductivity of the amorphous silicon layer by several orders of magnitude, depending on the intensity of the illumination. Reported data has shown that the photoconductivity of amorphous silicon increases by five orders of magnitude under an illumination intensity of 100 W/cm^2 [9]. The increase in the conductivity of the

amorphous silicon layer shifts the majority of the voltage drop to the liquid layer as shown in the equivalent circuit model in Fig.2-4. and creates a non-uniform electric field near the illuminated spots. The cells or the particles near the illuminated spots are polarized and experience DEP forces due to the interaction of the induced dipoles and the local electric field. Particles experiencing positive DEP forces will be attracted to the illuminated spots, while particles experiencing negative DEP forces will be pushed away from the illuminated spots. The particles can be continuously addressed at any position on the two-dimensional surface by scanning the light beams across the surface.

The resolution of the light-patterned virtual electrode is limited by two factors: the ambipolar diffusion length of the carriers in the amorphous silicon layer and the optical diffraction limit of the focused light spot. The electron and hole concentration at the illuminated spot is higher than the neighboring area, resulting in lateral carrier diffusion away from the illuminated spot. In our OET device, the number of light-generated carriers is far more than the intrinsic carrier concentration in the conduction band. The numbers of light-generated electrons and holes are almost equal, resulting in an ambipolar diffusion process. The ambipolar diffusion length is mainly determined by the mobility of the slow carrier (the hole for amorphous silicon), and the recombination time of the carriers. Previous literature has reported that the ambipolar diffusion length of amorphous silicon is less than 100 nm [5]. The second limiting factor for the virtual electrode resolution is the optical diffraction limit of the optical system. From Fraunhofer diffraction theory, the minimum spot size that can be formed by an objective lens is $1.22\lambda/N.A.$, where N.A. is the numerical aperture of the objective lens. For example, $0.77\ \mu\text{m}$ is the minimum spot size that can be formed using a 633 nm laser and an objective

lens with N.A. = 1. From the above discussion, the resolution of the light-induced virtual electrode is limited by the optical diffraction limit of the objective lens, and not by the ambipolar diffusion length of amorphous silicon.

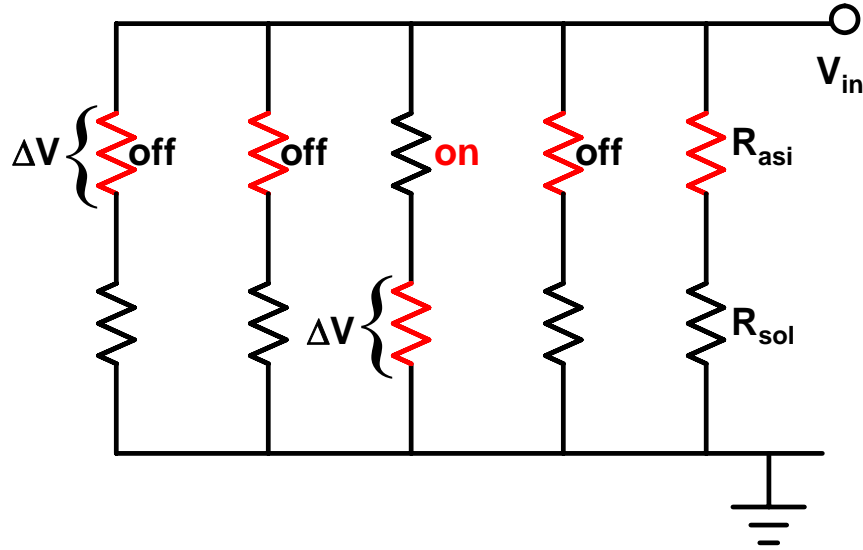


Fig.2-4 The equivalent circuit model for OET operation. At the area without light illumination, the virtual electrodes are in the off state. The majority of the applied voltage drops across the amorphous silicon layer. In the area under light illumination, the light-generated electrons and holes increase the photoconductivity of the amorphous silicon layer, switching the majority of the voltage to the liquid solution layer for DEP manipulation.

2.4 OET Device Fabrication

The fabrication process of OET device starts from a commercially available ITO coated glass with a sheet resistivity. A 1nm Al is deposited on the ITO glass using e-beam evaporation. A 1.5 μm a-Si:H layer is deposited on the Al layer using plasma enhanced chemical vapor deposition (PECVD) with deposition temperature of 275°C and

silane (SiH_4) flow rate 9 sccm. Due to the limitation of our facility, no extra hydrogen gas is added during the deposition to passivate the dangling bonds. This increases the defect density in a-Si:H and the optical power of OET actuation. On top of the a-Si:H layer is a 20 nm silicon nitride layer deposited by PECVD. This silicon nitride layer, designed to prevent electrolysis, can be removed if OET is operated in high ac frequency and low ac bias range.

To sandwich the liquid between the ITO and the photoconductive surfaces, a liquid droplet is pipetted on the photoconductive surface. The ITO glass is then glued to the photoconductive surface using double-side tape, enclosing the liquid droplet between the two surfaces and giving a spacing $\sim 100 \mu\text{m}$. To get different gap spacing, various photoresist can be spin-coated at different speed and patterned as the spacer material.

To increase the photoconductivity of the OET device, we replaced the Al layer with a 50 nm heavily doped n^+ a-Si:H to further decrease the contact resistance between the ITO and the intrinsic a-Si:H layer (This structure is shown in Chap. 4.2). This n^+ layer also reduces the loss due to the optical reflection in the metal and semiconductor interface and increases the optical transmission to the intrinsic layer. This further lowers the optical power for OET actuation. To get a better quality a-Si:H having less defect density, we have used the foundry service to deposit the n^+ and the intrinsic a-Si:H layers (SDtech Inc., <http://www.sdtech.co.kr>). The company claims the spin defect density is $\sim 10^{15} / \text{cm}^3$.

2.5 Simulated electric field distribution

We use the dc electrostatic module in FEMLAB for finite element simulations of the electric field strength and its distribution in the solution of the OET device. In this

simulation, the liquid conductivity is assumed to be 0.01 S/m and the dark conductivity of the amorphous silicon layer is 10^{-8} S/m. In the area under light illumination, we assume there is no vertical variation of the photoconductivity and the radial distribution of the photoconductivity is linearly proportional to the illumination intensity, which has a radial gaussian distribution and a FWHM spot diameter of 17 μm . The result (Fig.2-5) shows that the strongest electric field occurs near the surface of the illuminated spot. There is an electric field gradient in both lateral and vertical directions, meaning that the generated DEP forces will pull the nearby particles towards the surface of the virtual electrode if a positive DEP force is induced, or in the opposite direction if a negative DEP force is induced. To simulate the OET response to illumination power, we define a normalized photoconductivity c , which is the ratio of $\sigma_{\text{photo}}/\sigma_{\text{m}}$, where σ_{photo} is the maximum conductivity at the peak of the gaussian beam and σ_{m} is the medium conductivity.

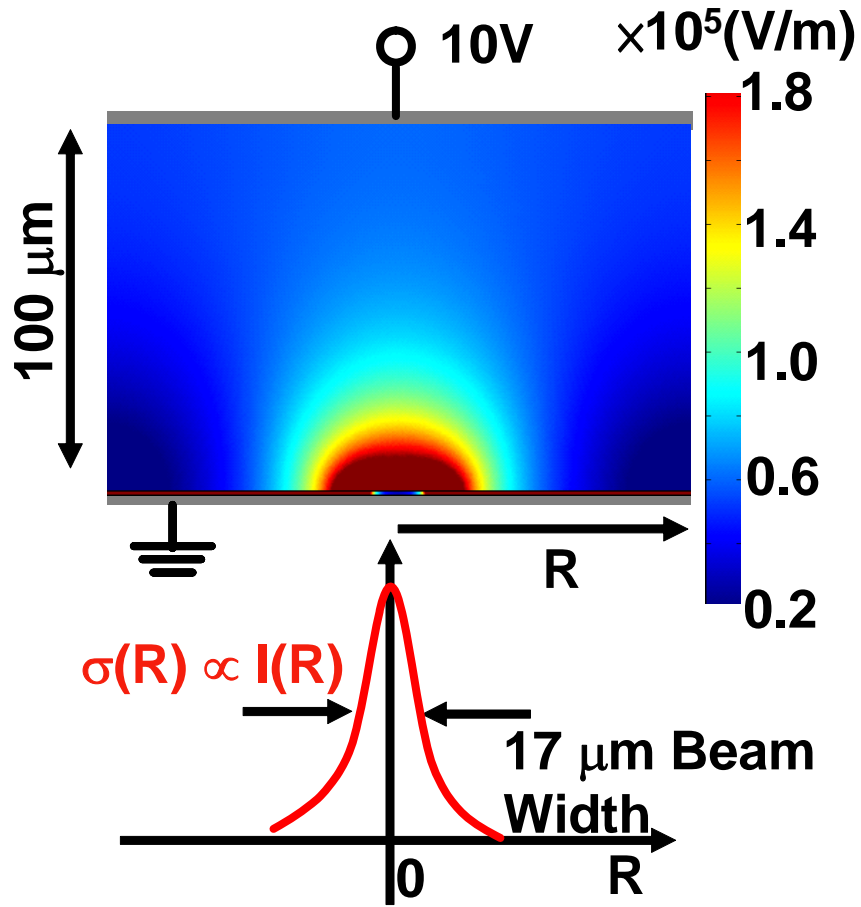


Fig.2-5 Electric field distribution in the liquid layer under light illumination. The photoconductivity in the amorphous silicon layer is assumed to be linearly proportional to the illuminated light intensity and have a gaussian distribution with a spot diameter of $17\ \mu\text{m}$.

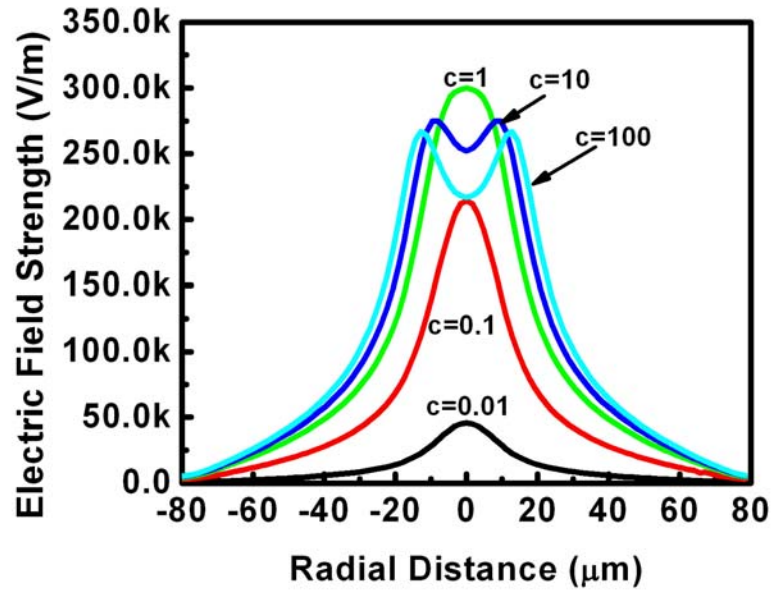


Fig.2-6 Electric field strength distribution under light illumination with different intensities at a height $5 \mu\text{m}$ above the photosensitive surface. The variable $c = \sigma_{\text{photo}}/\sigma_m$, represents the normalized photoconductivity at the peak of the Gaussian beam. The peak photoconductivity equals the liquid medium conductivity when $c = 1$.

Fig. 2-6 shows the electric field distribution in the radial direction at a height of $5 \mu\text{m}$ above the photoconductive surface for various values of c . The result shows that the electric field starts to drop across the liquid layer when the c value is larger than 0.01, meaning that a photoconductivity larger than 0.1 mS/m can activate the DEP forces in the liquid layer. The magnitude of the DEP force is proportional to the gradient of the square of the electric field (∇E^2). As the normalized photoconductivity c increases from 0.01 to 1, the gradient of the electric field and the maximum DEP force also increases. The strongest DEP force occurs at a radial distance of $15 \mu\text{m}$ to $20 \mu\text{m}$ to the center of the illuminated spot. For c larger than 1, although the size of the virtual electrode expands

with the increased optical power, the maximum DEP force remains almost constant. This can be found from the maximum slope of the electric field when $c > 1$. This implies that the virtual electrode has been fully turned on, and further increases the photoconductivity does not increase the maximum DEP forces, but only serves to increase the effective size of the light-induced virtual electrode. There is one significant difference between the curves for $c < 1$ and the curves for $c > 1$. In the case of $c < 1$, there is only one peak for the electric field distribution, meaning that the positive DEP forces can concentrate positive DEP particles to the center of the illuminated spot. For $c > 1$, a double-peak profile emerges. Positive DEP forces will concentrate the particles to the edge, not the center, of the virtual electrode. The effective range of the light-induced DEP forces is also shown in Fig. 2-6. The light-induced DEP forces extend to $\sim 80 \mu\text{m}$ in the radial direction from the center of the illuminated spot. However, the strongest DEP forces occur at a radial distance between $20 \sim 30 \mu\text{m}$ for all c values shown in Fig.2-6.

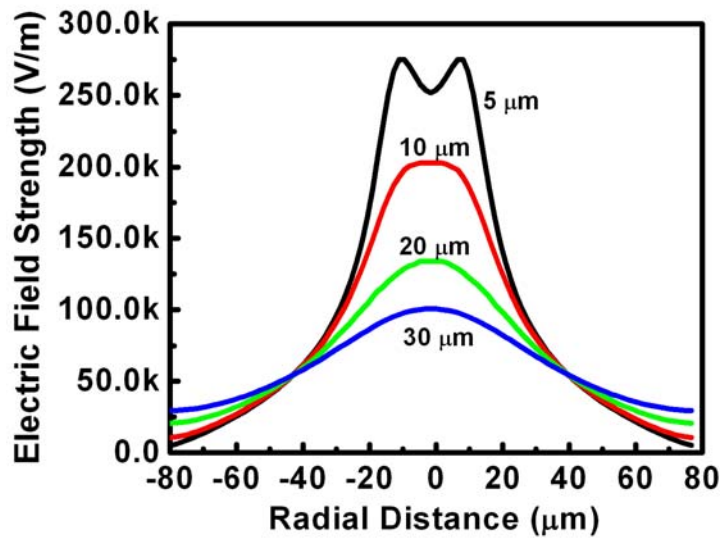


Fig. 2-7 Electric field strength distribution at four different heights above the photosensitive surface ($c=10$ in this simulation).

To understand the DEP forces in the vertical direction, the electric field strength at four different heights above the photoconductive surface for $c=10$ are plotted in Fig. 2-7. The strongest electric field occurs right above the virtual electrode, and decays in the vertical direction, resulting in a vertical DEP force that can be applied to concentrate positive DEP particles onto the photoconductive surface. Near the photoconductive surface, the electric field decays sharply in the lateral direction; however, at a position higher than $30\ \mu\text{m}$ above the photoconductive surface, the lateral gradient of the electrical field is small, resulting in a small lateral DEP force even though the electric field strength is still large. Thus, DEP manipulation of particles would only be effective at positions near the photoconductive surface in both the lateral and vertical directions.

The spacing between the top ITO electrode and the bottom photoconductive surface is an important parameter affecting the effective range of the light-induced DEP forces, the magnitude of the DEP forces, and the optical actuation of the virtual electrode. Fig. 2-8(a) shows the electric field distribution of an OET device with a reduced liquid layer thickness of $15\ \mu\text{m}$. The strongest electric field strength and the largest field gradient and DEP force still occur near the virtual electrode on the photoconductive surface, as in case of a $100\text{-}\mu\text{m}$ -thick liquid layer. However, the magnitude of the electric field is larger, and the effective range of the light-induced DEP force becomes shorter (Fig.2-8(b)). The spot size of the illuminating gaussian beam is kept at $17\ \mu\text{m}$, as in the $100\text{-}\mu\text{m}$ spacing simulation. Nevertheless, the effective range of the light-induced DEP force decreases to $30\ \mu\text{m}$, which is much shorter than the $80\text{-}\mu\text{m}$ range of the $100\text{-}\mu\text{m}$ -thick liquid layer case. The largest gradient of the electric field square (∇E^2) at $4\ \mu\text{m}$ above from the photoconductive surface is $3.2 \times 10^{16}\ \text{V}^2/\text{m}^3$, which is seven times larger

than the value $4.5 \times 10^{15} \text{ V}^2/\text{m}^3$ in the 100- μm -gap simulation. Thus, stronger DEP forces can be induced in OET devices with a thinner liquid layer.

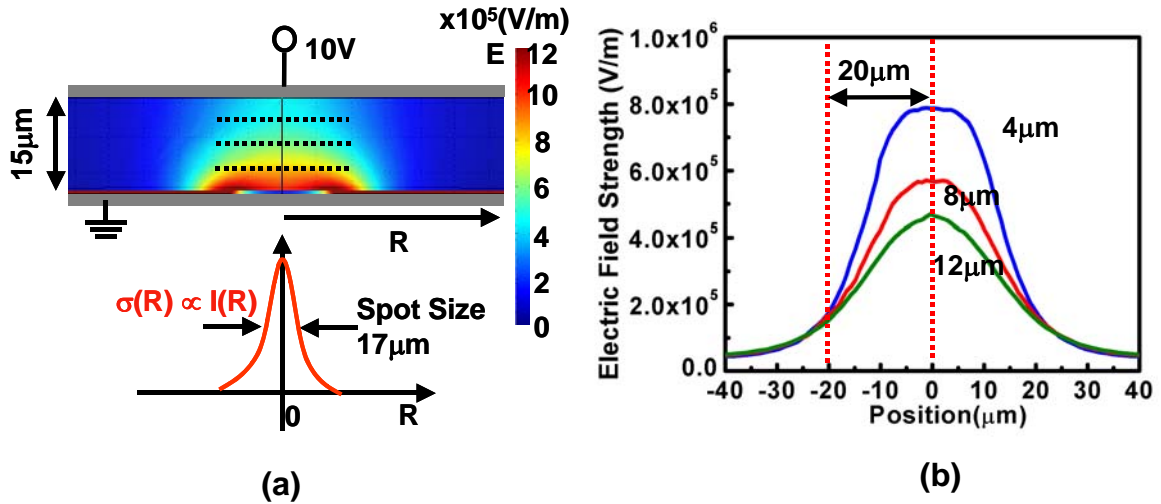


Fig.2-8 (a) Electric field distribution of the OET device with a gap of 15 μm . A normalized photoconductivity of $c = 10$ assumed in this plot. (b) The electric field strength at three different heights above the photoconductive surface. The effective range of the light-induced DEP force is less than 30 μm from the center of the illuminated spot.

Reducing the gap spacing of the OET device, however, also increases the optical power required to activate the virtual electrode. Figure 2-9(b) shows the electric field strength for normalized photoconductivity c varying from 1 to 10^4 . In the 100- μm spacing OET, $c = 1$ is sufficient to fully turn on the virtual electrode. However, in the case of 15- μm spacing OET, $c = 1$ results in a electric field that is less than 50% of the electric field of a fully turned on virtual electrode, which occurs for $c > 10$. As the virtual electrode is fully turned on, the maximum DEP force saturates and does not increase significantly, even when c is increased to 10^4 .

Figure 2-9 also illustrates the enlargement of the virtual electrode before and after the virtual electrode is fully turned on ($c = 10$). The plot is radially symmetric, so only one side of the virtual electrode is shown. In the case where $c=10^3$, the size of the virtual electrode can be determined by the peak of the electric field, which corresponds to an effective spot size of $34 \mu\text{m}$.

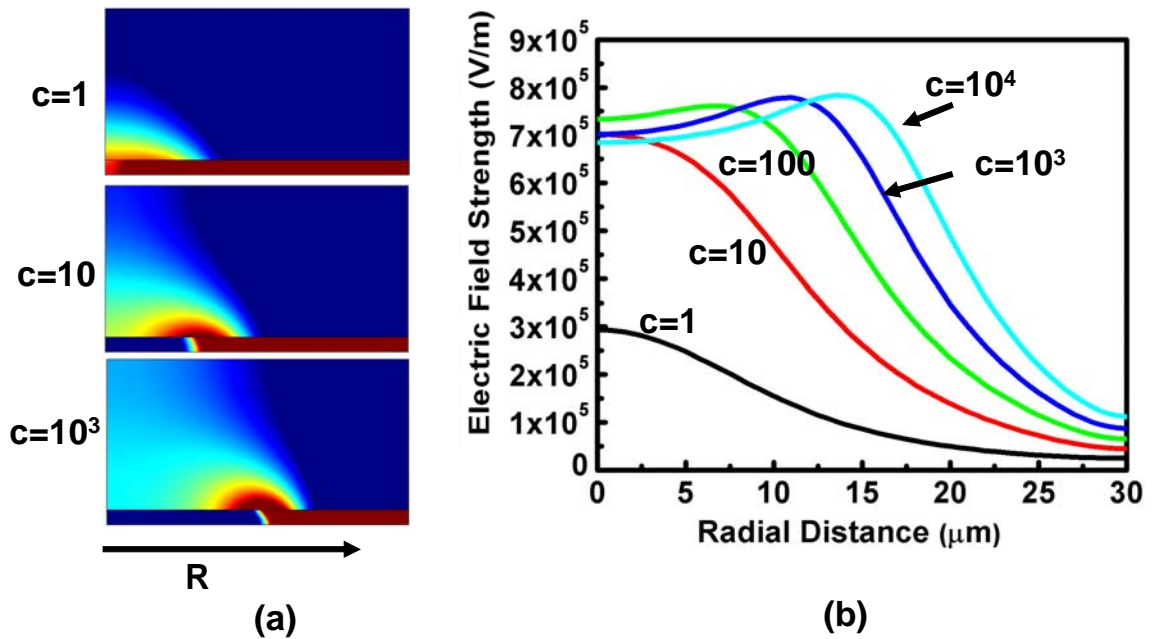


Fig. 2-9(a) The enlargement of the light-induced virtual electrode under illumination with different light intensities. (b) The electric field strength corresponding to various c values before and after the virtual electrode is fully turned on.

2.6. OET manipulation of polystyrene beads

Figure 2-10 shows the experimental setup for OET manipulation of polystyrene beads. An $800\text{-}\mu\text{W}$, 632-nm HeNe laser with a beam width of 0.24 mm is used as the actuation light source. The laser beam is scanned by a 2D galvanometer mirror

(Cambridge Technology, Inc., Model 6210), reflected by a dichroic mirror (Edmund Industrial Optics Inc.), and then focused by a 40× objective lens to generate a 17-μm light spot that is focused on the amorphous silicon layer. Neutral density filters (Newport Inc.) are used in the light pathway to control the incident optical power.

As predicted by DEP theory, the light-induced DEP forces in the OET devices can have two operation modes: positive OET can create attractive forces to pull particles towards light induced virtual electrodes, while the negative OET creates repulsive forces that push the particles away from the illuminated spots. For a 25-μm-diameter polystyrene bead, a negative DEP force is experienced at a frequency of 100 kHz in an aqueous medium with a conductivity of 0.01 S/m (Fig. 2-11). Figure 2-12 demonstrates a particle concentration function using a scanning, shrinking circular pattern.

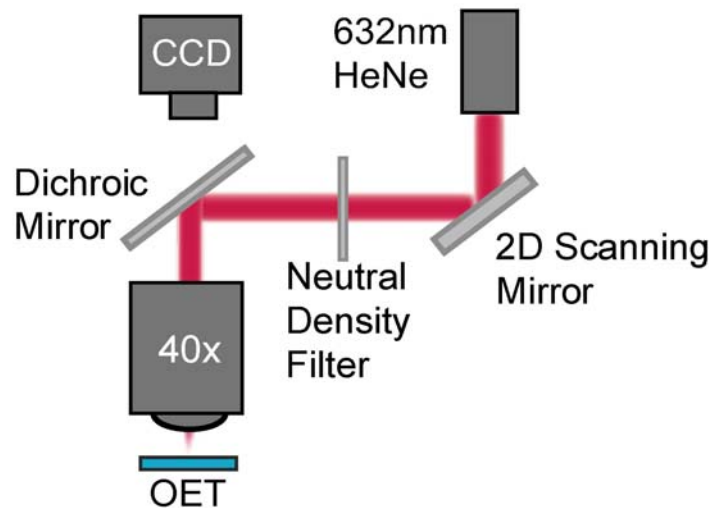


Fig.2-10 Experimental setup for OET manipulation of polystyrene beads.

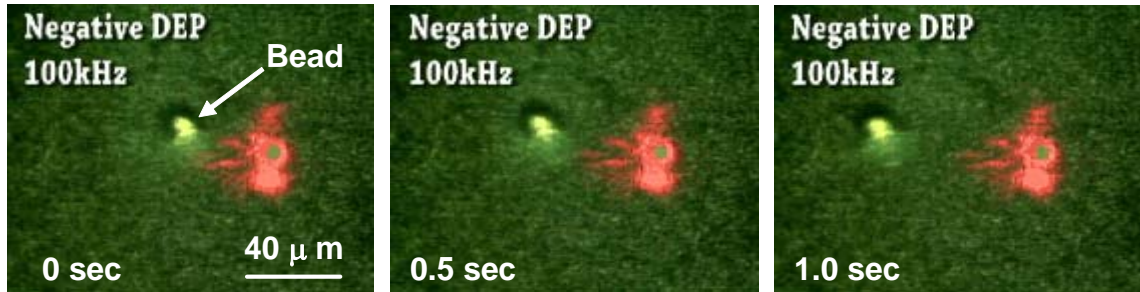


Fig.2-11 The polystyrene bead experiences a negative DEP force and is repelled away from the illuminated spot.

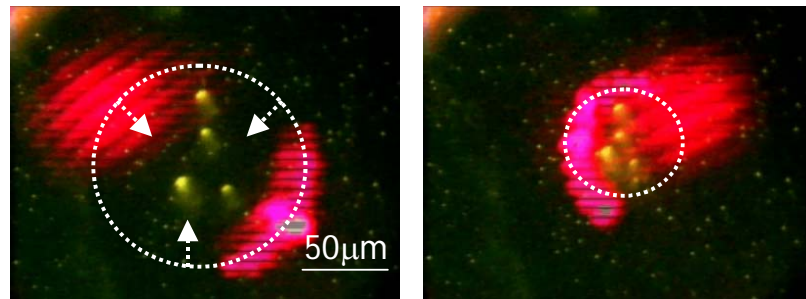


Fig.2-12 The laser beam is programmed to scan a circular pattern near the particles. As the circular pattern shrinks, the four polystyrene beads are focused to the center of the circular pattern.

To measure the magnitude of the DEP forces generated on the OET device, we apply a 10V, 100 kHz a.c. signal to operate the OET device in the negative mode on a 25- μm -diameter polystyrene bead in 0.01 S/m medium. The laser beam is programmed to scan at a constant speed to push the bead. If the scanning speed is smaller than the maximum speed that the bead can be manipulated, the bead will move at the same speed as the light beam. However, if the laser beam scans faster than the maximum speed that the bead can move, the bead will be left behind. Fig.2-13 shows the maximum speed that particle can be transported under different optical powers and ac voltages. Using a 1- μW laser beam, the bead can be actuated at a speed of 4.51 $\mu\text{m/s}$. The minimum optical

actuation intensity is as low as $3 \text{ nW}/\mu\text{m}^2$, which is 5 orders of magnitudes less than that of the minimum optical power ($1 \text{ mW}/\mu\text{m}^2$) required by optical tweezers for making a stable trap. As the optical power increases, the maximum speed also increases, reaching $397 \mu\text{m}/\text{sec}$ at a power level of $100 \mu\text{W}$. Using Stoke's Law, the DEP force induced by the light beam can be calculated from the speed of the particle as

$$F = 6\pi\eta r v \quad (2.1)$$

where η is the viscosity of the liquid ($1.002 \text{ Ns}/\text{m}^2$ for water at $20 \text{ }^\circ\text{C}$), r is the radius of the particle, and v is the velocity of the particle. Using Stoke's law, it is estimated that a light-induced DEP force of 93.4 pN is required to move a $25\text{-}\mu\text{m}$ -diameter particle at $397 \mu\text{m}/\text{s}$. When the ac voltage is reduced to 5V , the maximum particle speed decreases to one-fourth of that measured at a 10V bias, since the DEP force is proportional to the gradient of the electric field square (∇E^2).

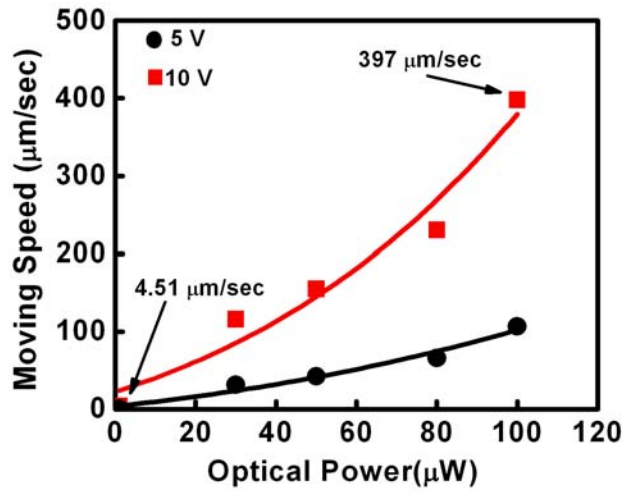


Fig.2-13 The maximum particle speed under various optical powers and applied ac voltages. The square (■) symbol represents the data for an applied voltage of 10V and the circular (●) symbol represents the data for 5V . The FWHM spot size of the laser beam is $17 \mu\text{m}$.

The optical actuation power of OET is dependent on liquid conductivity as the actuation of the virtual electrode relies on the switching of the local voltage drop from the photoconductor to the liquid layer. A liquid medium with a higher conductivity requires a higher optical power to activate the virtual electrode (Fig.2-14). In liquid with a conductivity of 2.5 mS/m, using an optical power of 50 μ W is enough to fully turn on the virtual electrode. The maximum speed saturates after the virtual electrode is fully turned on, as predicted in Fig. 2-9. As the liquid conductivity increases, the optical power required to fully turn on the virtual electrode also increases. In the medium with a conductivity of 0.01 S/m, 100 μ W of power is still not enough to fully switch the voltage to the liquid layer.

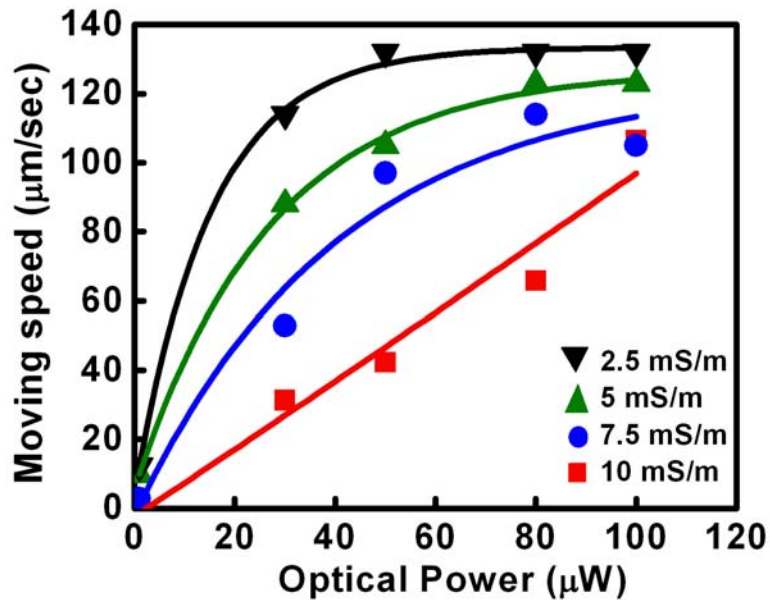


Fig.2-14 The optical actuation power for liquid media of different conductivities. The ac bias voltage is 5V. The FWHM spot size of the laser beam is 17 μ m.

2.7 OET Trapping of Live Bacteria (*E. Coli*)

The magnitude of the DEP force strongly depends on the size of the manipulated particles, as the DEP force is proportional to the particle volume. To trap small particles such as bacteria or nanoscopic particles, strong electric field gradients need to be generated to provide sufficient DEP forces for the formation of stable traps. In order to trap live *E. coli* (cylindrical shape with diameter of $\sim 0.5 \mu\text{m}$ and a few μm in length) using OET, we reduced the spacing between the ITO glass and the photoconductive surface to $15 \mu\text{m}$. The simulated electric field distribution for this device has been presented in Fig.2-8.

Figure 2-15 shows the experimental setup that allows the integration of OET manipulation and the observation of the fluorescent signals from the cells at the same time. Fluorescent detection is an important technique for biological detection and analysis. It provides biologists a quantitative tool for analyzing the status of cells. In the experiment, we use the *E. coli* cells that can express green fluorescent protein (GFP) for the convenience of observation under the fluorescent microscope. The OET system is integrated on a Nikon inverted microscope (TE 2000E). The optical actuation system is the same as the previous setup for polystyrene bead manipulation, except the observation port is now at the bottom side of the OET device. To allow the fluorescent observation, the excitation and the emission wavelengths of the optical signal need to be able to penetrate through the OET device layers. This can be achieved by positioning the amorphous silicon layer as the top layer and the transparent ITO glass as the bottom layer. Since OET can be activated by a very low light intensity, the UV lamp used to excite the fluorescent signals could also partially turn on the OET device and create leakage

currents that could turn on the virtual electrodes in regions that do not have laser illumination. This could potentially be serious for OET manipulation, depending on the light intensity and the wavelength of the excitation signals. Figure 2-16 shows the wavelength-dependent optical attenuation of the amorphous silicon layer using the absorption coefficients from [10] . Wavelengths shorter than 600 nm are strongly absorbed by the amorphous silicon, and are attenuated within 0.1 μm from the incident surface. In the OET devices, the amorphous silicon layer has a thickness of 1 μm to 1.5 μm . Optical actuation using a wavelength shorter than 600 nm thus only increases the photoconductivity near the surface of the amorphous silicon, keeping the overall conductivity of the photoconductive layer low. This keeps the virtual electrode in the off state. In most biological experiments, the excitation wavelengths of the fluorescent signals are shorter than 600 nm, and the emission signals from the fluorescent particles too weak to affect the OET operation. Thus, the effect of fluorescent excitation and emission on the actuation of OET is limited, enabling the possibility of integrating OET with a fluorescent microscope.

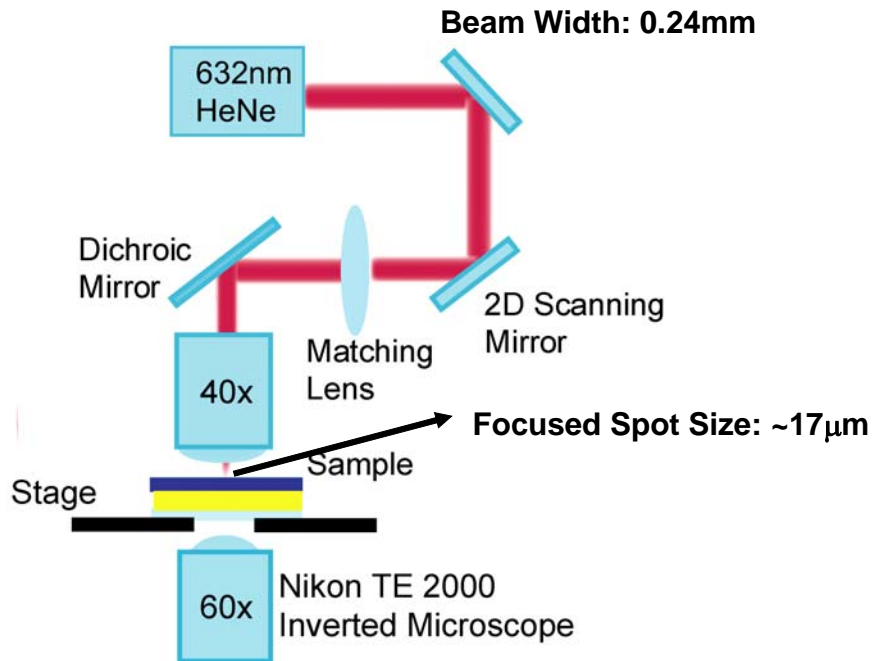


Fig.2-15 Experimental setup for OET manipulation of live *E. coli* cells. This optical system allows OET manipulation and fluorescent observation simultaneously.

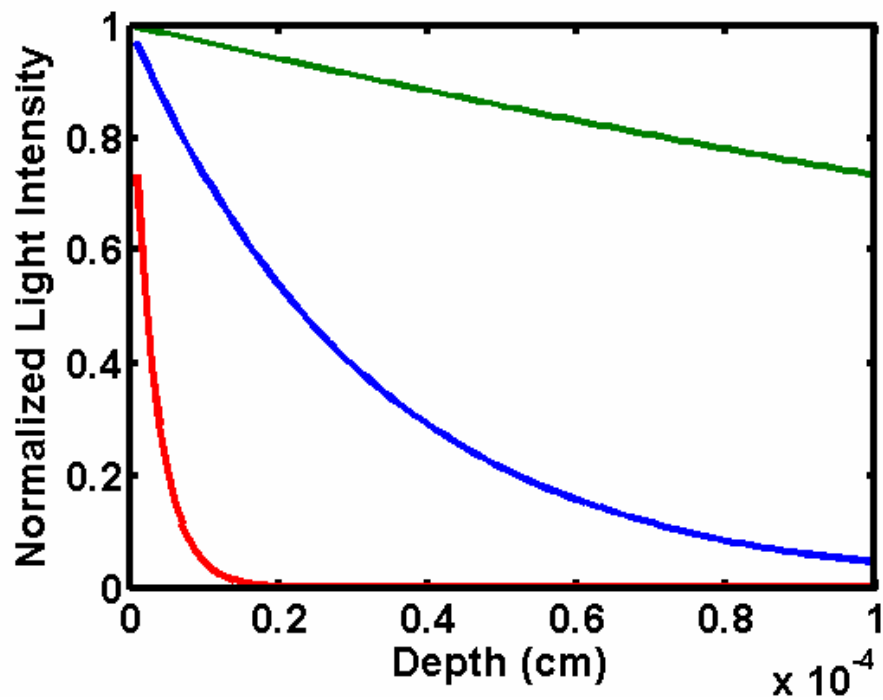


Fig.2-16 Optical attenuation of different wavelengths in the amorphous silicon layer.

Figure 2-17(a) shows the images of live *E. coli* cells under the microscope. The liquid has a conductivity of 1 mS/m. We apply a 100 kHz, 10 V_{pp} a.c. bias between the top and the bottom ITO electrodes. As the external a.c. bias is turned on, the rod-shaped *E. coli* cells align with the electric field due to the torques generated by the induced dipoles and the vertical electric field as shown in Fig.2-17(b). Under the microscope, the *E. coli* cells appear as a group of randomly distributed green spots, as only the ends of the rod-shaped cells are visible. The *E. coli* cells experience a positive DEP force at the applied bias frequency. When the laser is turned on, cells within a 20- μ m radius of the laser spot start to move towards the laser beam, and are eventually trapped at the focal spot (Fig. 2-18). Due to the electric field gradient in the vertical direction, the cells are trapped at the surface of the photoconductive surface. These trapped *E. coli* cells can be transported in a group to any position on 2D OET surface (Fig.2-19).

An interesting phenomenon we have observed is that the trapped *E. coli* cells can swim away from the trap when the laser and the electric bias is turned off. There is no significant photodamage effect to the cells even under the illumination of a visible light laser. This is a dramatic difference from cell trapping by optical tweezers using a visible light laser; a strongly-focused laser beam could damage cells instantly because of the heat generated by the intense laser beam. This phenomenon further confirms that the low optical power requirement of OET is a significant advantage in cell manipulation compared to the conventional optical tweezers.

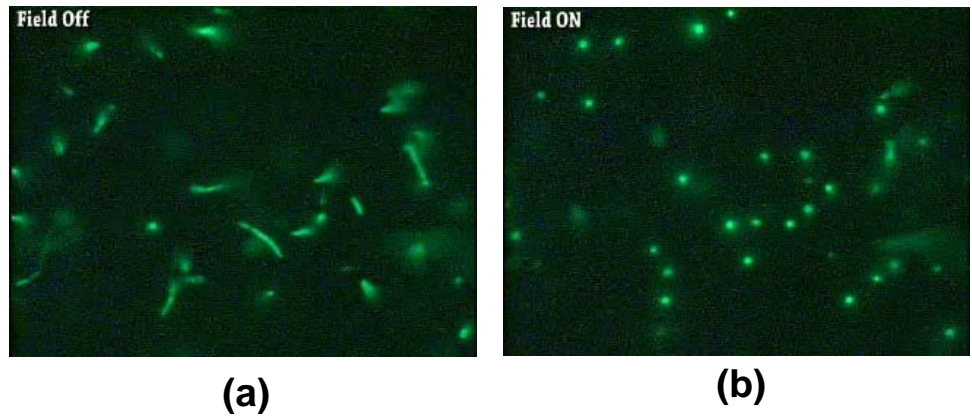


Fig. 2-17 The rod-shaped *E. coli* cells (a) before and (b) after the ac bias field is turned on. The *E. coli* cells are aligned in a direction perpendicular to the OET surface by the small leakage electric field when the external ac bias is turned on.

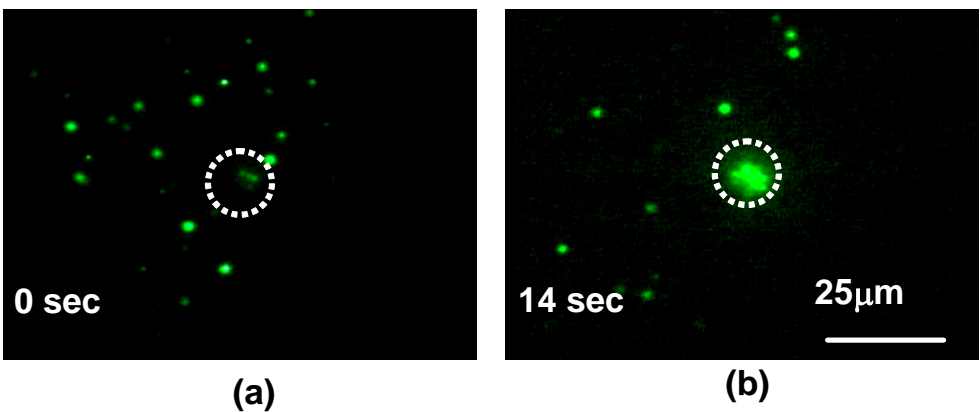


Fig.2-18 The *E. coli* cells are concentrated to the illuminated spot when the light is turned on.

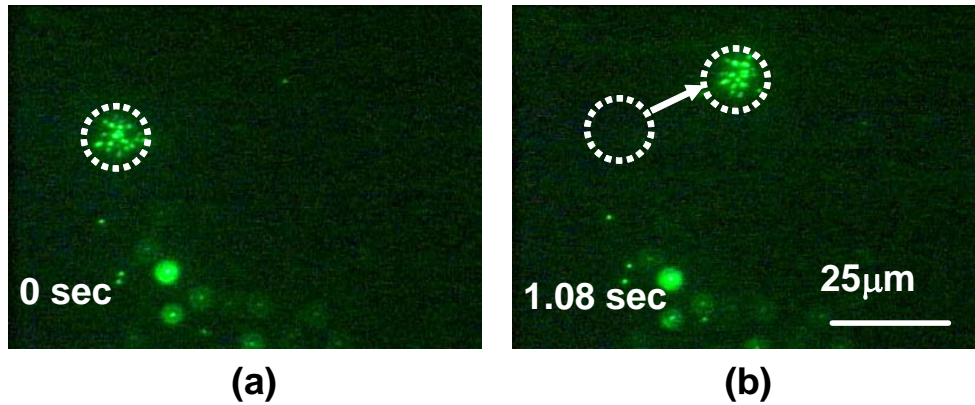


Fig.2-19 A group of trapped *E. coli* cells are transported to different positions on the two dimensional OET surface.

To study the effective trapping area and the velocity of the cells that are attracted to the traps, we recorded the trapping process and analyzed the video images frame by frame. The objective lens of the observation microscope is focused on the surface of the photoconductor to observe the trapped cells. We have measured the moving velocities of the trapped cells using laser powers of 8, 120, 400, and 800 μW , corresponding to the light intensities of 2.4, 36, 120, and 240 W/cm^2 , respectively. The OET traps work at all power levels. Figure 2-20 shows the measured velocities versus the radial distance from the trap center. At optical power of 800 μW , cells as far as 30 μm away can be trapped by the OET. The cells move at a relatively low speed at the radial distances of ~ 20 to 30 μm . The moving speed increases sharply when they close within 20 μm from the trap center, and reaches a peak of 120 $\mu\text{m}/\text{s}$ at a position around 15 μm from the center of the laser spot. This result matches very well with the simulated result in Fig. 2-8(b), which shows that the maximum DEP force occurs at a radial position around 15 μm from the center of the light spot (check the maximum slope of the curve 4 μm above photoconductor). The

cell velocity is a function of the optical power. The peak velocity increases from the 26 $\mu\text{m/s}$ at 8 μW to the 90 $\mu\text{m/s}$ at 120 μW . Above 120 μW , the peak velocity increases slowly, and eventually saturates at about 200 μW (Fig.2-20(b)). This can be explained by the following: when the optical power is lower than 120 μW , the virtual electrode is not fully turned on. Above 200 μW , the virtual electrode is fully turned on, switching most of the voltage drop to the liquid layer. Further increasing the optical power does not increase the electric field strength. However, the effective size of the virtual electrode still increases with higher optical powers. This is why the position where the peak velocity occurs is farther away from the trap center for higher optical powers.

It should be pointed out that the saturation of the photoconductivity is another reason that could cause the saturation effect of the peak velocity. If the saturated photoconductivity is not high enough to fully turn on the virtual electrode, the phenomenon of the saturation of the peak velocity and the enlargement of the virtual electrode can also be observed. The only difference would be that the magnitude of the peak velocity does not reach the value when the virtual electrode is truly turned on. The reason for photoconductivity saturation will be discussed in detail later in this chapter.

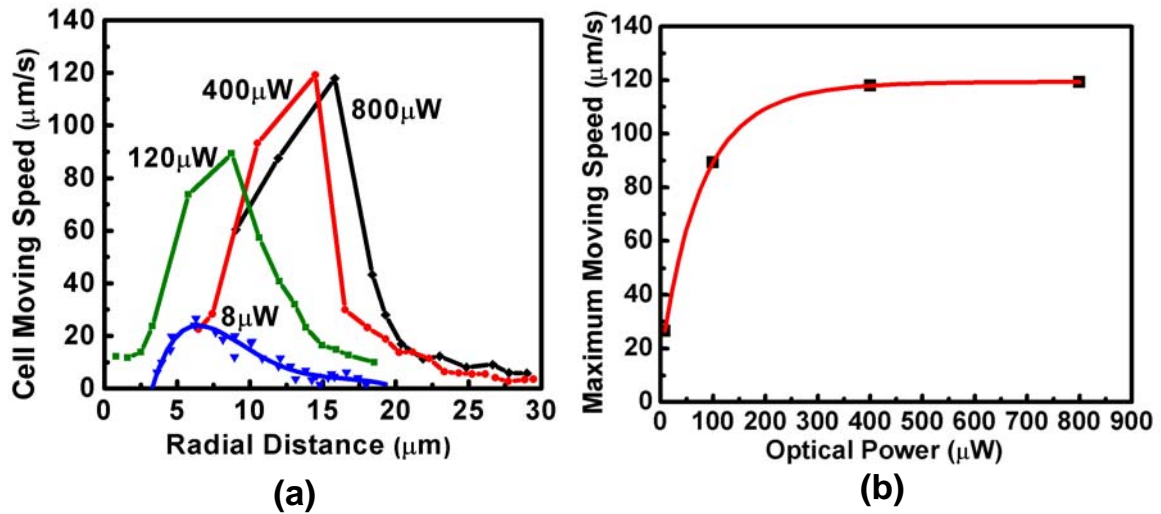


Fig.2-20 (a) The moving speed of the *E. Coli* cells toward the center of the focused light spot. R is the radial position of the cell (b) The saturation of the peak velocity at high optical power levels.

The simulated trapping forces for *E. Coli* cells at different radial positions is shown in Fig. 2-21(a). The factor $c = \sigma_{\text{photo}}/\sigma_{\text{m}}$ represents the normalized photoconductivity of the amorphous silicon layer. The electric field distribution is extracted from Fig. 2-8(a) at 3 μm height above the photosensitive surface to calculate the DEP forces. The size of the *E. coli* cell is approximated by a 2.7- μm spherical bead and the real part of the CM factor is assumed to be 1. To compare the simulated results with the experimental results of Fig. 2-20, the DEP force is converted to a cell transport speed using Stoke's Law. A 2.7- μm particle moving at a speed of 100 $\mu\text{m/s}$ experiences a 2.54 pN viscous force in the microfluidic environment. The simulated result in Fig. 2-21(a) shows the same trend as the experimental data in Fig. 2-20(a). The peak velocity

increases with optical power at low power levels, and eventually saturates at high optical power levels. The positions where the peak velocities occur increase with optical power, due to the virtual electrode enlargement effect. However, the saturation of the peak velocity occurs at a lower photoconductivity in the simulated results. The curve of the optical power of 120 μW matches with the simulation curve $c = 1$. From $c = 1$ to 10, the maximum speed still increases as the c value increases; however, the experimental data has shown saturation at 400 μW . This implies that the photoconductivity might saturate at a level between 120 μW to 400 μW and the virtual electrode is not fully turned on. Further increasing the optical power does not increase the photoconductivity and the DEP forces.

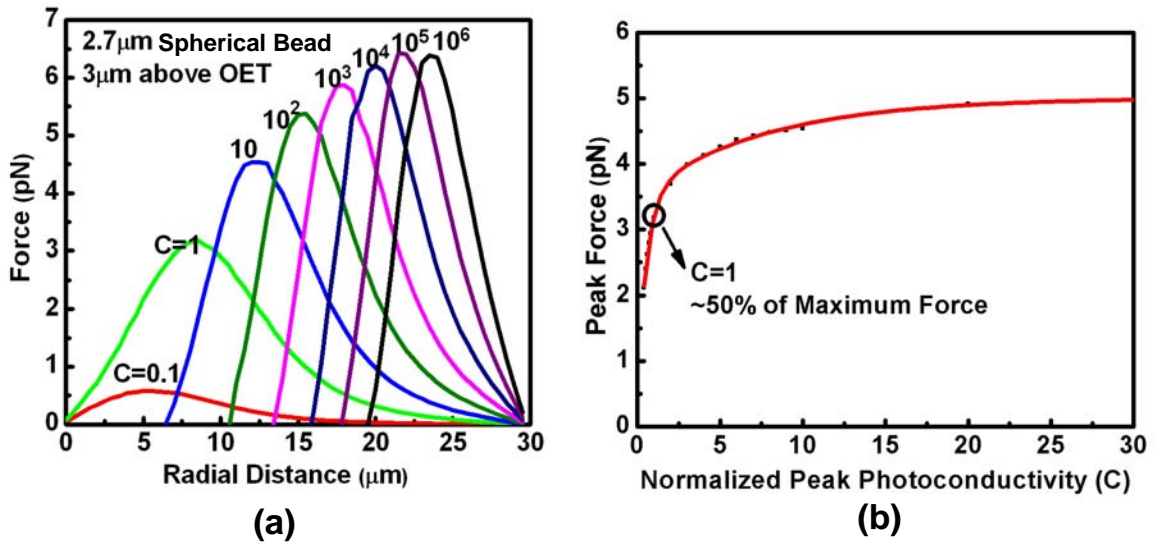


Fig.2-21 (a) The simulated trapping forces for *E. coli* cells approximated with 2.7- μm latex beads. The factor $c = \sigma_{\text{photo}}/\sigma_{\text{m}}$ is the normalized photoconductivity (b) The peak trapping force is shown as a function of the normalized photoconductivity.

2.8 AC Frequency Range for OET Operation

OET devices consist of multiple featureless layers including a 1~1.5 μm amorphous silicon layer, a 20 nm nitride layer, and a liquid solution layer that can be varied from 10 μm to 100 μm depending on the application (Fig. 2-22(a)). Between the interface of the solid and liquid layer, there is an electric double layer (EDL) which behaves as a capacitor. When an external a.c. bias is applied through the top and the bottom electrodes, these multiple layers can be modeled as serially connected lumped circuit elements (Fig. 2-22(b)). In ideal OET operation, all the applied voltage drops across the amorphous silicon layer in the dark; under illumination, all the voltage is dropped across the liquid layer. However, in a more realistic model, some of the voltage may drop across the liquid layer in the dark, creating a leakage electric field. Under light illumination, some of the voltage may drop across the insulating layers or the EDL, decreasing the electric field strength and the DEP forces induced in the liquid layer. To solve these issues, the thickness of the insulation layer and the frequencies of the applied signals need to be carefully selected.

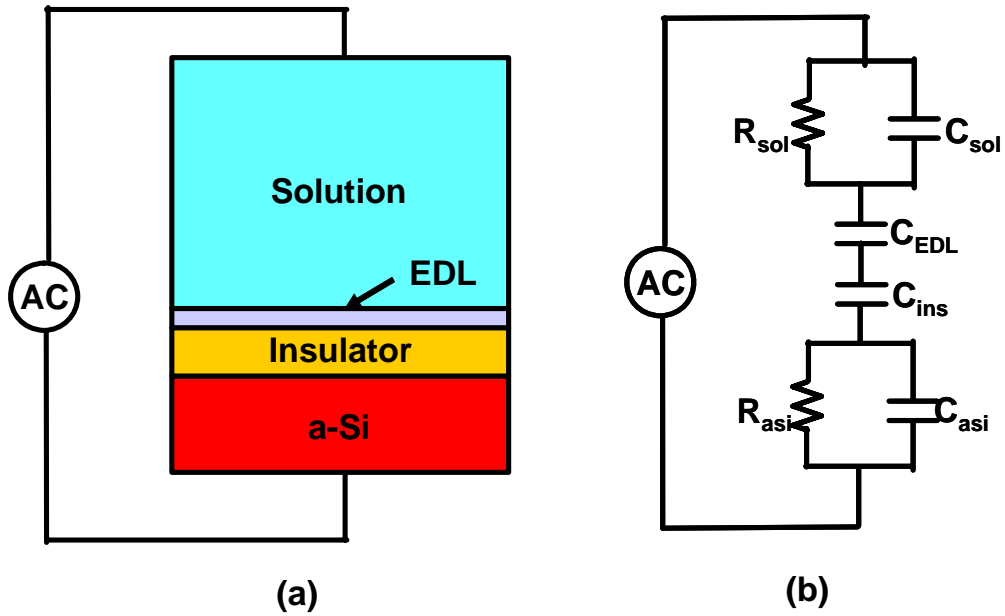


Fig.2-22 (a) Schematic and (b) equivalent circuit model for the OET device. The multiple featureless layers are modeled as serially-connected lumped circuit elements.

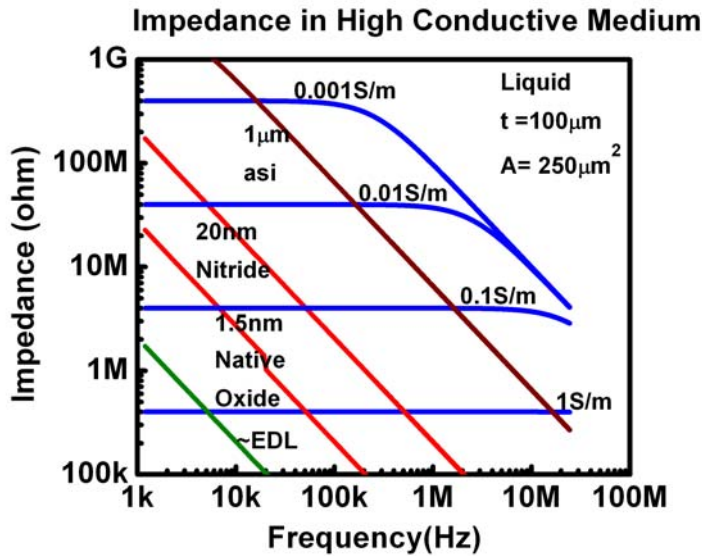


Fig.2-23 The calculated impedance of the multiple layers in the OET device. The thickness of the liquid layer and the device area are assumed to be $100\ \mu\text{m}$ and $250\ \mu\text{m}^2$, respectively. The thickness of the EDL is assumed to be $4\ \text{nm}$, corresponding to an electrolyte concentration about $10\ \text{mM}$.

Figure 2-23 shows the calculated electric impedance for the serially-connected lumped elements using the following parameters: the relative permittivities, ϵ_r , of water, silicon nitride, silicon dioxide, and amorphous silicon are 78, 7, 4, 11, respectively, and the dark conductivity of the amorphous silicon is 10^{-8} S/m. The conductivity of the insulating layer and the electric double layer is assumed to be negligible. The thickness of the liquid layer is 100 μm and the thickness of the double layer is 4 nm, which corresponding to an electrolyte concentration around 10 mM. The area of the device is 250 μm^2 . The impedance of the liquid solutions with conductivities from 1 mS/m to 1 S/m is also shown in the plot.

To avoid the leakage of the electric field to the liquid layer without illumination, the dark impedance of the amorphous silicon layer must be an order of magnitude larger than that of the liquid layer. Since amorphous silicon is not conductive in the dark, the dark impedance is mainly dominated by the capacitive term at frequencies above 10 kHz. This capacitance decreases as the frequency increases. The liquid layer impedance is dominated by the resistive term in the low frequency range, but becomes dominated by the capacitive term in the high frequency range. In a solution with a conductivity 0.01 S/m the impedance has a constant value below 1 MHz. As the frequency increases above 1 MHz, the impedance begins to decrease. The impedance curve of the amorphous silicon intersects the 0.01 S/m liquid curve at the frequency of 200 kHz. Below this frequency, the dark impedance of the amorphous silicon layer is larger than the liquid layer and the OET device can operate. Above this frequency, more than 50% of the voltage will drop across the liquid layer even in the dark state. The voltage that can be switched between

the amorphous silicon layer and the liquid layer is small, and the OET device does not work well. The situation of electric field leakage is better in solutions with a higher conductivity; however, it also takes a higher optical power to activate OET in these media.

To avoid voltage drops across the insulating layer, the frequency needs to be high enough so that the impedance of the insulator is lower than the liquid layer. In the 0.01 S/m medium, the impedance line of the liquid intersects the impedance line of the 20-nm nitride layer at 4 kHz. Below this frequency, more than 50% of the voltage that is meant to be switched to the liquid layer will be dropped across the nitride layer. This effect becomes more serious when operating OET in high conductivity media. For a 1 S/m medium, we need to operate OET at a frequency above 500 kHz to avoid this effect.

Apparently, there is an optimal frequency window for OET manipulation that avoids field leakage in the dark and the excessive voltage drop across the insulator in the bright state. For a 0.01 S/m medium, this window is between 4 kHz to 200 kHz. To increase the frequency window of OET operation, the insulation layer can be removed as long as electrolysis does not occur. In some cases where the surface modification is necessary, the thickness of the coated layer should also be considered.

2.9 Photocurrent Measurement and Simulation of OET

The operation frequency range of OET devices is 10 kHz to 1 MHz. In this frequency range, the interface capacitance formed by the electric double layer or the thin insulation layer is a short circuit. This simplifies the equivalent circuit model for OET analysis (Fig. 2-24). The external applied voltage is switched only between the bulk

liquid layer and the photoconductor. Since the photocurrent of the photoconductor is usually not a linear function of the applied bias and the optical power, load line analysis on the I-V curve is necessary to understand the effective voltage drop across the liquid layer under different applied voltages and optical power levels.

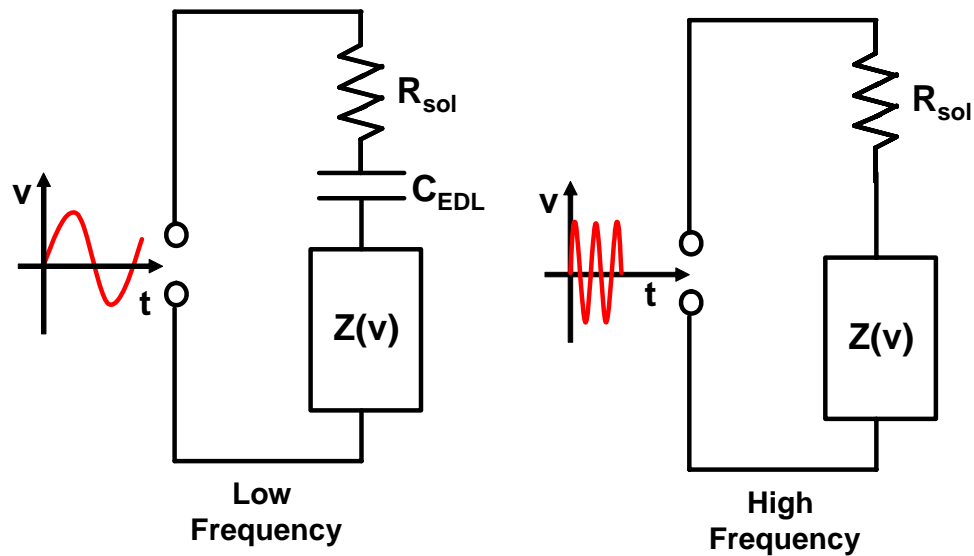


Fig.2-24 The equivalent circuit model for OET operation. The interface capacitances such as the double layer capacitance become a short circuit for high frequency operation.

Figure 2-25 shows an example of the load line analysis on the I-V curves of the photoconductor under different optical power levels. The load lines are the straight lines with negative slopes, representing passive resistances with values determined by the liquid conductivity and the gap between the top and the bottom photoconductor. A load line with a larger slope represents a more conductive medium.

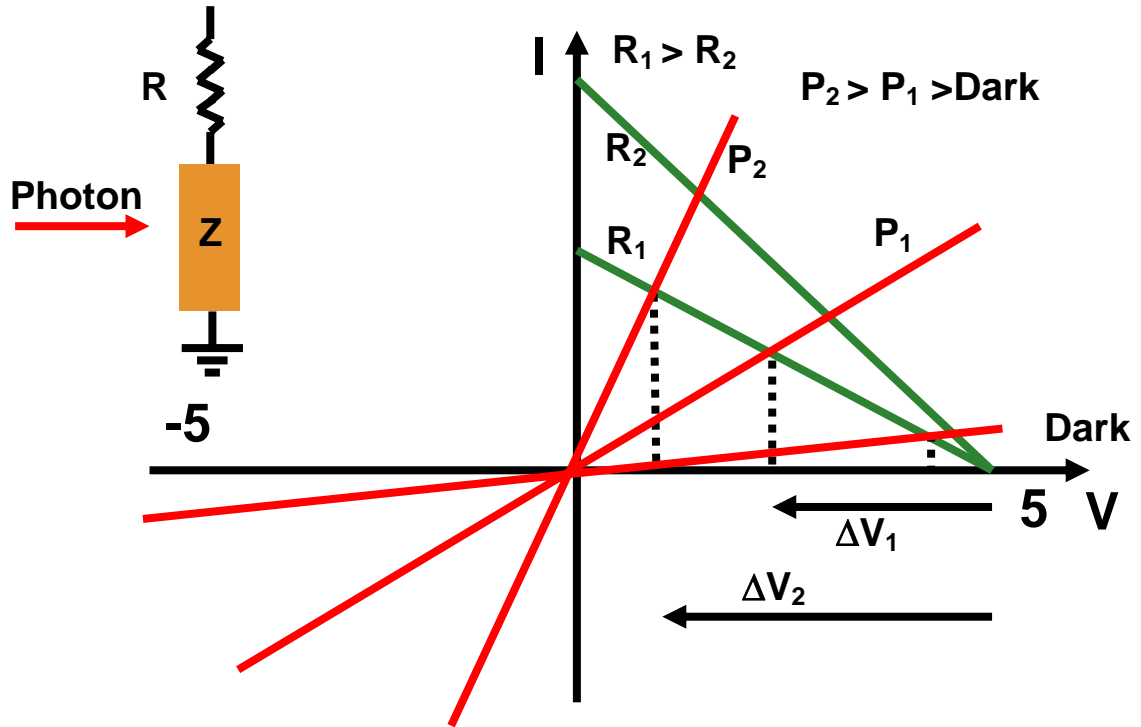


Fig.2-25 Load line analysis on the I-V curve of the photoconductor. The slope of the load line depends on the liquid conductivity of the solution and the thickness of the gap between the top ITO glass and the bottom photoconductor. A small slope represents a load line with large resistance. ΔV_1 , ΔV_2 are the effective voltages dropping across the liquid layer when the optical power is P_1 , and P_2 , respectively.

The effective voltage drop across the liquid layer is equal to the difference between the voltage at the intersection of the load lines and the I-V curve corresponding to a certain optical illumination power and the bias voltage. For example, to create an effective voltage ΔV_1 in a liquid layer with a resistance R_1 , the illumination power needs to reach P_1 . To create an effective voltage ΔV_2 , an optical power needs to go up to P_2 . Fig.2-25 also shows that for a load line having a smaller resistance R_2 , the effective

voltage that can be switched to the liquid layer under the same optical power is smaller than that of the load line having a higher resistance R_1 .

During OET operation, a signal with a large ac bias and zero dc bias is applied to provide a sufficient DEP force for particle manipulation. In the load line analysis, this means that the load line sweeps from the positive bias region to the negative bias region. No dc bias is applied since the dc bias will be filtered out by the interface capacitance and will probably create electrolysis at the photoconductor interface.

Electrical characterization of the OET device is challenging since it is operated in a large signal ac bias. Exact characterization of the electrical properties of the OET device is difficult since most of the current commercially available equipment such as impedance analyzers or LCR meters only provide small signal analysis functions. Instead, we have used some indirect methods to characterize the OET devices.

To measure the I-V curves of the OET devices for load line analysis, we have adapted a modified OET structure which replaces the interface capacitance with an ohmic contact electrode as shown in the inset of Fig. 2-26. This does not interfere with characterization; since OET operates at a high frequency, the interface capacitances between the liquid and the photoconductor are modeled as short circuits. This adapted OET structure also has the same multiple layer structure of the original OET device, except the top nitride layer is replaced by a 50-nm N^+ a-Si:H layer and an aluminum layer. The function of the N^+ layers is to reduce the contact resistance between the electrode and the intrinsic amorphous silicon layer. The thickness of the intrinsic layer is kept the same as the real OET device. Optical illumination is introduced from the lower ITO glass surface. Fig. 2-26 shows the I-V curve of this adapted structure under illumination of 51

mW/cm² light intensity. The light source is a 625-nm LED. The data shows that the photocurrent decays as the illumination time increases. In Fig. 2-27, we plot the photocurrent at the 5 volt bias as a function of time. A 38% decay of the photocurrent has been observed after 80 minutes of illumination. This decay of the photocurrent comes from the light-induced defect states in the amorphous silicon. The decay of the photocurrent could affect the OET operation by decreasing the effective voltage drop across the liquid layer when the light intensity is low. We will show the effect in Chap. 4 when discussing the particle sorting using an integrated virtual optical machine. However, the decayed photocurrent can be recovered by annealing the device at 150°C for 1 hour [11]. A load line representing a liquid conductivity of 0.01 S/m is drawn on the I-V curves to show the effective voltage drop across the liquid layer under this illumination (Fig. 2-26). Illumination at this light intensity can switch 3V of the applied 5V to the liquid layer.

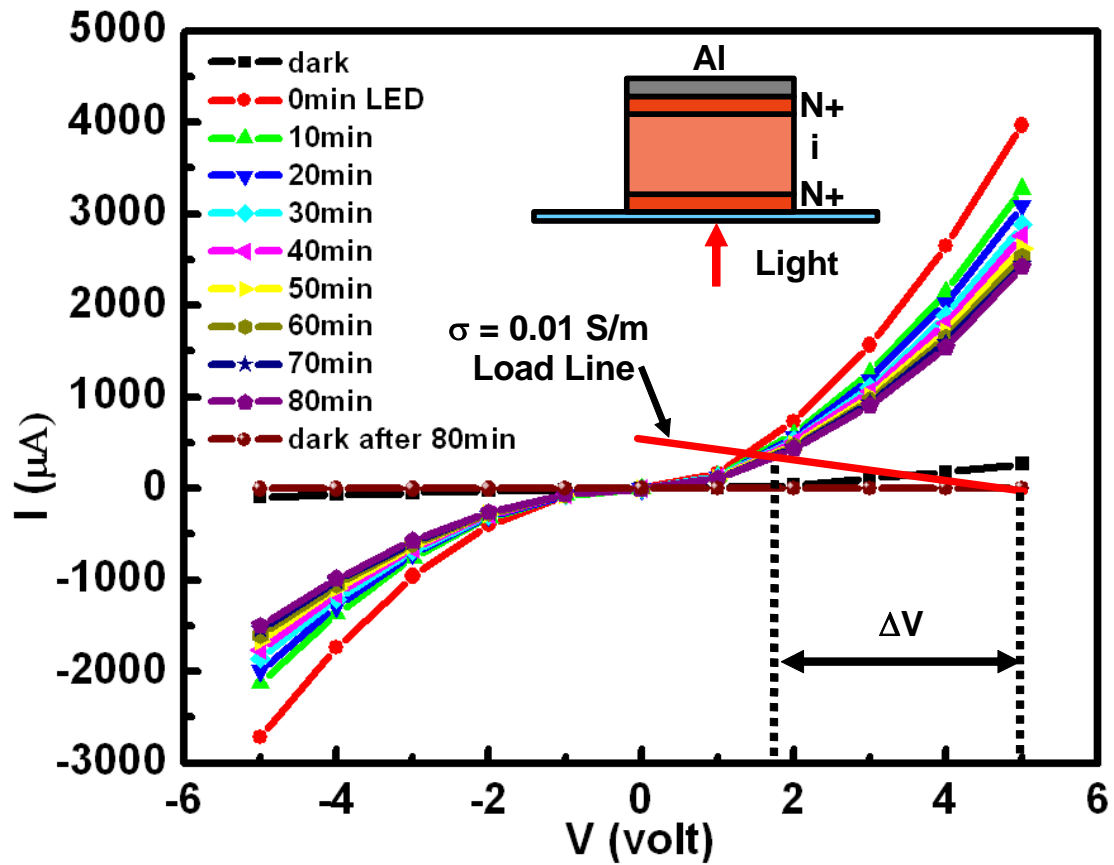


Fig.2-26 The I-V curves of the adapted structure (inset diagram) in dark and under the illumination of a 625-nm light source at an intensity of 51 mW/cm². The photocurrent shows long-term decay as the illumination time increases. The load line representing a liquid conductivity of 0.01 S/m is drawn to show the effective voltage drop across the liquid layer under this illumination.

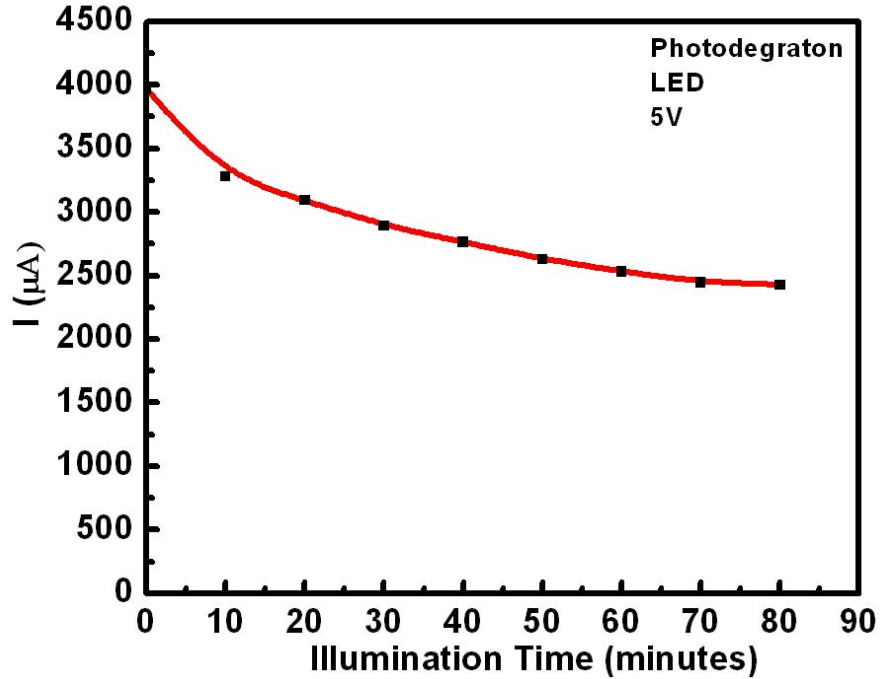


Fig. 2-27 The photocurrent decay as the illumination time increases. The data is extracted from Fig. 2-26 at 5V bias. There is a 38% photocurrent decay after 80 minutes of illumination.

The thickness of the intrinsic layer is critical for OET operation. In the interface of the N^+ layer and the intrinsic layer, there exists a built-in space charge region so that the Fermi level at the N^+ layer and the intrinsic layer aligns in the equilibrium dark state. Since the intrinsic layer is undoped, the depletion width is controlled by the defect density of states. For a defect density of states at the level of 10^{15} cm^{-3} , the space charge zone has a thickness of around $0.69 \mu\text{m}$ for a built-in potential of 0.4 volt. In the $N^+ \text{-i-} N^+$ structure, the two space charge zones overlap, resulting in the lowering of the barrier of the intrinsic layer as shown in Fig. 2-28 and the increase of the dark conductivity of the photoconductor. When the intrinsic layer is too thin, the dark conductivity of the

photoconductor becomes too high to hold the external applied voltage of the OET device in the dark state. We failed in operating OET devices with intrinsic layer of 0.5 μm . The whole OET surface was turned on in the dark state.

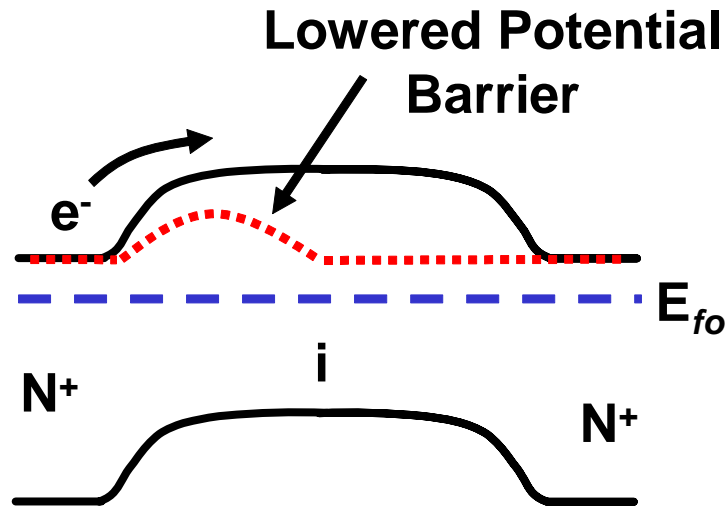


Fig. 2-28 The band diagram of the $n^+ - i - n^+$ amorphous silicon structure. When the intrinsic layer is too thin, the two space charge regions overlap which reduces the potential barrier and increases the dark conductivity of the photoconductor.

The maximum voltage that the OET device can operate depends on the dark current level. The dark current in the amorphous silicon device is controlled by the space-charge-limited current due to the defect density of states in the intrinsic layer [12]. The dark I-V curve is not linear. The dark conductivity at a high bias is much lower than that of a low bias. Fig. 2-29 shows the simulated dark I-V curve of an $n - i - n$ structure with a 1- μm thick intrinsic layer. The simulation is done using ISE TCAD. When the operation voltage is at 5V, the leakage voltage in the dark state is 1V for a load line representing a 0.01 S/m medium. However, the leakage voltage goes up to 7V when the bias is 15V.

More than 50% of the applied voltage will drop across the liquid layer in the dark state for the same load line. A thicker intrinsic layer is required to increase the OET operating voltage and provide larger DEP force for particle manipulation. A thicker intrinsic layer also prevents the overlap of the two space charge regions and lowers the dark conductivity of the OET device. Considering the optical absorption depth of the amorphous silicon, the optimal thickness of the intrinsic layer of for an OET device is around $1.5 \sim 3 \mu\text{m}$.

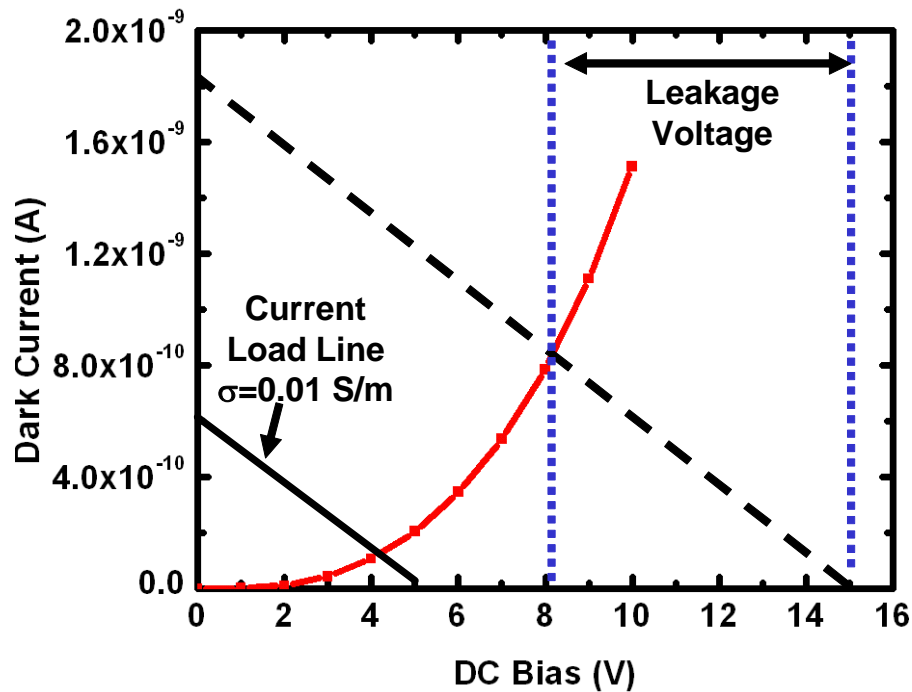


Fig. 2-29 Simulated dark current of the n-i-n structure with an intrinsic layer thickness $1 \mu\text{m}$. The dark conductivity at the high bias is much smaller than that of the low bias. A significant amount of the applied voltage has dropped across the liquid layer in the dark state when a high bias is applied.

The current OET device is not effective in manipulating particles in a medium with a conductivity higher than 0.01 S/m. We have observed a photocurrent saturation effect in our current OET device. Fig. 2-30 shows the maximum speed of a 20- μm -diameter polystyrene particle pushed by an optical beam at different medium conductivities under various optical power levels. The speed of the particle is directly proportional to the DEP force ($\sim \nabla E^2 \sim V^2/L^2$, where L is the characteristic length) induced by the optical beam. The speed measurement could be a good indicator of the effective voltage drop across the liquid layer induced by the optical beams. As shown in Fig.2-30, for an optical power lower than 600 μW , the maximum speed increases with the optical power, except for the 0.01 S/m medium. This decrease is caused by the photodegradation effect, as the 0.01 S/m solution was the first medium tested on the OET device. The maximum speed saturates at optical powers higher than 600 μW , all four tested media conductivities. However, the saturated maximum speed in the low conductivity medium is higher than that of the high conductivity medium. The saturation light intensity is 73 W/cm^2 , corresponding to a 600- μW optical beam with a beam size of 4.8 $\mu\text{m} \times 170 \mu\text{m}$. This light intensity also matches with the previous data of *E. coli* trapping in Fig. 2-20(b), which shows a saturation light intensity of 69 W/cm^2 , corresponding to a 200- μW optical beam with a spot size of 17 $\mu\text{m} \times 17 \mu\text{m}$.

The saturated photoconductivity can be found by using the saturated particle speed and the liquid conductivity in Fig.2-30. The maximum speed obeys the following relation:

$$v \sim \left(\frac{R_{liquid}}{R_{photo} + R_{liquid}} V \right)^2 \quad (2.2)$$

where R_{photo} is the saturated resistance of the photoconductor, R_{liquid} is the resistance of the liquid layer, and V is the applied voltage. By assuming the photoconductivity saturate at 8.8×10^{-4} S/m, the curve generated using Eq. (2.2) can fit the experimental data well (Fig.2-31). In this curve fitting, we use the saturation speed at the optical power of 600 μW . This data also confirms that the maximum speed saturation effect observed in Fig. 2-20 is caused by the saturation of the photoconductivity. The saturated photoconductivity of 8.8×10^{-4} S/m corresponds to $c = 0.88$.

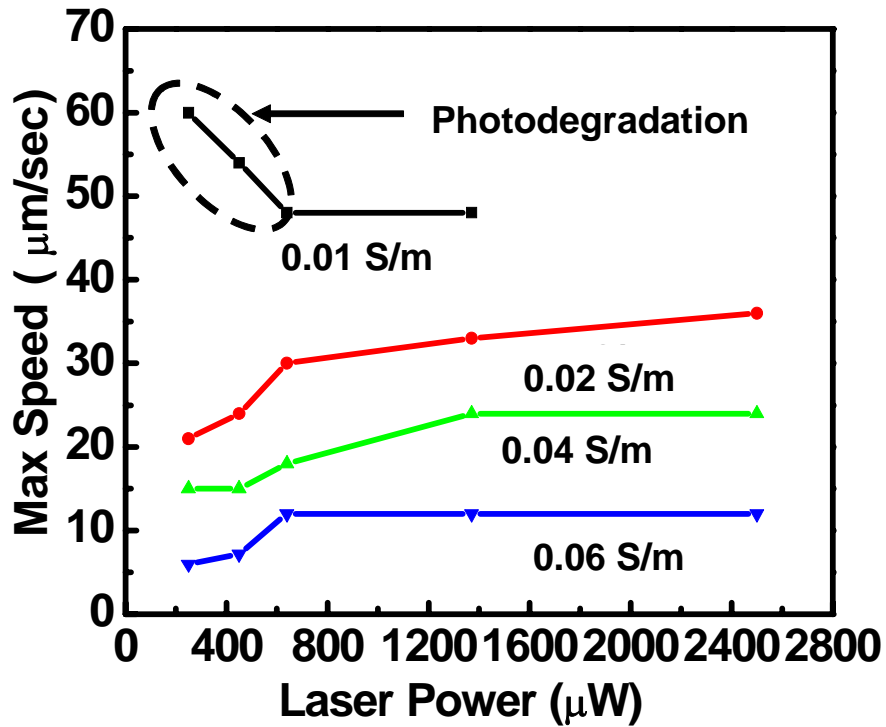


Fig.2-30 Speed measurement using a 20- μm -diameter particle in media with different conductivities under the various optical illumination levels. The optical beam has a linear-shape with a beam size of $4.8 \mu\text{m} \times 170 \mu\text{m}$. The gap spacing of this experiment is 100 μW .

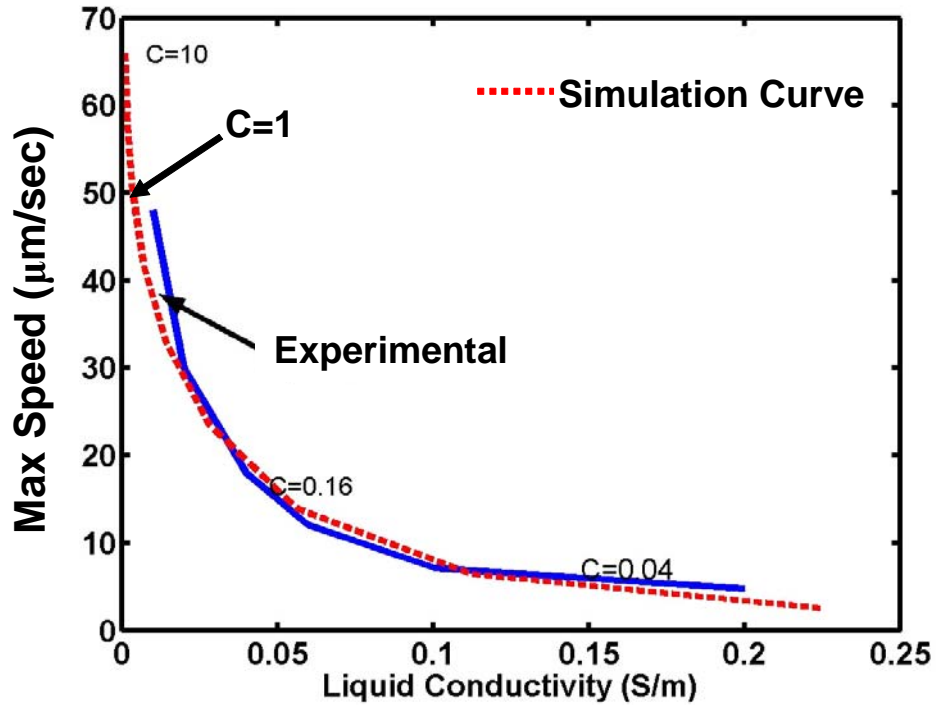


Fig. 2-31 Curve fitting of the experimental data in Fig. 2-30. The experimental curve is plotted using the data point at $600 \mu\text{W}$ optical power. The experimental curve is generated using Eq. (2.2) by assuming the saturated photoconductivity to be $8.8 \times 10^{-4} \text{ S/m}$.

2.10 Reference

- [1] D. M. Pai and B. E. Springett, "Physics Of Electrophotography," *Reviews Of Modern Physics*, vol. 65, pp. 163-211, 1993.
- [2] R. C. Hayward, D. A. Saville, and I. A. Aksay, "Electrophoretic assembly of colloidal crystals with optically tunable micropatterns," *Nature*, vol. 404, pp. 56-59, 2000.
- [3] M. Ozkan, S. Bhatia, and S. C. Esener, "Optical addressing of polymer beads in microdevices," *Sensors And Materials*, vol. 14, pp. 189-197, 2002.

- [4] S. Wang, *Fundamentals of semiconductor theory and device physics*. New Jersey: Prentice Hall, 1989.
- [5] R. Schwarz, F. Wang, and M. Reissner, "Fermi-Level Dependence Of The Ambipolar Diffusion Length In Amorphous-Silicon Thin-Film Transistors," *Applied Physics Letters*, vol. 63, pp. 1083-1085, 1993.
- [6] T. Tiedje, C. R. Wronski, B. Abeles, and J. M. Cebulka, "Electron-Transport In Hydrogenated Amorphous-Silicon - Drift Mobility And Junction Capacitance," *Solar Cells*, vol. 2, pp. 301-318, 1980.
- [7] M. J. Madou, *Fundamentals of microfabrication*. New York: CRC Press, 1997.
- [8] R. A. Street, *Hydrogenated Amorphous Silicon*. New York: Cambridge University Press, 1991.
- [9] J. H. Wei and S. C. Lee, "Electrical and optical properties of implanted amorphous silicon," *Journal Of Applied Physics*, vol. 76, pp. 1033-1040, 1993.
- [10] S. M. Sze, *Physics of Semiconductor Devices*, 2 ed. New York: John Wiley & Sons, Inc., 1981.
- [11] D. L. Staebler and C. R. Wronski, "Optically Induced Conductivity Changes In Discharge-Produced Hydrogenated Amorphous-Silicon," *Journal Of Applied Physics*, vol. 51, pp. 3262-3268, 1980.
- [12] V. Cech, "Modeling of the I-V characteristics in amorphous silicon n(+)-i-n(+) devices," *Journal Of Applied Physics*, vol. 88, pp. 5374-5380, 2000.

CHAPTER 3

Scanning OET for Microparticle Sorting

3.1. Introduction

The optically-patterned electric field generated on the OET surface can be configured to trap and transport single or multiple cells in parallel. Such a dynamic reconfigurable electric field can provide driving forces for sorting particles without the need for the pumps, channels, and valves used in most of the microfluidic sorters [1-4]. This completely eliminates the need for the fabrication and integration of complex microfluidic components, adding much flexibility for cell or particle manipulation. In this chapter, a novel particle sorting mechanism based on a dynamic electric field patterned by scanning OET will be described. The sorting mechanism is based on the force balance between the hydrodynamic viscous force and the dynamic light-induced dielectrophoretic force. Randomly distributed particles with different sizes are sorted out and positioned in deterministic positions relative to a line-shaped scanning laser beam.

3.2 Sorting Mechanism

Optoelectronic tweezers is a novel mechanism that enables optical patterns to induce highly non-uniform electric fields on a photoconductive thin film material. The particles near the non-uniform electric field experience a net force, resulting from the

interaction between the electric field and the induced electric dipole of the particles. As discussed in Chap. 2, DEP force is expressed as [5]

$$F_{dep} = 2\pi r^3 \varepsilon_m \operatorname{Re}[K^*(\omega)] \nabla(E^2) \quad (3.1)$$

where E is the electric field strength, r is the particle radius, ε_m is the permittivity of the surrounding medium, ω is the angular frequency of the applied electric field, and $K^*(\omega)$ is the Clausius-Mossotti (CM) factor, which has a value between 1 and -0.5, representing the polarizability of the particle. This force is very sensitive to the size of the particle (r^3) and the non-uniformity of the field (∇E^2). When a line-shaped laser beam scans across the OET surface, it produces an electric field pattern that moves at the same speed, as shown in Fig. 3.1. This light-induced electric field pushes particles forward in the OET device. The relative distance between the moving light beam and the particles is determined by the balance between the DEP force and the viscous force. Using Stoke's Law to estimate the viscous force for a moving particle, we obtain the following relationship between the particle size and non-uniformity of the field:

$$r^2 \nabla(E^2) = C = \frac{3\eta v}{\varepsilon_m \operatorname{Re}[k^*(\omega)]} \quad (3.2)$$

where r is the particle radius and C is a constant determined by the light scanning speed, v , the real part of the CM factor, and the viscosity, η , and permittivity, ε_m , of the surrounding medium. Since the term $\nabla(E^2)$ is a function of the relative distance between the particle and the electric field maximum, particles with different sizes will have different deterministic distances to the center of the scanning laser beam. Based on this principle, particles with different sizes will be sorted out when the laser beam scans across the OET surface as shown in Fig. 3-1(c).

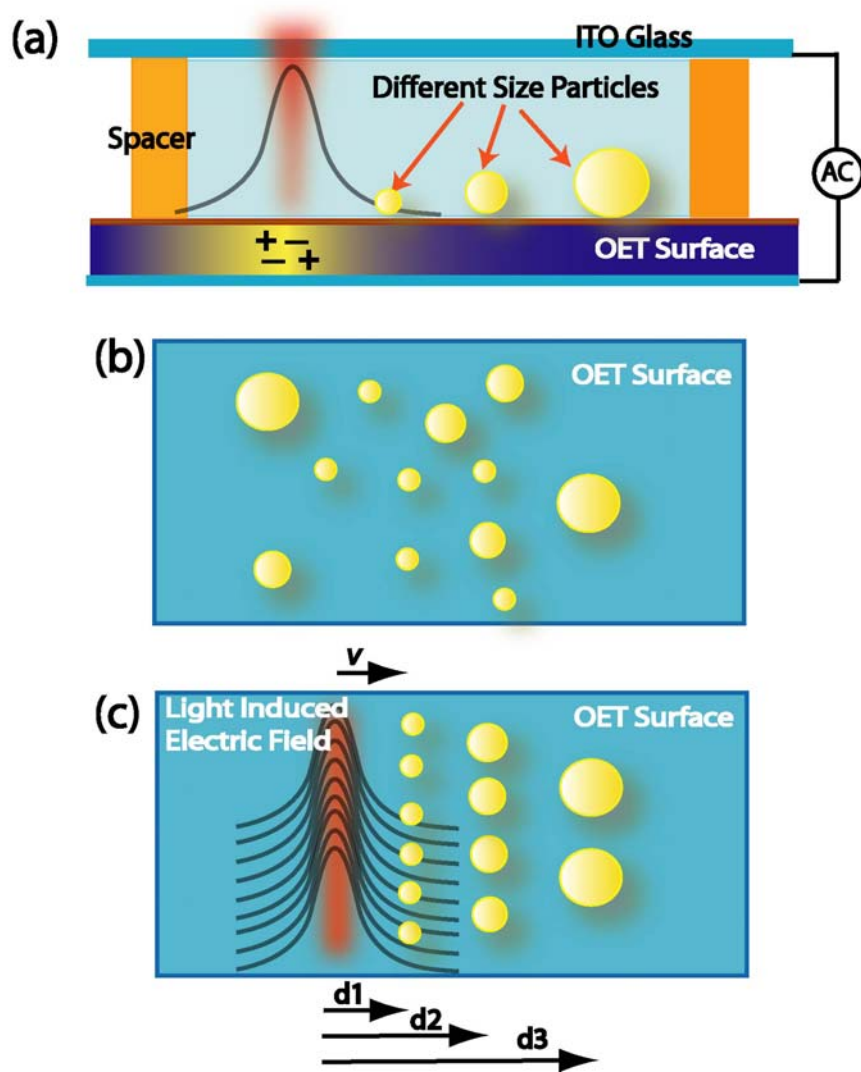


Fig. 3-1 (a) Schematic diagram of the OET device. The particles are sandwiched between a top ITO glass and a bottom OET surface. (b) Particles with different sizes are initially distributed at random positions. (c) Particles are sorted according to their sizes by a line-shaped scanning laser beam across the OET surface.

3.3 Experimental Setup and Results

The experimental setup is shown in Fig. 3-2. A single-mode fiber-pigtailed laser diode with a wavelength of 635 nm is coupled through a fiber collimator, producing a beam spot size of 3 mm at an optical power of 120 μW . A cylindrical lens and a 10 \times objective lens are used to transform the circular gaussian beam into a line-shaped pattern and focus it onto the OET surface. A scanning mirror is programmed to steer the laser beam. A scanning mirror is programmed to steer the laser beam.

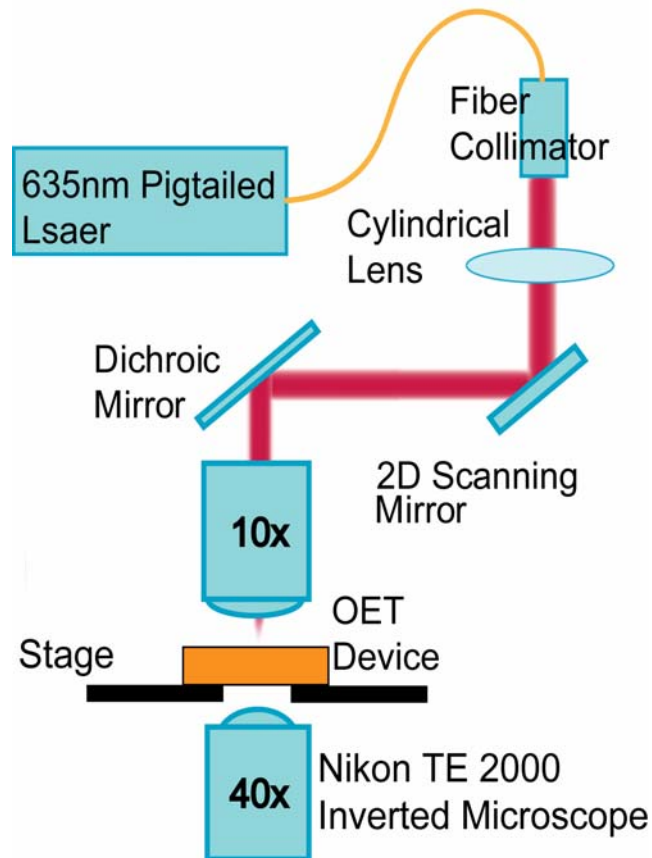


Fig. 3-2 Experimental setup for optical sorting of microscopic particles.

Figure 3-3 shows the result when the laser beam scans across the OET surface where the 10- and 20- μm -diameter polystyrene beads are randomly distributed. After the line-shaped laser beam scans across the assortment of beads, the 10- and 20- μm beads become aligned at different distances relative to the center of the beam. The laser beam is programmed to “jump” between these two groups of particles and further separate them. This sorting process finished in 25 seconds. Figure 3-4 shows the sorting of 5 μm , 10 μm , and 20 μm particles with relative distances of 15 μm , 20 μm , and 40 μm , respectively, from the laser line under a scan speed of 6 $\mu\text{m}/\text{s}$.

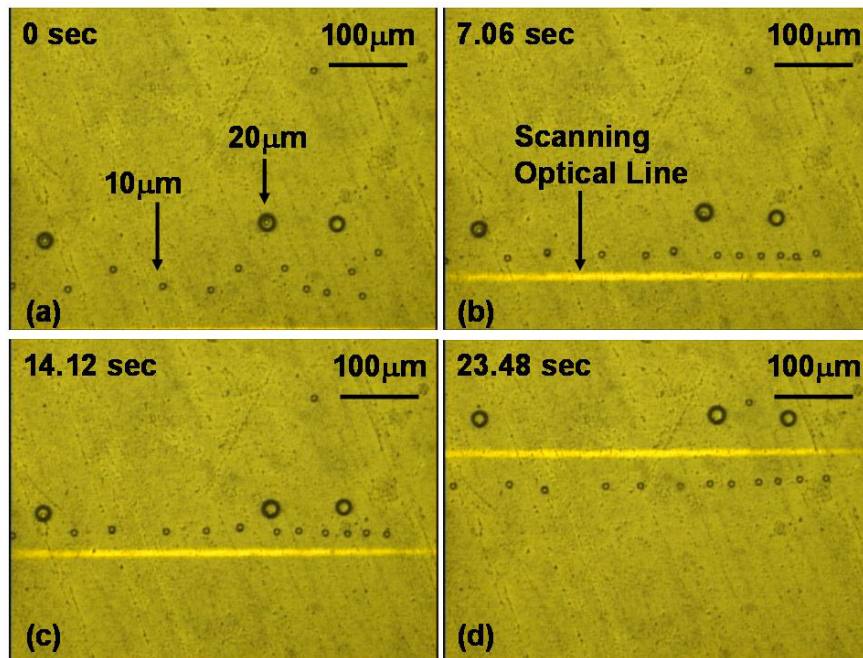


Fig.3-3 Example of OET based optical sorting of 10- and 20- μm polystyrene particles using a 120- μW red diode laser (wavelength = 635nm). (a) The particles are randomly distributed on the surface. (b) The optical beam scans across the 10 μm beads area and align them into a line pattern. (c) Both the 10 μm and 20 μm beads are aligned and moving with different relative distances to the center of the optical beam (d) The optical

beam is programmed to “jump” into the spacing between these two groups of particles and further separate them.

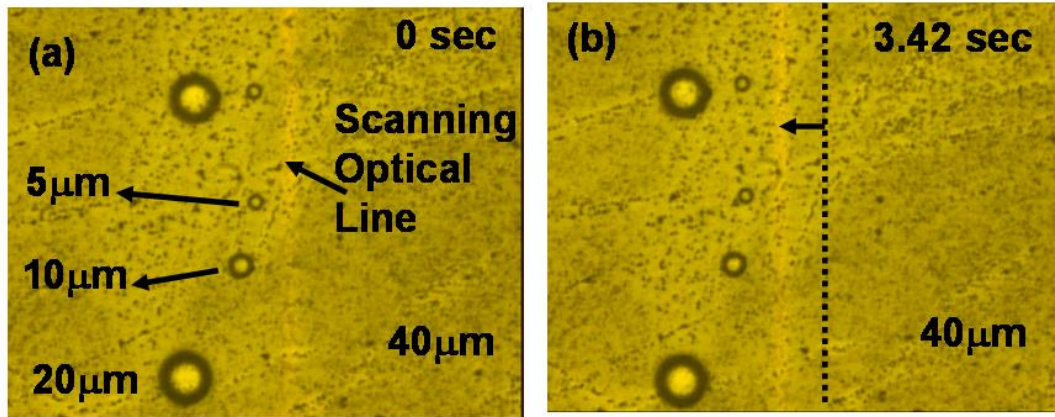


Fig. 3-4 Sorting of three different sizes of particles. The optical beam scans at a constant rate from the left to the right. These three sizes of particles are moving at the same speed as the light beam. Their deterministic relative distances remain constant during the movement.

The relative distance of a particle from the scanning line is dependent on the scanning speed. At a high scanning speed, the particle experiences a larger viscous force and balances this force by moving closer to the scanning beam, where a stronger electric field gradient exists. Fig. 3-5 shows the simulated and experimental results of the relative distances under different scanning speeds. For the 20- μm particle, the relative distance to the scanning beam center decreases from 50 μm to 25 μm when the scan speed increases from 20 $\mu\text{m/s}$ to 100 $\mu\text{m/s}$. This trend is also reflected in the data for 5- and 10- μm particles. Thus, low scanning rates provide a larger spatial separation between the different sizes of particles. At a scanning speed of 17 $\mu\text{m/s}$, the spacing between 5- and 10- μm particles is 7 μm , and the spacing between 10- and 20- μm particles is 28 μm . The

maximum scanning rate for a 5 μm particle is around 70 $\mu\text{m}/\text{s}$. If the scanning rate is increased beyond this limit, the particle becomes levitated by the vertical non-uniformity of the electric field, causing the particle to escape the lateral “pushing force” of the scanning beam. The escape speed is higher for bigger particles; for a 10- μm bead, it is 90 $\mu\text{m}/\text{s}$.

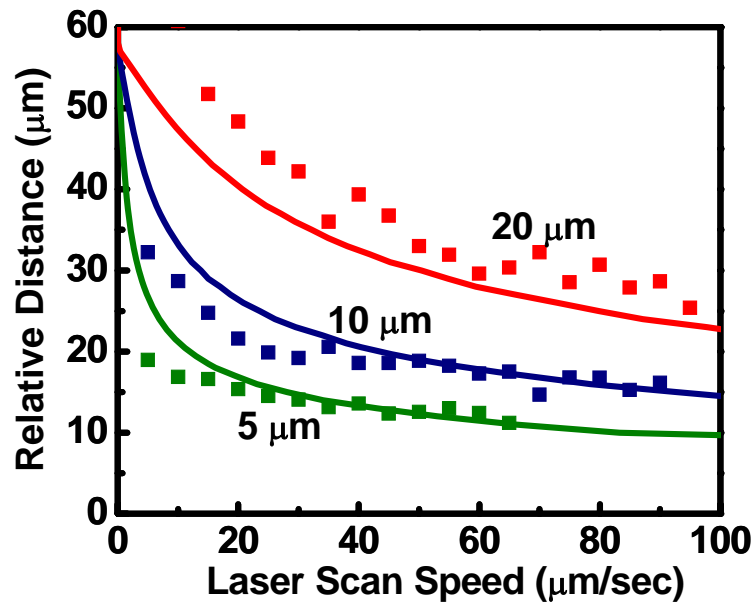


Fig. 3-5 Theoretical calculations (solid lines) and experimental data (dots) of the relative distances of microparticles from the scanning beam center as a function of scanning speed.

3.4 Reference

[1] M. P. MacDonald, G. C. Spalding, and K. Dholakia, "Microfluidic sorting in an optical lattice," *Nature*, vol. 426, pp. 421-424, 2003.

- [2] P. T. Korda, M. B. Taylor, and D. G. Grier, "Kinetically locked-in colloidal transport in an array of optical tweezers," *Physical Review Letters*, vol. 89, 2002.
- [3] X. B. Wang, J. Yang, Y. Huang, J. Vykoukal, F. F. Becker, and P. R. C. Gascoyne, "Cell separation by dielectrophoretic field-flow-fractionation," *Analytical Chemistry*, vol. 72, pp. 832-839, 2000.
- [4] P. R. C. Gascoyne, X. B. Wang, Y. Huang, and F. F. Becker, "Dielectrophoretic separation of cancer cells from blood," *Ieee Transactions On Industry Applications*, vol. 33, pp. 670-678, 1997.
- [5] T. B. Jones, *Electromechanics of particles*. New York: Cambridge University Press, 1995.

CHAPTER 4

Optical Image Driven OET for Massively Parallel Manipulation

4.1. Introduction

The experimental results in previous chapters have demonstrated OET's potential in optical manipulation with extremely low optical power. To activate the virtual electrode on the amorphous silicon surface, the minimum required light intensity is $10 \text{ nW}/\mu\text{m}^2$, which is 5 orders of magnitude less than optical tweezers. This property opens up the new possibility for optical manipulation using direct optical images from incoherent light sources such as LEDs or halogen lamps. Furthermore, tightly-focused light is not necessary in OET manipulation. This increases OET's effective manipulation area and enables massively parallel manipulation of single particles or cells – a function that is difficult to achieve by other techniques.

To generate a large array of optical beams on the OET surface for parallel manipulation, we integrate OET with a spatial light modulator (SLM) such as a digital micromirror device (DMD) or a liquid-crystal modulator. These spatial light modulators enable the generation of arbitrary dynamic optical patterns for projection onto the OET device. The number of the individually-controllable optical pixels on the OET surface is determined by the number of the elements of the spatial light modulator. The resolution of the projected images is determined by the pixel size on the spatial light modulator and

demagnification of the optics used to focus the optical images upon the OET surface. Current commercially-available DMD displays have more than a million pixels. Integrating such a spatial light modulator with OET turns a plain silicon-coated glass slide into a million-pixel optical manipulator. This gives OET users great flexibility in designing various moving electric field patterns for a wide variety of manipulation functions.

4.2 System of direct optical image driven OET using a LED

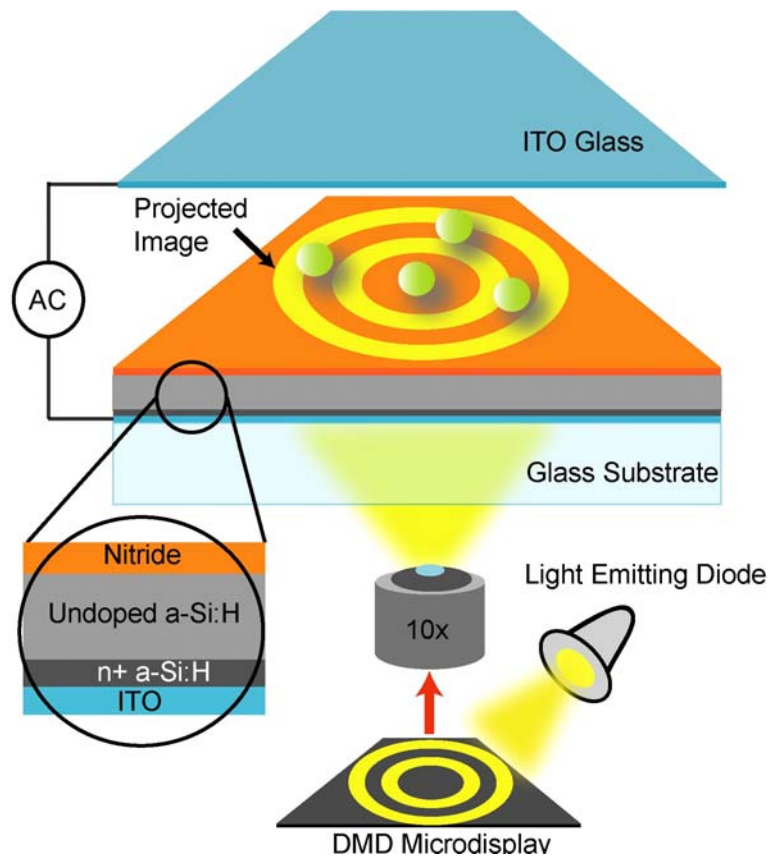


Fig. 4-1 Illustration of the direct optical image-driven OET. A spatial light modulator is used to program the projected images to create dynamic electric field to generate reconfigurable DEP forces for particle manipulation.

Figure 4-1 shows an OET system integrated with a 1024×768 pixel DMD SLM. The pixel size of this DMD chip is $13.68 \times 13.68 \mu\text{m}^2$. After projection onto the OET surface by a $10\times$ objective lens, the optical pixel size is $1.52 \mu\text{m}$. A single red light emitting diode (LED, 625 nm) is used as the illumination source. The light intensity measured on the OET plane is 1 mW. Covering $\sim 40,000$ pixels, the average optical power per pixel is 25 nW. The total effective manipulation area is $1.3 \text{ mm} \times 1.0 \text{ mm}$ on the OET plane, limited by the projected area of the entire DMD display.

4.3 Virtual Particle Concentrator and Conveyer

With the spatial light modulator, arbitrary patterns can be easily generated and reconfigured to perform specific functions as shown in Figs. 4-2, 4-3, and 4-4. In Fig. 4-2, an optical pattern consisting of concentric optical rings is projected onto the OET surface. By shrinking these rings synchronously, particles that experience negative DEP forces are concentrated in the center. One interesting phenomenon was observed in the concentration process. These particles are polarized in the vertical direction. The induced electrostatic dipoles on these particles are along the same direction, resulting in repulsive forces between the particles. As a result, the collected particles form symmetric patterns such as a triangle, a pentagon, and a hexagon, depending on the number of the particles collected. An optical conveyer that transports multiple particles in parallel from the left to the right of the manipulation area is demonstrated in Fig. 4-3. The particles are

transported in the conveyer in a speed of $20\mu\text{m}/\text{sec}$, which can be controlled by changing the refreshing rate of the projected images.

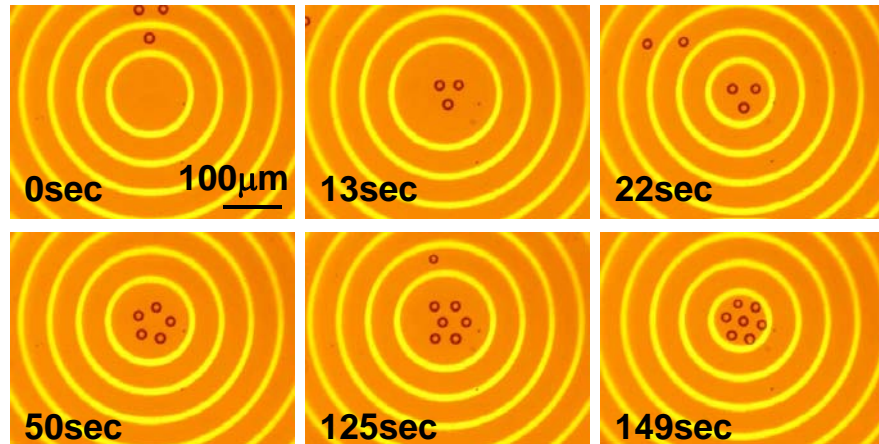


Fig. 4-2 Particles are collected by the shrinking optical rings to the concentric center. The electrostatic dipoles of the particles repel each other and the particles eventually form self-assembled patterns, such as triangle, pentagon, and hexagon.

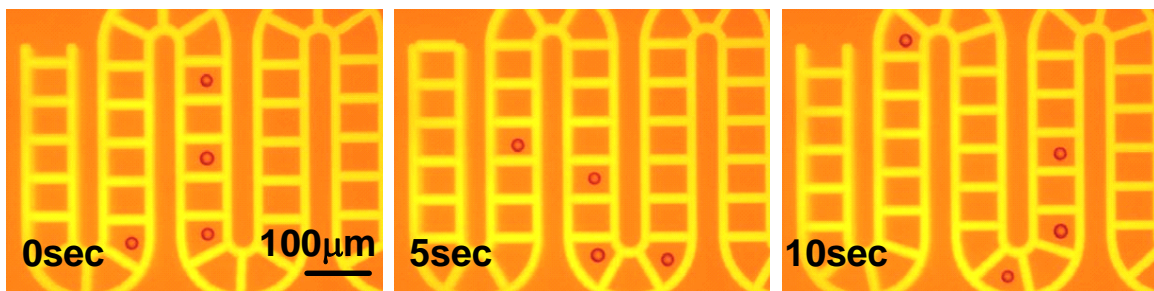


Fig. 4-2 A dynamic optical conveyer that transports multiple particles. The $20\text{-}\mu\text{m}$ polystyrene particles are transport in a speed of $20\ \mu\text{m}/\text{sec}$.

4.4 Selective concentration of live white blood cells

By exploiting the dielectric differences between different particles or cells, DEP techniques have been able to discriminate and sort biological cells with differences in membrane properties (permeability, capacitance, and conductivity), internal conductivity, and cell sizes [1-3]. The OET technique not only inherits these DEP advantages, but also provides the capability of addressing each individual cell. We demonstrate the selective concentration of live human B cells from a mixture of live and dead cells in Fig. 4-4. The cells are suspended in an isotonic buffer medium of 8.5% sucrose and 0.3% dextrose, mixed with a solution of 0.4% Trypan blue dye to check the cell viability, resulting in a conductivity of 10 mS/m. The applied ac signal is 14 Vpp at a frequency of 120 kHz. The cell membranes of live cells are selectively permeable, and can maintain an ion concentration differential between the intracellular and extracellular environments. Dead cells cannot maintain this differential. When dead cells are suspended in a medium with a low ion concentration, the ions inside the cell membrane is diluted through ion diffusion. This results in a difference between the dielectric properties of live and dead cells. Using a similar shrinking optical rings but with a dashed line pattern, live cells can be selectively concentrated. Live cells experience positive OET, and are collected in the center of the shrinking optical ring pattern by attraction to the illuminated region, while dead cells experience negative OET and are not collected.

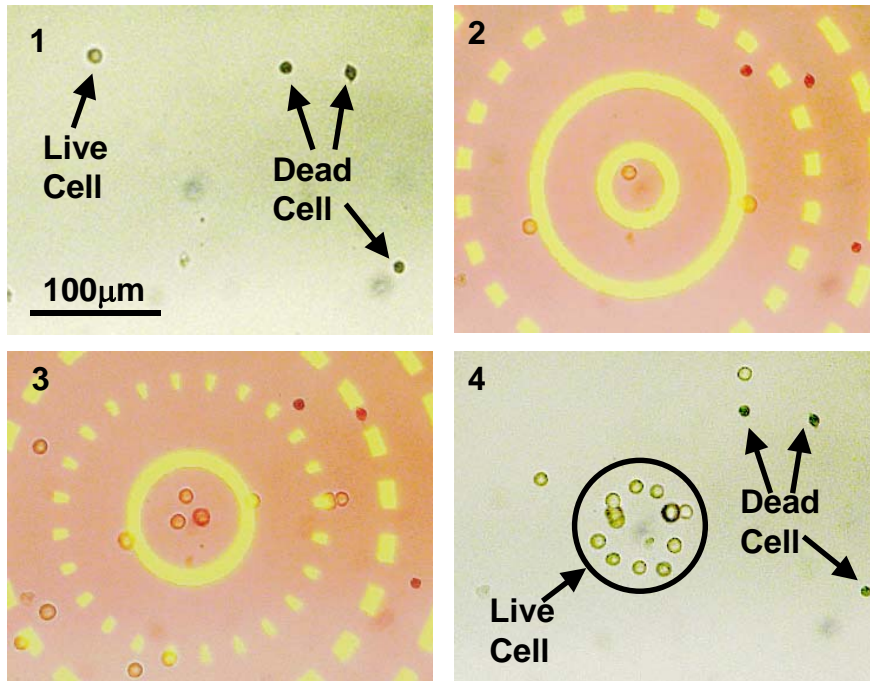


Fig. 4-4 Selective collection of live cells from a mixture of live and dead cells. The live cells experience positive OET, trapping them in the bright areas, and pulling the live cells into the pattern's center. The dead cells (stained with Trypan blue dye) leak out through the dark gaps and are not collected.

4.5 Massively Parallel Optical Manipulation of Microscopic Particles

To demonstrate the high-resolution capabilities of OET, we have created 15,000 DEP traps across an area of $1.3 \times 1.0 \text{ mm}^2$ as shown in Fig. 4-5(a). The particles are trapped in the dark area by the induced negative DEP forces, which push the beads into the non-illuminated regions, where the electric field is weaker. The size of each trap is optimized to capture a single 4.5- μm diameter polystyrene bead. The pitch between

particles is 12 μm , corresponding to 8 optical pixels. By programming the projected images, these trapped particles can be individually moved in parallel. Shown in Fig. 4-5b are the snapshots of the captured video showing the particles in adjacent columns are transport in opposite directions.

Although OET has the capability to pattern high-resolution virtual electrodes, the trapping of submicron particles using DEP force is still challenging for current OET devices since it requires a strong electric field gradient to overcome the Brownian motion of the particles. In our current optoelectronic tweezers, the electric field gradient patterned by the LED is not strong enough to trap particles less than 1 μm through DEP mechanism. However, the trapping of particles less than 1 μm does occur when the OET device is operated at a low frequency ac bias (~ 1 kHz). This trapping mechanism is not due to DEP forces, but is caused by the optically-patterned ac electroosmotic flow. Details of this mechanism will be discussed in Chapter 6.

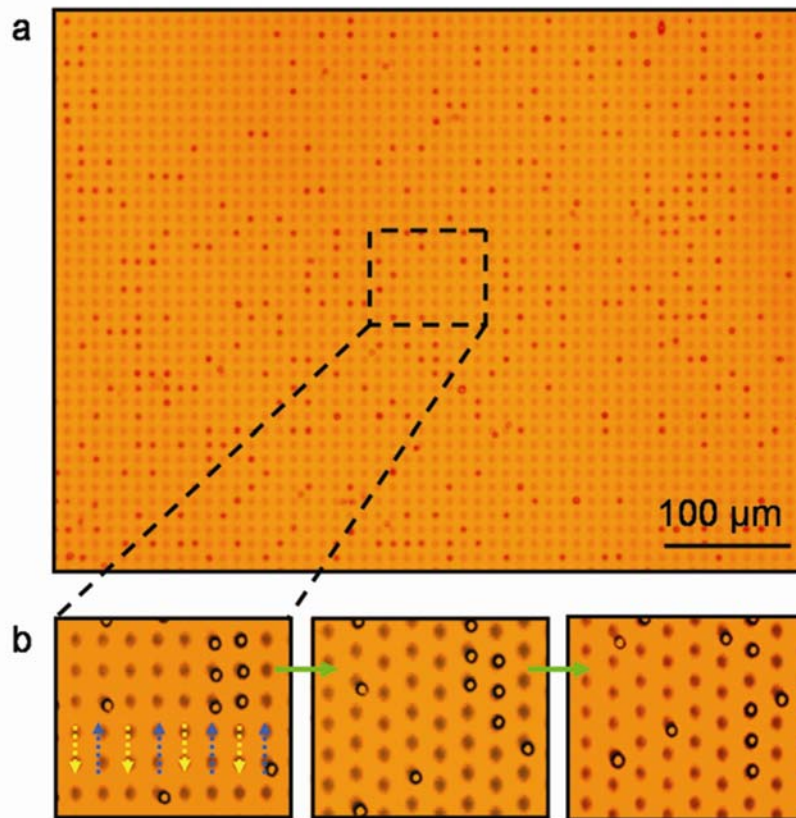


Fig. 4-5 Massively parallel manipulation of single particles. (a) 15,000 particle traps are created across a $1.3 \text{ mm} \times 1.0 \text{ mm}$ area. The $4.5 \text{ }\mu\text{m}$ -diameter polystyrene beads experiencing negative DEP forces are trapped in the dark area. Each trap has a diameter of $4.5 \text{ }\mu\text{m}$, which is adjusted to fit a single particle. (b) Parallel transportation of single particles. Three snapshots from the captured video show the particle motion in a subset of the manipulation area. The trapped particles in two adjacent columns move in opposite directions, as indicated by the blue and yellow arrows.

4.6 Integrated Dynamic Optical Patterns for Multi-step Manipulation

Using direct imaging, sophisticated virtual electrodes can be easily patterned and reconfigured to create dynamic electric fields for continuous particle manipulation without the assistance of fluidic flow. Various optical components can be synchronized and integrated to form a complicated virtual machine for performing multi-step functions. Fig. 4-6 shows an example of an integrated optical manipulator that combines multiple functions of optical conveyors, sorters, wedges, and joints. Particles are transported through different functional areas and recycled in this light-patterned circuit, traveling through different paths depending on the position of the wedge divider. Particles with different sizes are fractionated in the vertical z direction as they pass through the sorter path due to the asymmetric shape of the light-patterned electric fields. The sorting mechanism is similar to the scanning OET sorting principle that has been discussed in Chap 3. In Chap 3, we demonstrate one-dimensional sorting using a scanning line-pattern laser beam, and here, we show an example of two-dimensional sorting. Particles with different sizes are fractionated in the direction parallel to the direction of movement of the optical patterns.

After the sorter path, an optical wedge divides and guides the particles into the two conveyors. The looped optical conveyors can recycle the particles back to the sorter input to repeat the process. Fig. 4-6(b) and (c) show that the paths of the fractionated particles can be switched by reconfiguring the tip position of the optical wedge. The trajectories of the particle movement are highly repeatable and accurately defined even though the dark area in the conveyor is much larger than the particles. The trace pattern

shown in Fig.4-6(b) is the overlap of the loops of the particles traces after 43 cycles through the optical pattern. Fig. 4-7 shows the distribution of the particle position in the middle of the sorter (marked by a white bar) after the particles have passed through the sorter 43 times. The standard variations of trace broadening are 0.5 μm for the 10- μm bead, and 0.15 μm for the 24- μm bead. As the magnitude of the DEP force is proportional to the particle volume, the larger particle shows a better confinement in the optically-patterned DEP cages during transportation. The data shown in Fig.4-7 also considered the long-term drifting of the average traces due to the metastability of a-Si:H.

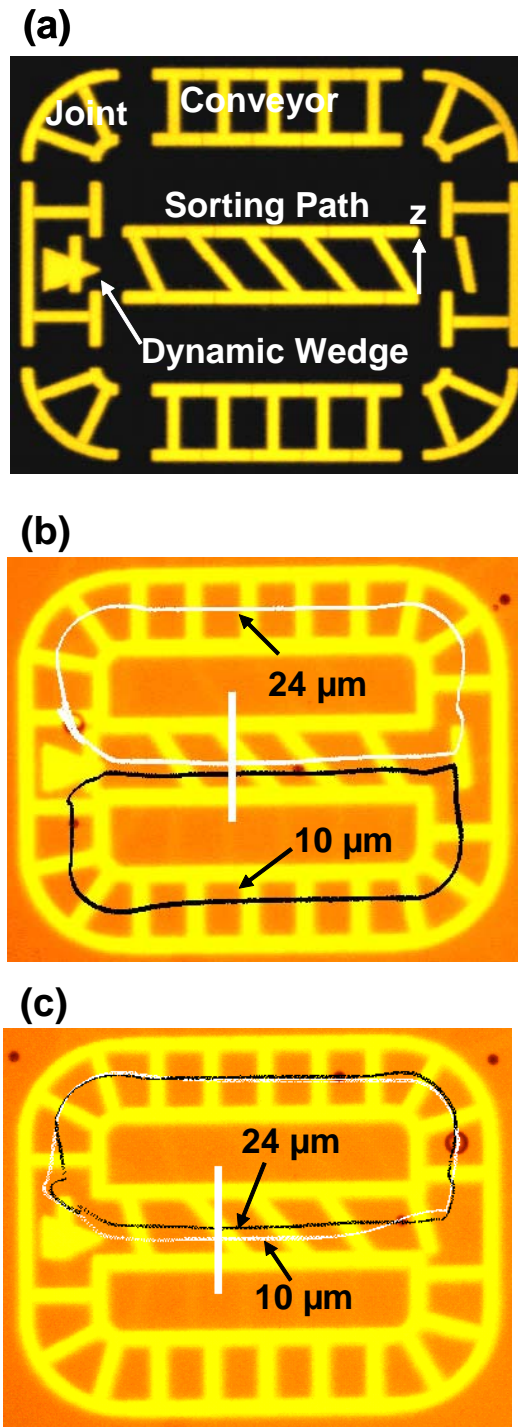


Fig.4-6 An example of an integrated virtual optical machine. (a) Integration of virtual components including an optical sorter path, conveyors, joints and a wedge. The motion of different components is synchronized. (b), (c) Two polystyrene particles with sizes of

10 μm and 24 μm pass through the sorter path and are fractionated in the z-direction due to the asymmetrical optical patterns. The particle trajectories can be switched at the end of the sorter path by the optical wedge.

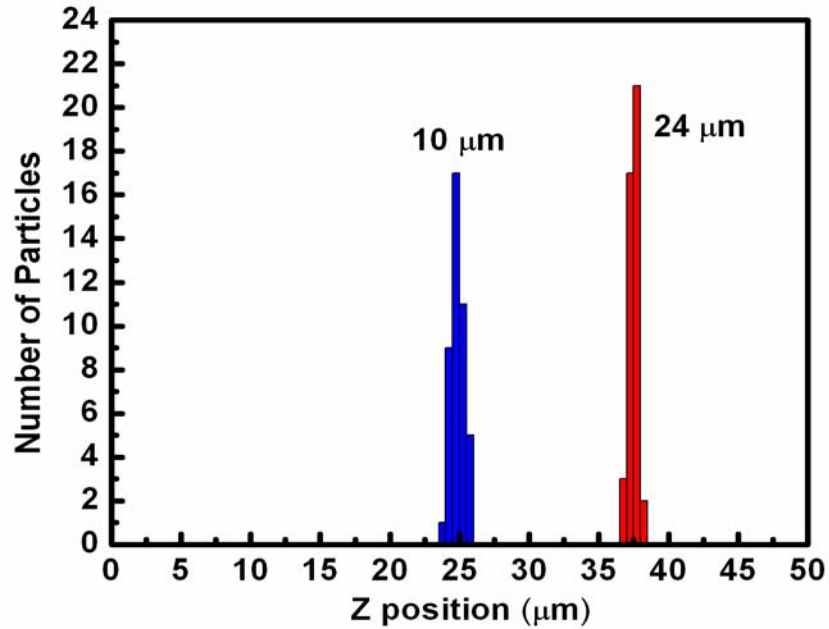


Fig.4-7 Optical sorting repeatability test. The white and black loops in 4-6(b) represent the particle traces after 43 cycles. The trace broadening at the white bar has a standard deviation of 0.5 μm for the 10- μm bead and 0.15 μm for the 24- μm bead.

4.7 Effect of Long-term photodegradation of Photoconductivity in Amorphous Silicon

As discussed in Chap 2, there is a long term metastability issue in amorphous silicon. The photoconductivity of the amorphous silicon decays as the illumination time increases, which is due to optically-induced defect states in the material [4, 5]. This leads

to a reduction in recombination time of the photo-generated electron-hole pairs, resulting and a decrease of the conductivity as illumination time increases. This decreases the electric field strength in the liquid layer and the DEP forces on particles. Fig. 4-8 shows the z positions of both the 10- μm and the 24- μm particles corresponding to the data shown in Fig. 4-7. A long-term drift of the average traces are observed on both the 10- μm and the 24- μm particles. The drift after the particles are recycled for 43 times for the 10- μm and 24- μm particles are 1 μm and 0.5 μm , respectively. The light-induced defect states can be healed by annealing the device at 150°C for 2 hours [5].

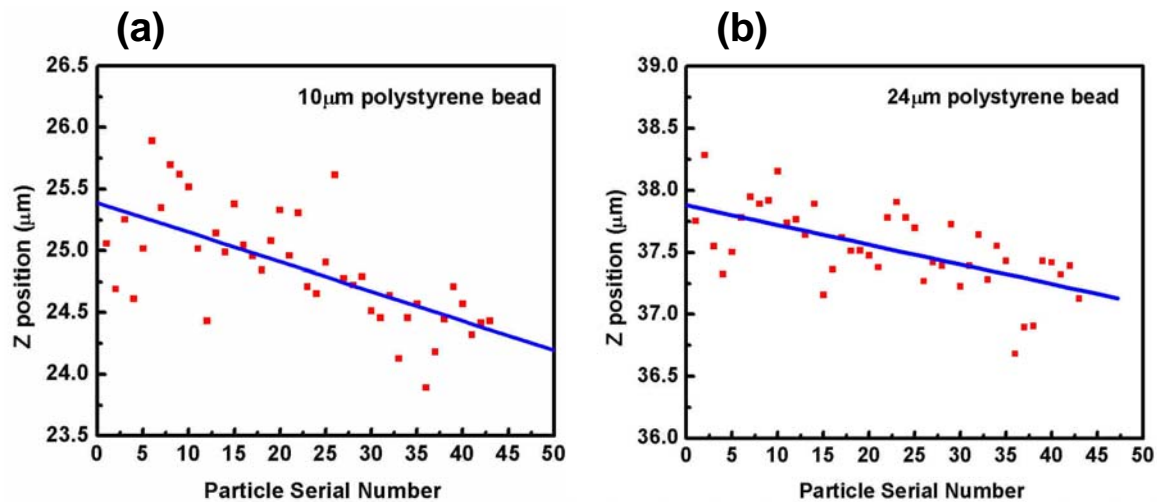


Fig.4-8 The particles experience a long-term drift as the illumination time increases. (a) The drift of the trajectory of the 10- μm particle is 1 μm after recycling for 43 times. (b) The drift of the 24- μm particles is 0.6 μm .

4.8 Reference

- [1] P. Gascoyne, R. Pethig, J. Satayavivad, F. F. Becker, and M. Ruchirawat, "Dielectrophoretic detection of changes in erythrocyte membranes following

- malarial infection," *Biochimica Et Biophysica Acta-Biomembranes*, vol. 1323, pp. 240-252, 1997.
- [2] J. Yang, Y. Huang, X. B. Wang, F. F. Becker, and P. R. C. Gascoyne, "Differential analysis of human leukocytes by dielectrophoretic field-flow-fractionation," *Biophysical Journal*, vol. 78, pp. 2680-2689, 2000.
- [3] F. F. Becker, X. B. Wang, Y. Huang, R. Pethig, J. Vykoukal, and P. R. C. Gascoyne, "Separation Of Human Breast-Cancer Cells From Blood By Differential Dielectric Affinity," *Proceedings Of The National Academy Of Sciences Of The United States Of America*, vol. 92, pp. 860-864, 1995.
- [4] V. Nadazdy and M. Zeman, "Origin of charged gap states in a-Si: H and their evolution during light soaking," *Physical Review B*, vol. 69, 2004.
- [5] D. L. Staebler and C. R. Wronski, "Optically Induced Conductivity Changes In Discharge-Produced Hydrogenated Amorphous-Silicon," *Journal Of Applied Physics*, vol. 51, pp. 3262-3268, 1980.

CHAPTER 5

Image Feedback-Controlled OET for Automatic Processing

5.1. Introduction

OET enables massively parallel manipulation of single cells, necessitating the use of an automated control system for particle manipulation. In this Chapter, we report a novel image feedback-controlled OET system that allows triggering of adaptive optical patterns on the OET device based on the visual information of the manipulated particles and cells. This OET system integrates image analysis techniques to distinguish different cells and particles based on visual characteristics such as fluorescent signal, size, or surface texture. The appropriate optical patterns are automatically created to process pre-assigned manipulation functions. Several automatic functions have been demonstrated, including the assembling of randomly distributed particles, real-time interactive control, and the continuous sorting of cells and particles based on size or color.

5.2 Microvision-Activated OET System

Figure 5-1 shows the schematic diagram of the microvision-activated optical manipulation system[1]. It is constructed on a Nikon inverted microscope. A 150-W halogen lamp illuminate a programmable DMD microdisplay. The DMD pattern is projected onto the OET device through a 10× objective. The halogen lamp can be

replaced by a single LED if the speed of the particle is not important. The halogen lamp provides more optical power than the LED, and can more fully turn on the virtual electrodes for DEP manipulation.

The microscopic image of the particles and cells in the OET device cavity is captured by a CCD camera through the inverted microscope. A Java-based software called Processing (<http://processing.org/>) is used to grab the digital video from the camera, and analyzes each video frame to acquire the particle information. The corresponding optical patterns to control particle motion can be automatically generated by Processing, using customized functions that we wrote in Java. Due to a hardware interface issue, the controlling software of the DMD kit does not support the real-time uploading and refreshing of the new optical images onto the DMD display. The projected images are first stored in an image format (.jpg) and are batch-loaded onto the DMD control board for display.

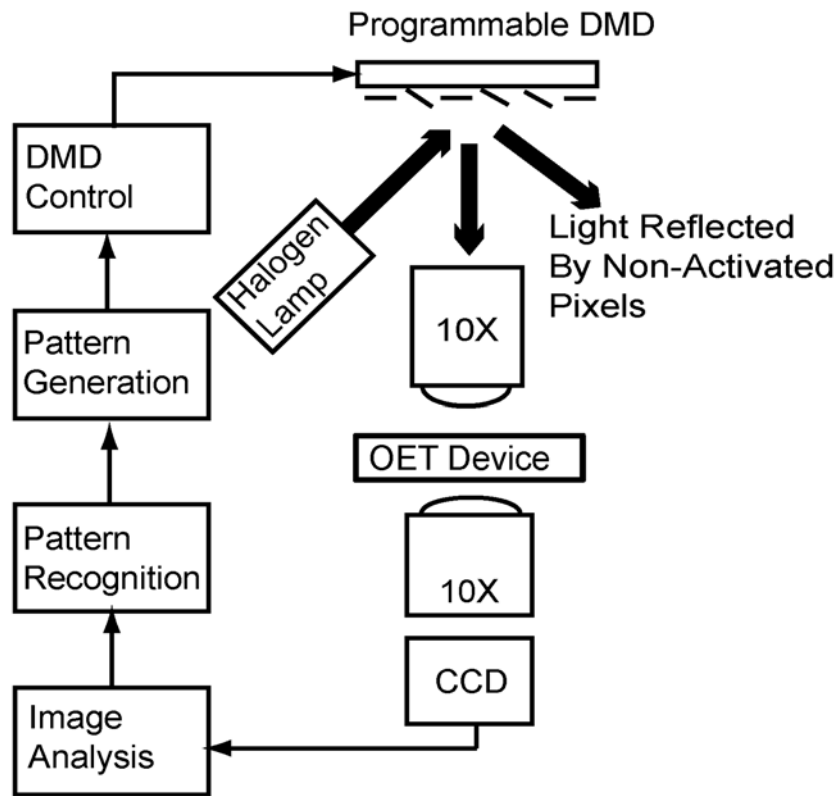


Fig. 5-1 Schematic diagram of the microvision-activated optical manipulation system.

5.3 Particle Recognition Process

Figure 5-2 shows the process of recognizing and arranging randomly distributed particles into a predetermined pattern. First, the images of the particles are captured and analyzed by the microvision system (Step 1), which then identifies the positions and the sizes of all particles (Step 2). The software then generates a ring pattern to trap the selected particles (Step 3). A series of optical images are then projected to transport selected particles in parallel to final positions (Step 4).

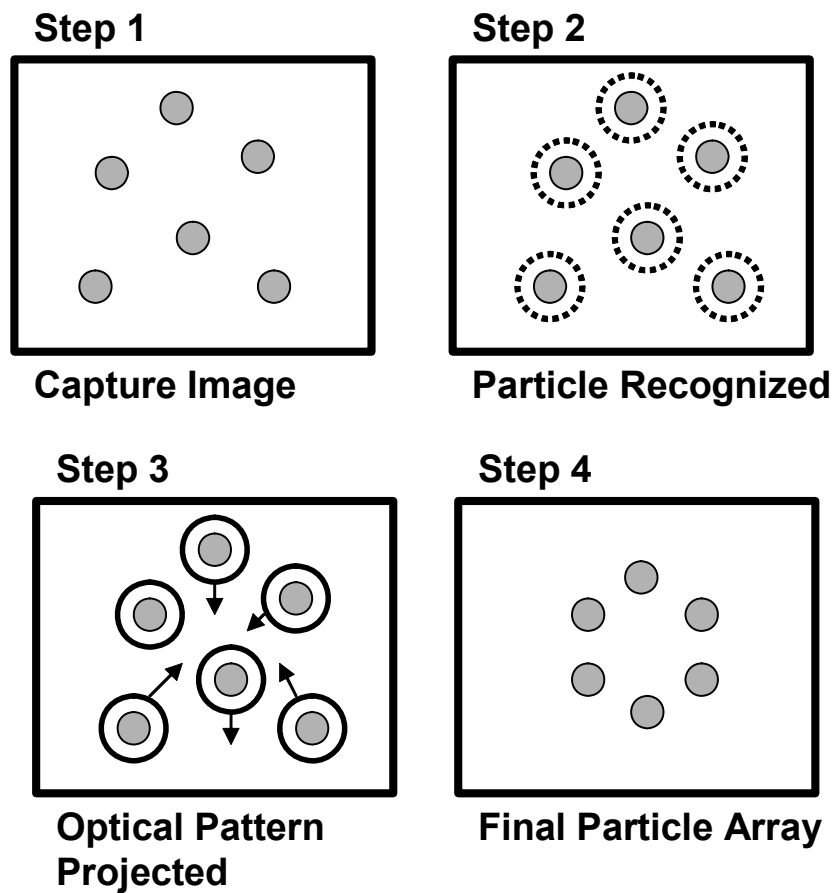


Fig. 5-2 Steps to arrange randomly distributed particles into a specific pattern.

Particle recognition is achieved by using a dark-pixel recognition algorithm to scan through each pixel of the captured image. The brightness value and the position of each pixel are recorded and calculated to determine the size and position of each particle. Figure 5-3(a) shows a test image for this automatic particle recognition system. This image shows randomly distributed particles with three different sizes, 10 μm , 15 μm , and 20 μm . The brightness value of the pixels at the particle edge is smaller than that of the particle center or the background. By setting a threshold brightness that is between the values of the background and the particle edge, we can recognize the edge of each

particle. By averaging the x and y positions of all the edge pixels of a particle, we can determine its position. Figure 5-3(b) shows the recognized particles encircled by white ring patterns generated by the microvision-analysis system. The same algorithm also determines the size of each particle by counting the number of the recognized dark pixels. Larger particles have more dark pixels than smaller ones. Figure 5-3(c) is the histogram of the number of particles and the number of the dark pixels for each particle in Fig. 5-3(a). By setting a threshold to the number of the dark pixels, represented as the dashed line in the histogram figure, this system can selectively pick up particles with specific sizes. For example, in Fig. 5-3(d), the 7 largest 20- μm beads are selected. This recognition algorithm is used specifically for spherical particles with different sizes. Other algorithms can also be developed to recognize particles with different colors, shapes, and textures.

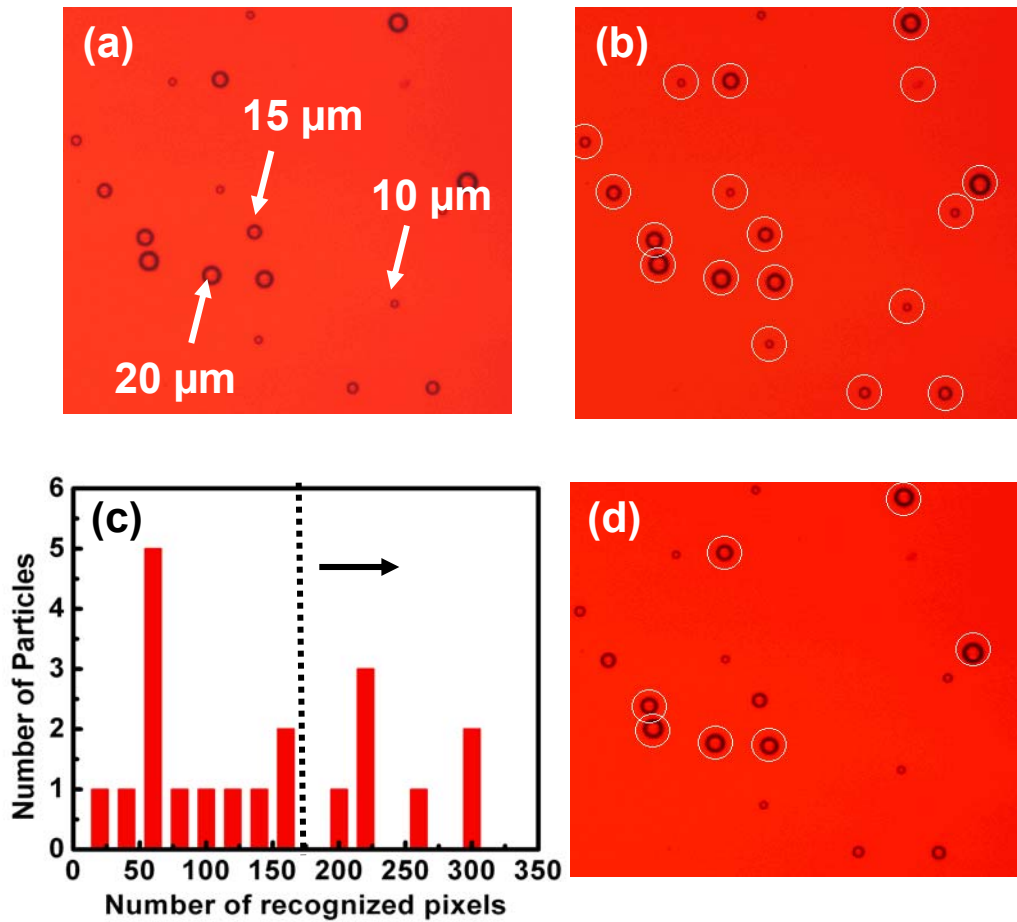


Fig. 5-3 (a) Test image for particle recognition. Polystyrene particles with three different sizes - 10 μm , 15 μm , and 20 μm , are mixed and randomly distributed. (b) The microvision system recognized the position of each particle and projected a ring marker around each particle. (c) A histogram of the number of particles and the number of the dark recognized pixels of the test image. (d) By setting a threshold number of the dark pixels, the largest particles are selected.

5.4 Automatic Generation of Optical Patterns for Functional Manipulation

In this experiment, the OET device is operated in the negative DEP mode, which repels the particles from strong electric field areas. To trap a single particle with negative DEP force, we create an optical ring pattern to form a virtual DEP cage that only allows a single particle to be trapped inside the ring (Fig. 5-4). In the static state, the trapped particle is focused at the center of the ring pattern, at the location of the minimum electric field. When the optical ring moves, the trapped particle also moves in the same direction, but its position deviates from the center of the ring, causing the DEP force to push the particle back to the center trap. The distance of deviation from the center of the ring is dependent on how fast the particle moves. If the optical ring moves too fast, the particle can escape the optical ring, as the DEP restoring force is not strong enough to hold the particle. The escape velocity of a 20- μm particle is 40 $\mu\text{m}/\text{s}$ in this system by using ring-pattern with line width of 20 μm and light intensity $\sim 100 \text{ nW}/\mu\text{m}^2$. To trap a particle with a smaller size, a smaller optical ring would be required, ensuring that only a single particle can reside in the ring.

Once the particle positions are recognized, the software generates the ring patterns and calculates the trajectories for all the particles to form a predetermined pattern. These optical patterns are stored as image files and are batch loaded to the DMD control software. This process is shown in Fig. 5-5(a). The image of the randomly distributed particles was scanned vertically from left to right. The first six particles were identified and trapped by the OET (0 sec). The trapped particles were transported by moving the ring traps, and reached the hexagonal configuration in 12 seconds. Figures 5-5(b) and 5-

5(c) show the video sequences of rearranging the particles into linear and triangular shapes. The unwanted particles were swept away by a scanning line pattern.

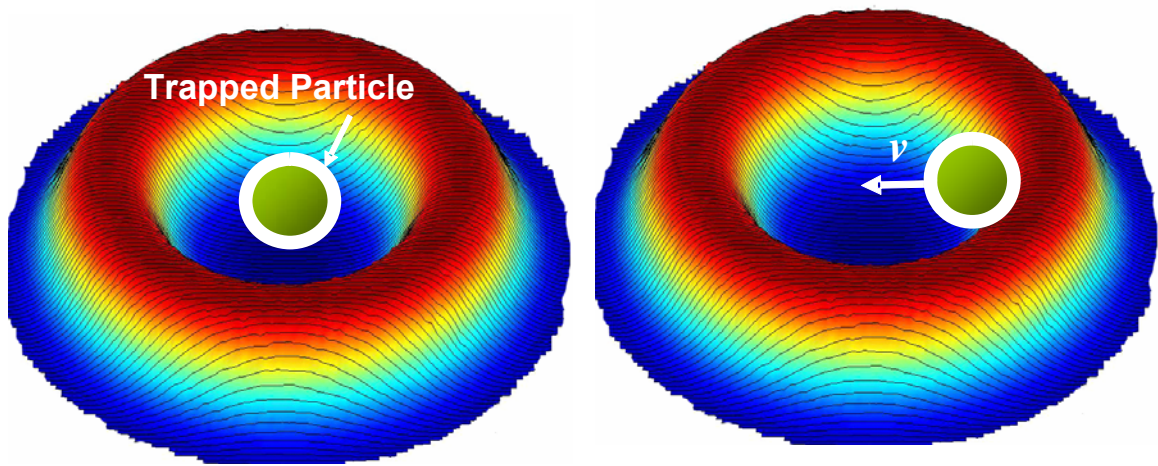
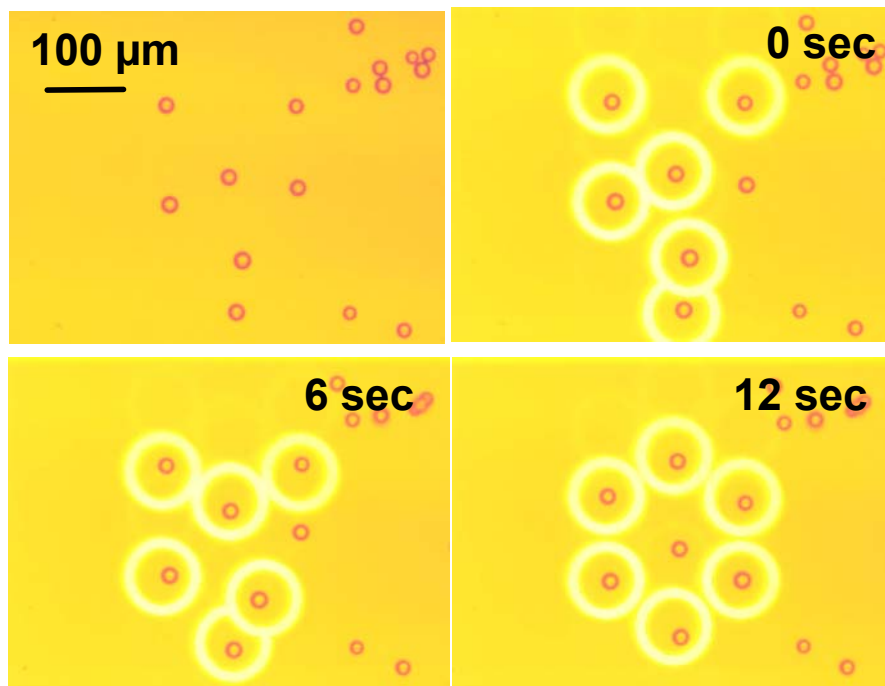
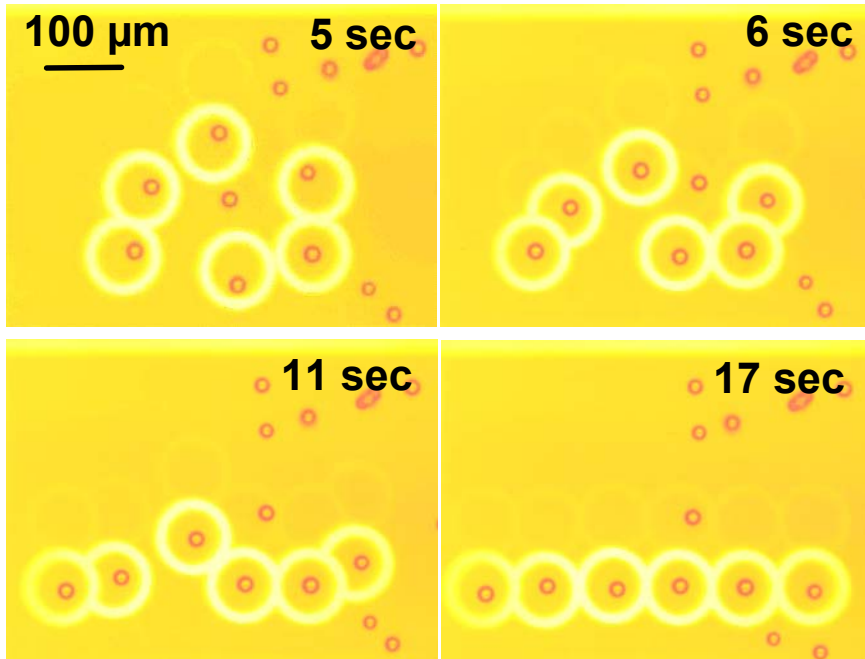


Fig. 5-4 (a) Illustration of the electric field distribution induced by a single optical ring pattern. In static state, the particle is trapped in the electric field minimum in the center. (b) During movement, the particle shifts away from the center to gain DEP force for transportation.

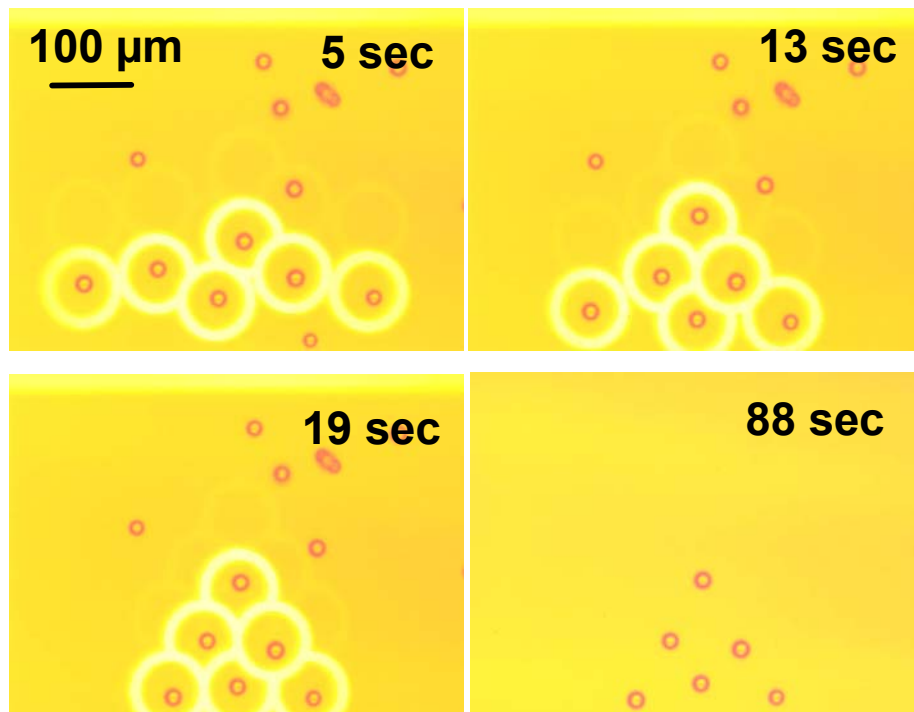
Fig. 5-5 Examples of microvision activated optical manipulation of microscopic particles



(a) Randomly distributed particles arranged into a hexagonal shape. The software recognizes the first six particles (vertically scanned from left to right) and generates optical patterns to cage and transport them to form a hexagonal pattern.



(b) The hexagonal pattern is transformed into a line.



(c) The line pattern is transformed into a triangular shape. The unwanted particles are swept away by a scanning line.

5.5 Continuous Sorting of Particles and Cells Based on Size and Color

In the previous section, we used a DMD to pattern the projected images on the OET device. Although the DMD provides sharp, high-resolution images, loading refreshed images to the DMD controller takes a few minutes, which is the rate-limiting step of our current system. Real-time control would require a DMD controller with much faster refresh rate.

In this section, we use a liquid crystal spatial light modulator (LC-SLM) to create the optical manipulation patterns. The control interface of the LC-SLM allows for the real-time refreshing of optical images at a rate of 5 frames per second. With this capability, we are able to achieve a continuous automatic optical sorting of cells and particles based on size and color [2].

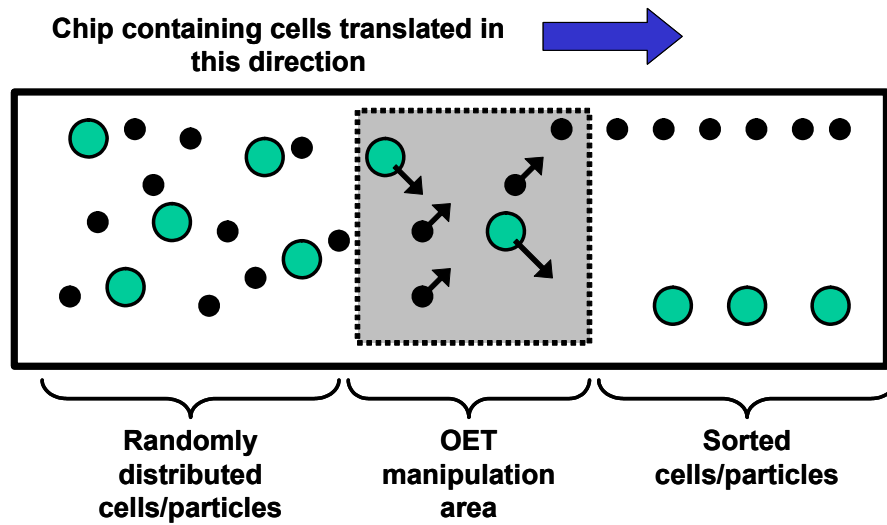
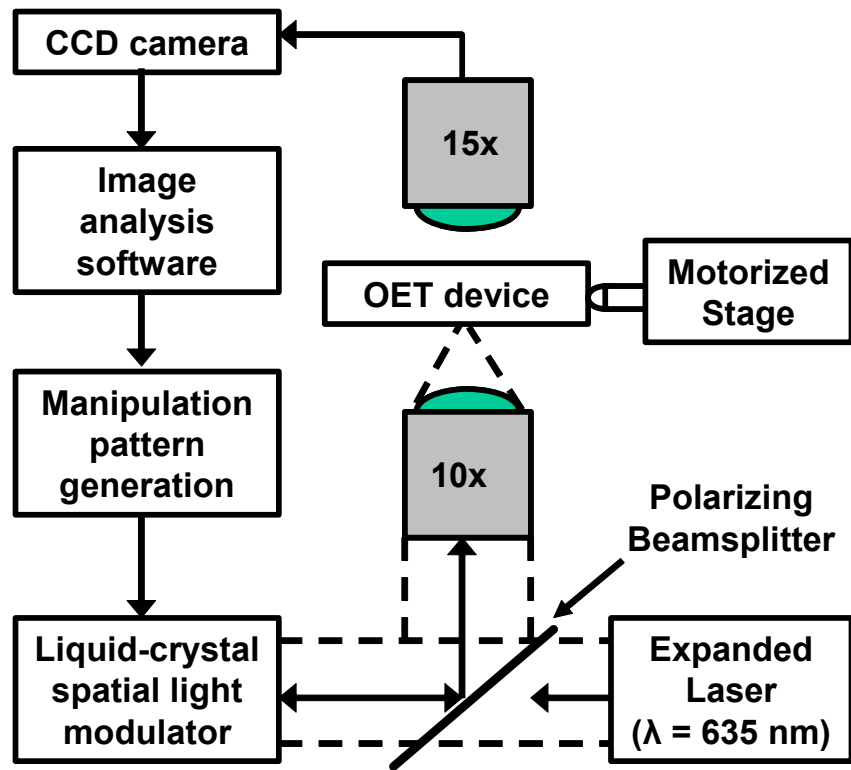


Fig.5-6 The OET system for the continuous sorting of cells and particles based on their visual characteristics such as size and color. The OET chip is positioned on a motorized stage, allowing the manipulation pattern to be rastered across the entire OET chip.

The LC-SLM used in this demonstration is PAL-SLM from Hamamatsu Inc. It has an array of 640×480 pixels covering a 20×20mm² area, and each pixel has an area of 40×40 μm². The operation wavelength is 635 nm. Since the LC-SLM is a phase modulator, a linear polarizing beam splitter is used to convert it to amplitude modulation. As shown in Fig. 5-6, a 10-mW, 635-nm laser beam is expanded five times to cover an area of 0.8-mm diameter spot on the image-generating surface. The patterned light is focused onto the OET device through a 10× objective lens. The microscopic image is captured by a CCD camera and analyzed by an image processing software (Processing 1.0). Based on the size, color, texture, or shape information, a corresponding optical pattern is generated on LC-SLM, producing an actuation electrode on the OET device. The effective manipulation area is approximately 250×250 μm² for this setup, limited by the expanded laser beam size at the focal plane of the objective lens. The OET chip is positioned on a programmable X-Y stage, allowing the manipulation pattern to be rastered over the entire OET chip (Fig. 5-6). This feedback system is real-time and fully automatic.

To generate optical patterns for particle sorting, the captured microscopic image is divided into 4800 scan-pixels. Each pixel scans its neighboring areas to search for particles. If a particle is found by one scan-pixel, this pixel can either be turned on to prevent the particle from moving toward this pixel (for OET in the negative DEP mode), or stay in the off state so it does not block the particle moving towards it. The size of the particles is much larger than that of a scan-pixel. Therefore, several scan-pixels can simultaneously locate the same particle in their scanning range, and generate multiple actuation pixels. An example illustrating this process is shown in Fig. 5-7. Particles of

different sizes enter the OET manipulation zone from the bottom. The goal of the sorting is to collect the large particles on the left side of the screen, and the small particles on the right side. In the vicinity of the large particle, we see that a scan-pixel has located the particle on right edge of the pixel. The scan-pixel has turned on to push the particle towards the left. The scan-pixels to left of the particle have also detected the particle, but stay in the off state to allow the particle to move to the left. For small particles, the criteria of the scan-pixels reverse, pushing the small particles to the right. Several pixels can turn on together to induce DEP forces on a single particle.

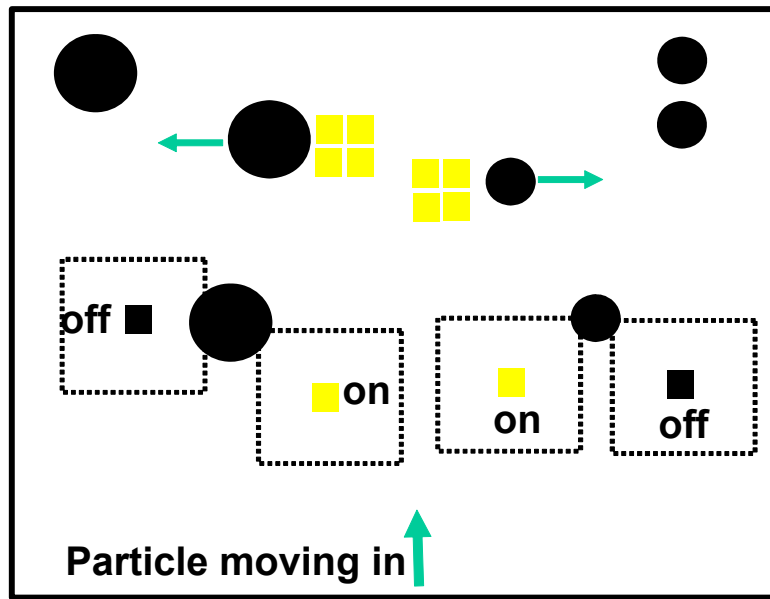


Fig.5-7 The illustration of the algorithm applied to generate optical patterns for particle sorting. The microscopic image is divided into 4800 scan-pixels. Each pixel scans its neighboring area searching for particles. Once a particle is found, the pixel can be turned on or off depending on its relative position to the detected particle and the programmed criteria for particle.

Figure 5-8 shows the test image and the generated optical pattern for projection onto the OET surface. In Fig. 5-8(a), there are 7 particles. The scan-pixels detect the presence of the particles, and the scan pixels on the left side of particles (marked by black dots on the test image) turn on the corresponding pixels of the spatial light modulator, creating a projected pattern as shown in Fig. 5-8(b). When the optical pattern is projected onto the OET surface, the bright pixels will map to the marked pixels on the test image.

The number of the scan-pixels can be increased to control smaller particles. Using a 15 \times objective lens, a 4800-pixel resolution works well for particles with diameters larger than 5 μm . To manipulate particles smaller than 5 μm , an objective lens with a higher magnification can be used, but the effective manipulation area is reduced.

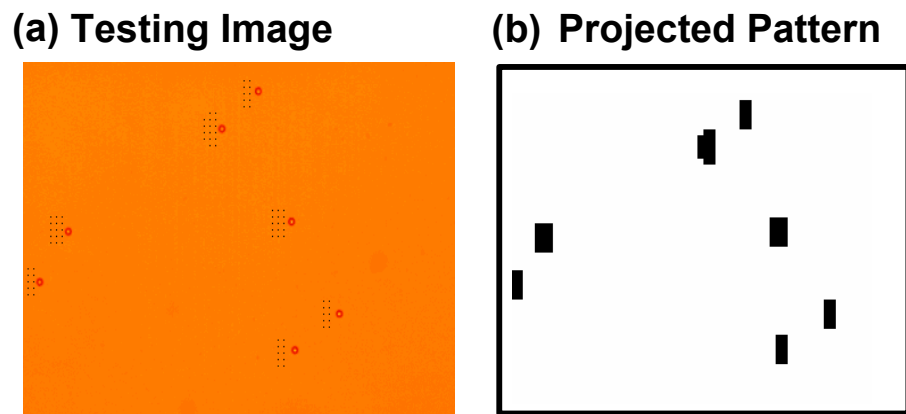


Fig. 5-8 Testing of the optical pattern generation algorithm for continuous particle sorting.

Figure 5-9 demonstrates a particle sorting function based on size. The OET chip is programmed to move the particles as they enter from the left side of the manipulation zone. The larger particles (20 μm) are pushed to the bottom of the image, while the smaller particles (15 μm) are pushed to the top of the image by the light-induced negative

DEP forces. The trajectories of the particles are recorded and plotted in Fig. 5-9(c). The particles enter the manipulation zone at random positions in the y direction. After they passed through the 250- μm -wide manipulation zone, the 20- and 15- μm particles are clearly separated.

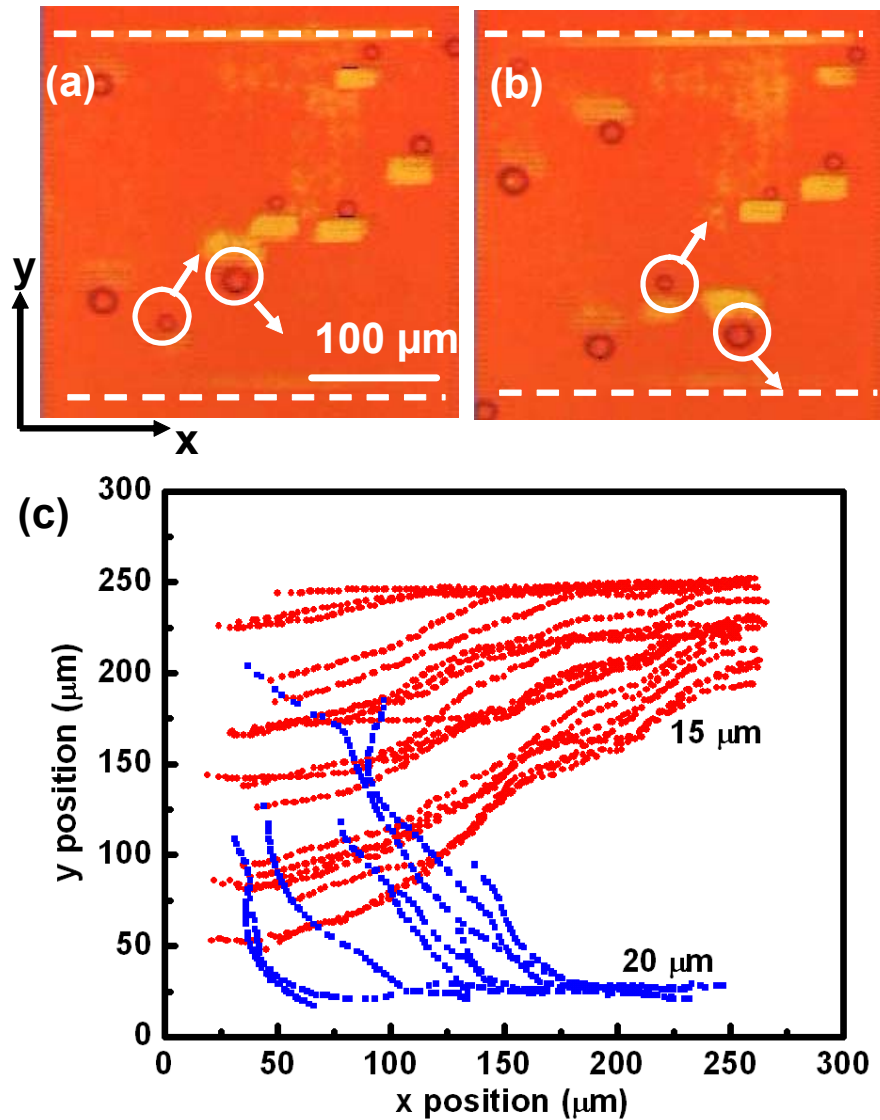
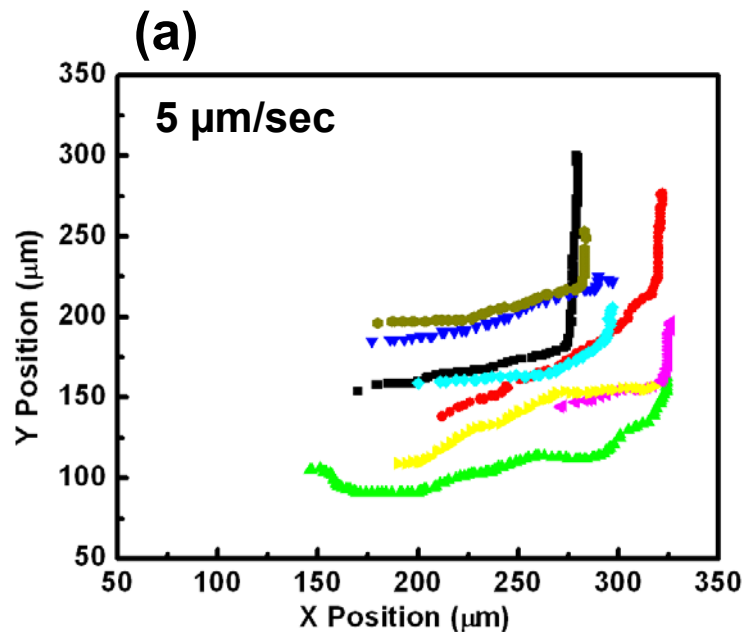


Fig. 5-9 (a)(b) Continuous particle sorting on 15- and 20- μm -diameter polystyrene beads. The dashed lines show the position of the optical guiding bars. (c) Trajectories of the beads entering the active area from the left of the image.

Although the light-induced DEP force is capable of particle transport at velocities of up to several hundred $\mu\text{m/s}$, the maximum sorting speed is limited by other factors such as the frame rate of the spatial light modulator, the frame rate of the CCD camera, and the processing time for the image analysis. In our current system, the frame rate of the spatial light modulator, 5 frames/s, is the limiting factor. As seen in Fig. 5-10, the slope of the particle trajectories increases when the stage translation rate is increased from 5 to 15 $\mu\text{m/s}$. When the stage speed increases beyond 20 $\mu\text{m/s}$, the particle trajectories are vertical lines. This means that the projected optical patterns do not affect the particle trajectories, as the refresh rate of the spatial light modulator is not fast enough to track the particles. The particles have already moved away from their original positions during the time it takes to load another manipulation image.



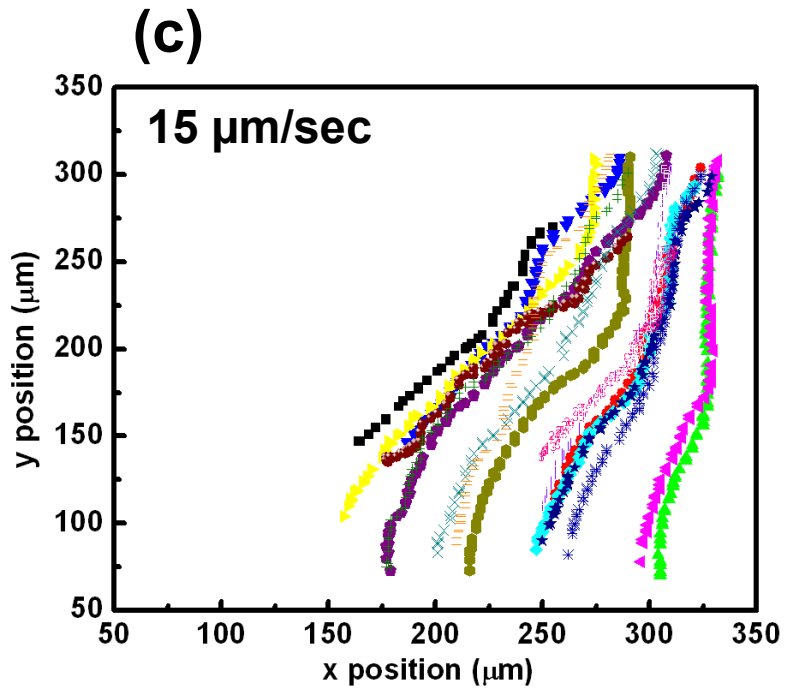
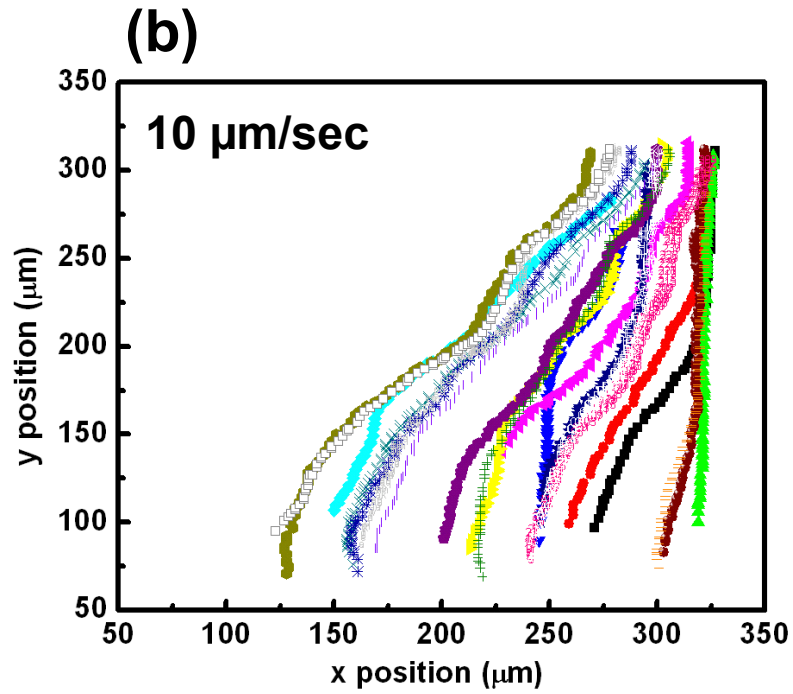


Fig. 5-10 The trajectories of the particles under stage translation rates of (a) $5 \mu\text{m}/\text{sec}$, (b) $10 \mu\text{m}/\text{sec}$, (c) $15 \mu\text{m}/\text{sec}$. The slopes of the trajectories increase dramatically as the stage speed increases from 5 to $15 \mu\text{m}/\text{s}$. For stage speed beyond $20 \mu\text{m}/\text{s}$, the particles are not

separated, and the trajectories are vertical. The refresh rate of the spatial light modulator is not fast enough to project the optical patterns at the appropriate positions when the particles are moving with a velocity greater than $20 \mu\text{m/s}$.

Figure 5-11 illustrates the sorting of HeLa cells. The stage carrying the OET device moves from the left to the right at a constant speed of $5 \mu\text{m/s}$. The cells enter the active manipulation area from the left side of the screen and trigger the SLM to switch on the pixels below the cells. The cells experience a positive DEP response at an ac frequency of 100 kHz , and are pulled to the bottom of the screen. In this experiment, the optical pixels projected on the OET device are triggered by the blue color of the cells. The trajectories of the cells are recorded in Fig. 5-11(c). The linear trajectories show that the cells experience a constant DEP force across the active area.

The blue color of the HeLa cells in Fig. 5-11 (a) and (b) are taken using the DIC mode of the microscope, and are not due to fluorescent signals. Fluorescent imaging is not performed due to a limitation of the OET device and the inverted microscope. To take fluorescent images, the photosensitive side of the OET device, which is not transparent, needs to be positioned as the upper surface so that it will not block the fluorescent signals from the bottom observation port. However, the cells will stay close to the bottom surface of the OET device due to gravitational force. The DEP forces are not strong enough to move the cells at the position far away from the photoconductive surface, as discussed in Chap 2. To solve this problem, an upright fluorescent microscope is required so the photoconductive surface is positioned as the lower surface, and the fluorescent signals propagate through the upper transparent ITO-coated glass.

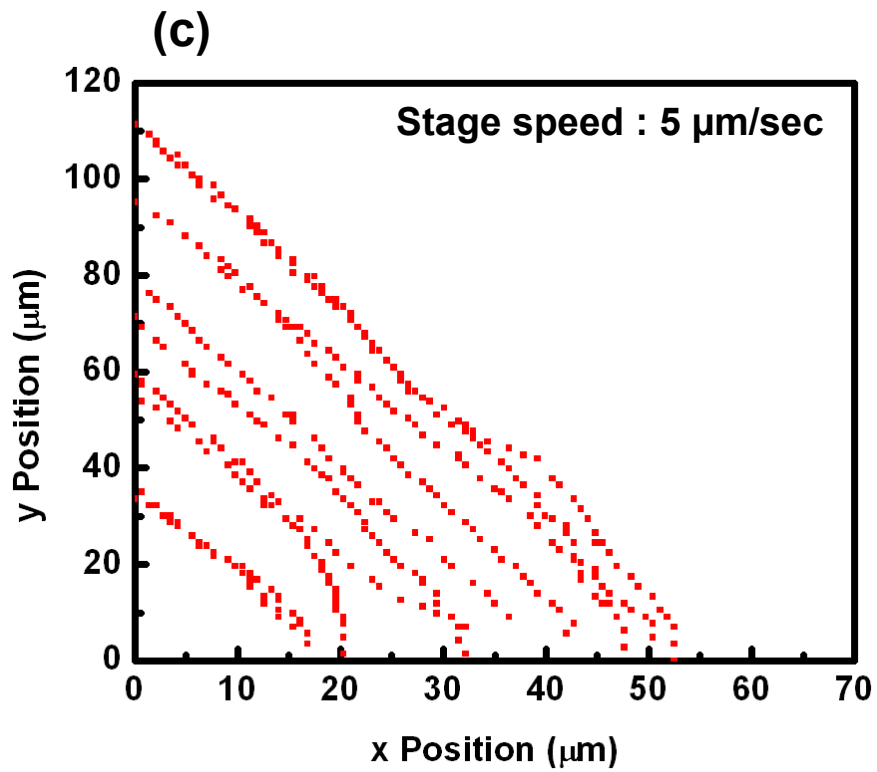
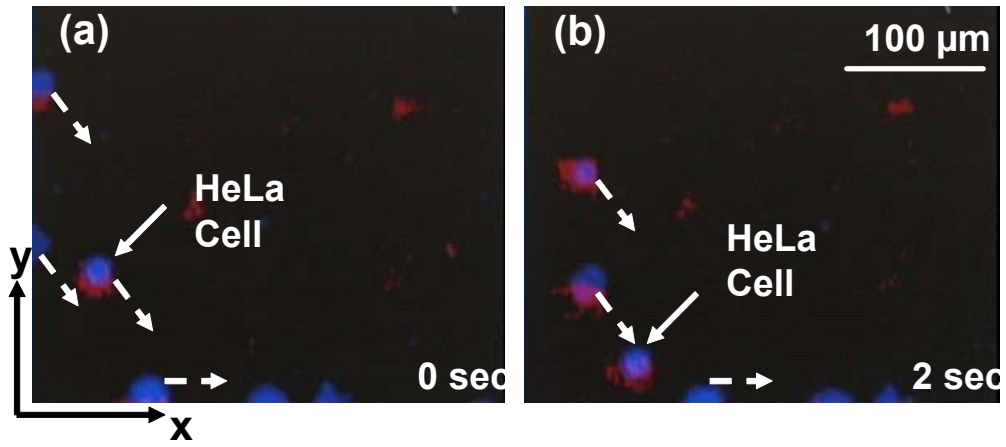


Fig. 5-11 The sorting of the HeLa cells based on color. (a), (b) HeLa cells concentrated at the bottom of the images. (c) Trajectories of the HeLa cells entering the active area from the left side of the image.

5.6. Reference

- [1] P. Y. Chiou, A. T. Ohta, and M. C. Wu, "Microvision activated optical manipulation on microscopic particles," in *Proceedings of IEEE Seventeenth Annual International Conference on Micro Electro Mechanical Systems*, pp. 682-685, 2005.
- [2] P. Y. Chiou, A. T. Ohta, and M. C. Wu, "Continuous optical sorting of HeLa cells and microparticles using optoelectronic tweezers," in *Proceedings of IEEE/LEOS International Conference on Optical MEMS and Their Applications (OMEMS' 05)*, pp. 83-84, 2005.

CHAPTER 6

LIGHT-PATTERNED AC ELECTROOSMOSIS FOR NANOPARTICLE MANIPULATION

6.1. Introduction

During OET manipulation, an abnormal motion of particles was observed in the low ac frequency regime, which cannot be explained by DEP forces. This phenomenon was also observed in many DEP experiments using patterned metal electrodes [1, 2]. A recently proposed theory has attributed it to the coupling of the tangential component of the electric field with the surface double layer charges on the electrodes, which creates a coulomb force at the liquid and electrode interface that drives fluidic flow [3-6]. This ac electrokinetic mechanism is called ac electroosmosis, and has been introduced in Chap. 1.

In OET manipulation, the majority of the applied voltage should drop across the liquid layer, creating an electric field gradient and generating DEP forces. However, at low ac frequencies, the electrical impedance of the electric double layer becomes significant and competes with that of the bulk liquid layer (Fig. 6-1). This results in a significant voltage drop across the double layer, charging accumulation at the surface of the light-patterned virtual electrode.

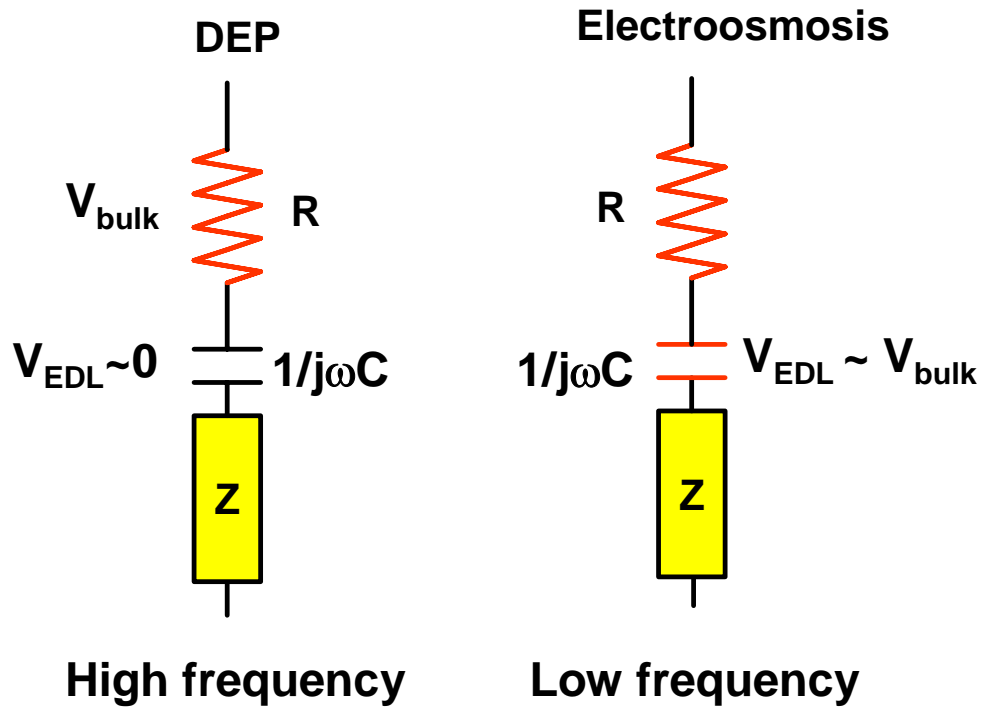


Fig. 6-1 Equivalent circuit model of OET including the effect of electric double layer at (a) high and (b) low frequencies. At low frequencies, a significant amount of the applied voltage will drop across the electric double layer.

6.2 Analytical Model of Light-Patterned AC Electroosmotic Flow

The magnitude and the direction of the driving force at the interface is determined by the polarity of the accumulated charges and the direction of the tangential electric field. To analyze the light-patterned ac electroosmosis flow on OET device, the tangential electric field and the zeta potential at the surface need to be determined, allowing the calculation of the slip velocity at the interface. The slip velocity was derived in Chap. 1, and is expressed as [7]

$$v_{slip} = -\frac{\varepsilon E_t \zeta}{\eta} \quad (6.1)$$

where v_{slip} is the slip velocity at the OET interface, ε is the permittivity of the liquid, E_t is the tangential component at the interface, ζ is the zeta potential as defined in Chap.1, and η is the viscosity of the liquid.

Figure 6-2 illustrates the direction of the driving force and the induced microfluidic flow pattern near the light-patterned virtual electrode. In the dark areas, both the surface charge and the electric field strength at the interface are small, as the electric impedance in the amorphous silicon layer dominates. As a result, the slip velocity at the dark area is small. At the center of the virtual electrode, the voltage is switched to the electric double layer and the bulk liquid layer. However, due to the symmetry of the virtual electrode, there is no lateral electric field in the center, resulting in a slip velocity of zero in the electrode center. At the edge of the virtual electrode, the fringing electric field has lateral component which can drive the surface charges in the direction indicated by Fig. 6-2. The slip velocity is strongest at the virtual electrode edge. The direction of the velocity vector points to the center of the virtual electrode, creating a microfluidic flow that is symmetrical about the virtual electrode. If a particle is near the virtual electrode, it will be brought into the center of the virtual electrode by the light-patterned microfluidic flow as a result of viscous force.

To analyze the slip velocity on the surface of the virtual electrode, we provide an analytical model based on the equivalent circuit of OET. As shown in Fig. 6-3 (a), the pattern of the electric field lines near the virtual electrode is highly non-uniform. The electric field lines originating from the ITO surface converge to a small virtual electrode on the photosensitive surface. Assuming the current flow in the lateral direction at the

interface double layer is negligible compared to the current flow in the vertical direction (which is reasonable because the double layer is very thin), a 1-D equivalent circuit model, as shown in Fig. 3-1(b), can be applied to simulate the response between two different electric field lines.

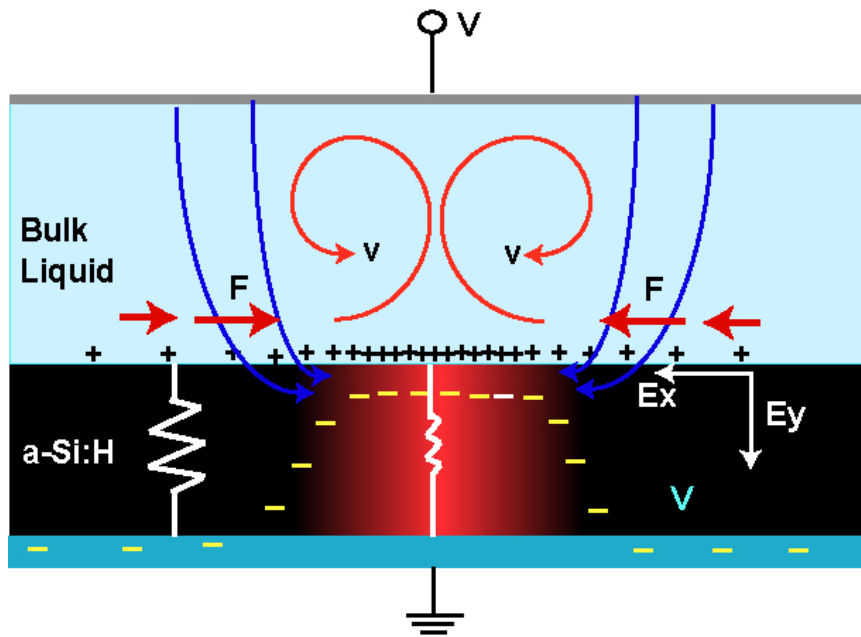


Fig.6-2 Illustration of the microfluidic flow pattern induced by the light-patterned ac electroosmosis mechanism.

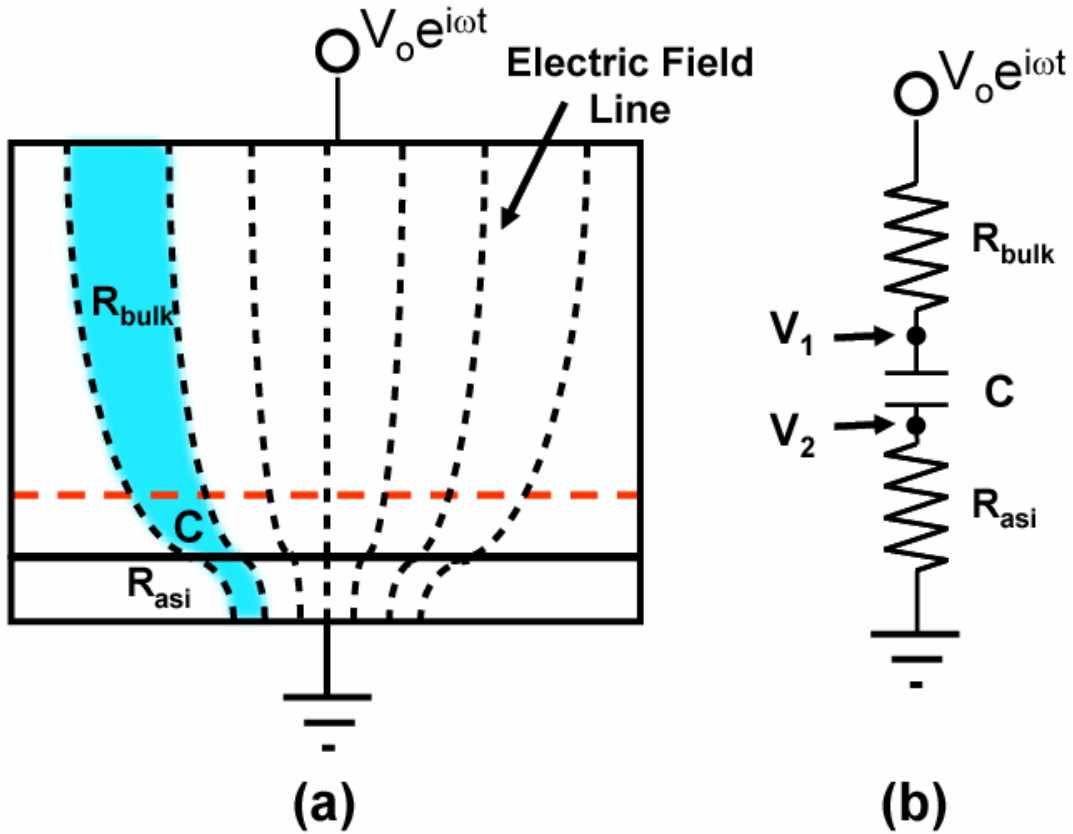


Fig. 6-3 Analytical model of light-patterned ac electroosmosis on OET. (a) The distribution of the electric field lines at the virtual electrode (b) Equivalent circuit model between two electric field lines.

To analyze the slip velocity under ac bias, the dc analytical expression of the slip velocity Eq. (6.1) is applied, except the tangential electric field and the zeta potential are now functions of time. The equation now becomes:

$$v_{slip} = -\frac{\varepsilon E_t \zeta}{\eta} = -\frac{\varepsilon E_t(t) \zeta(t)}{\eta} \quad (6.2)$$

where ε , η , E_t , ζ are the permittivity of the liquid, viscosity of the liquid, tangential electric field at the interface of the double layer and the bulk liquid layer, and the zeta

potential, respectively. The applied signal is assumed to be sinusoidal, and is represented by:

$$\begin{aligned} E_t(t) &= \text{Re}[E_{to}e^{i\omega t}] \\ \zeta(t) &= \text{Re}[\zeta_o e^{i(\omega t + \theta)}] \end{aligned} \quad (6.3)$$

where θ is the phase difference between E_t and ζ .

Substitute (6.3) into (6.2):

$$\begin{aligned} v_{slip}(t) &= -\frac{\varepsilon}{\eta} \text{Re}[E_{to}e^{i\omega t}] \times \text{Re}[\zeta_o e^{i(\omega t + \theta)}] \\ &= -\frac{\varepsilon}{\eta} E_{to} \zeta_o \left[\frac{e^{i\omega t} + e^{-i\omega t}}{2} \right] \times \left[\frac{e^{i(\omega t + \theta)} + e^{-i(\omega t + \theta)}}{2} \right] \\ &= -\frac{\varepsilon}{\eta} E_{to} \zeta_o \times \frac{1}{4} [e^{i(2\omega t + \theta)} + e^{-i(2\omega t + \theta)} + e^{i\theta} + e^{-i\theta}] \\ &= -\frac{\varepsilon}{\eta} E_{to} \zeta_o \times \frac{1}{2} [\cos(2\omega t + \theta) + \cos(\theta)] \end{aligned} \quad (6.4)$$

The result of (6.4) shows that the slip velocity consists of an ac term and a dc term; however, the net effect of the ac term is not observable in the kHz frequency range. The values of E_{to} , ζ_o , and θ can be calculated from the equivalent circuit model.

The zeta voltage is approximated by the voltage drop across the interface double layer capacitance and can be calculated as

$$\begin{aligned} \zeta(t) &= V_1 - V_2 = V_o e^{i\omega t} \left[\frac{1}{R + \frac{1}{i\omega C}} \right] \end{aligned}$$

$$= V_o Z_1 e^{i(\omega t + \phi_1)} \quad (6.5)$$

where

$$R = R_{bulk} + R_{asi}$$

$$Z_1 = \sqrt{\left[\frac{1}{1 + (\omega RC)^2}\right]^2 + \left[\frac{\omega RC}{1 + (\omega RC)^2}\right]^2}$$

$$\phi_1 = \tan^{-1}(\omega RC) \quad (6.6)$$

The electric field strength is not uniform along the electric field line – it is strongest at the photoconductive surface, and monolithically decays towards the ITO surface. $E_t(t)$ can be approximated as gV_{bulk}/L , where V_{bulk} is the voltage drop across the bulk liquid layer, L is the spacing between the photoconductive surface and the ITO glass, and g is the geometry factor of the liquid resistance along one specific electric field line. It considers the ratio of the length along the electric field line to the gap spacing L , the ratio of the converging areas from the ITO surface to the double layer boundary, and the ratio of the tangential component of the electric field at the double layer boundary. From the equivalent circuit model,

$$E_t(t) \sim g \frac{V_{bulk}}{L}$$

$$= g \frac{V_o}{L} e^{i\omega t} \left[\frac{R_{bulk}}{R + \frac{1}{i\omega C}} \right]$$

$$= g \frac{V_o}{L} Z_2 e^{i(\omega t + \phi_2)} \quad (6.7)$$

where

$$Z_2 = \sqrt{\left[\frac{\omega^2 C^2 R_{bulk} R}{1 + (\omega RC)^2}\right]^2 + \left[\frac{\omega R_{bulk} C}{1 + (\omega RC)^2}\right]^2} \quad (6.8)$$

$$\phi_2 = \tan^{-1}\left(\frac{1}{\omega RC}\right)$$

Substituting (6.5) and (6.7) into (6.2) results in

$$v_{slip} \sim -\frac{g\varepsilon V_o^2 Z_1 Z_2}{2\eta L} [\cos(2\omega t + \theta) + \cos(\theta)] \quad (6.9)$$

where $\theta = \phi_1 - \phi_2$ is the phase difference between the tangential electric field and zeta potential. If the ac term is neglected, a constant slip velocity is obtained, described by

$$v_{slip} \sim -\frac{g\varepsilon V_o^2 Z_1 Z_2}{2\eta L} \cos(\theta) \quad (6.10)$$

In the low ac frequency range, where $\omega RC \ll 1$, $\phi_1 \sim 0$, $\phi_2 \sim \pi/2$, and $\cos(\theta) = 0$, the slip velocity approaches 0. In the high ac frequency range, where $\omega RC \gg 1$, $\phi_1 \sim \pi/2$, $\phi_2 \sim 0$, and $\cos(\theta) = 0$, the slip velocity also approaches 0. The maximum slip velocity occurs at an optimal frequency where $\omega = 1/RC$, $\phi_1 = \phi_2$, and $\cos(\theta) = 1$.

In the dark areas, R is dominated by the dark resistance of the amorphous silicon layer, resulting in $\omega RC \gg 1$ and a very small slip velocity. At the center of the virtual electrode, the slip velocity equals to zero since there is no tangential electric field. Therefore, the driving force of the light-patterned ac electroosmotic flow is localized at the edges of the virtual electrode. This property gives rise to the possibility of generating a high-resolution microfluidic flow pattern for processing micro- and nano-scale particles.

6.3 Numerical Simulation of Light-patterned AC Electroosmotic Flow

The simulation of the light-patterned ac electroosmotic flow is divided into two parts. The first part is the calculation of the voltage drop across the double layer, the zeta potential, and the tangential electric field at the interface of the double layer and the bulk liquid. The second part is the calculation of the fluidic flow using the incompressible-flow Navier-Stokes equation using the boundary slip velocity calculated in the first part of the simulation.

The dc electrostatic model of the FEMLAB 3.0 software is used to simulate the electric field distribution and the voltage drop across the double layer. The double layer electrical impedance is converted to a resistance, $R_{EDL}=1/\omega C$, where ω is the radian frequency of the applied ac frequency and C is the double layer capacitance of the solution. Figure 6-4 shows the simulated electric field distribution and the electrical potential profile using the following parameters: thickness of the amorphous silicon layer = 1 μm , dark conductivity of the amorphous silicon layer = 10^{-8} S/m, double layer thickness = 10 nm, double layer dielectric constant = 78, liquid conductivity = 0.01 S/m, ac frequency = 8 kHz, gap between the top and the bottom electrode = 100 μm , gaussian beam spot size = 30 μm , peak conductivity of the amorphous silicon = 0.2 mS/m. The tangential electric field strength at the interface of double layer and the bulk liquid is extracted from Fig. 6-4(a), and is plotted in Fig. 6-5. The zeta potential, which is extracted from the voltage drop across the double layer in Fig. 6-4(b), is shown in Fig. 6-6. Multiplying the electric field strength in Fig. 6-5 with the zeta potential in Fig. 6-6 results in the slip velocity at different radial positions (Fig. 6-7).

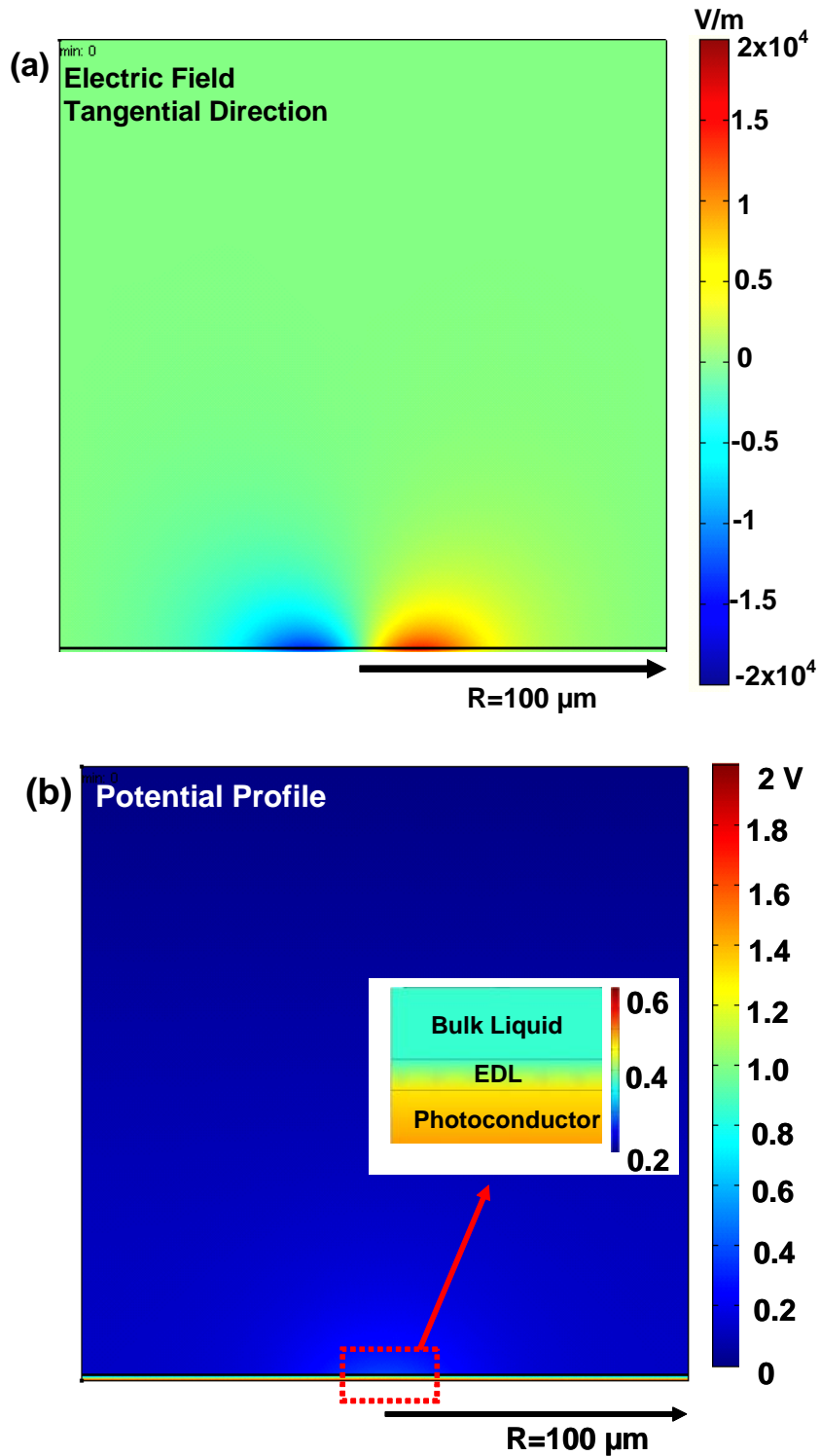


Fig.6-4 (a) Tangential electric field in the bulk liquid layer. (b) The potential profile in the bulk liquid layer. The potential drop across the electric double layer (EDL) is extracted to calculate the zeta potential at the interface.

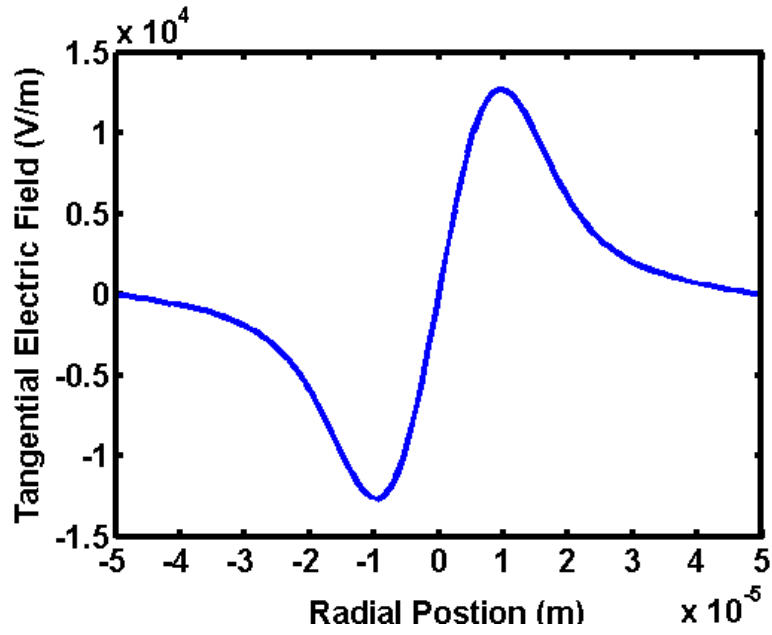


Fig.6-5 Radial distribution of the tangential electric field strength at the interface of the double layer and the bulk liquid.

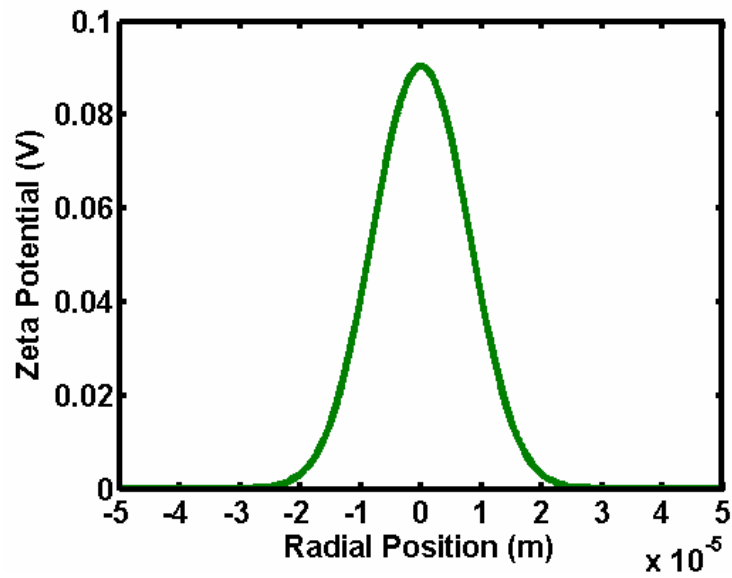


Fig.6-6 Radial distribution of the zeta potential at the interface between the photoconductive surface and the solution. This potential is approximated by the voltage drop across the double layer.

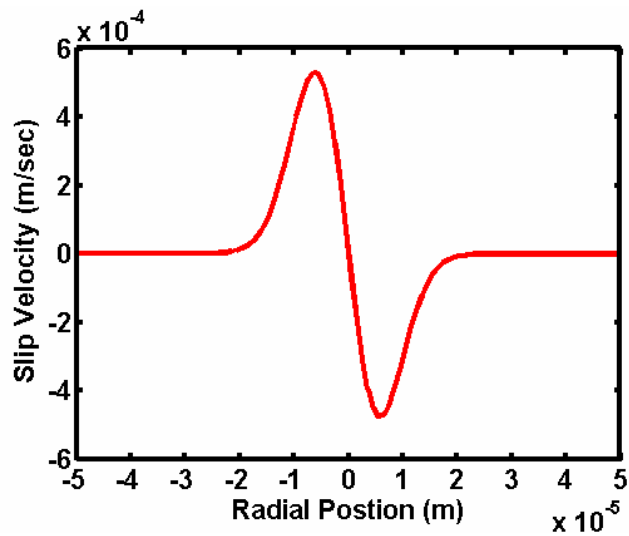


Fig.6-7 Radial distribution of the slip velocity at the surface of the light induced virtual electrode surface.

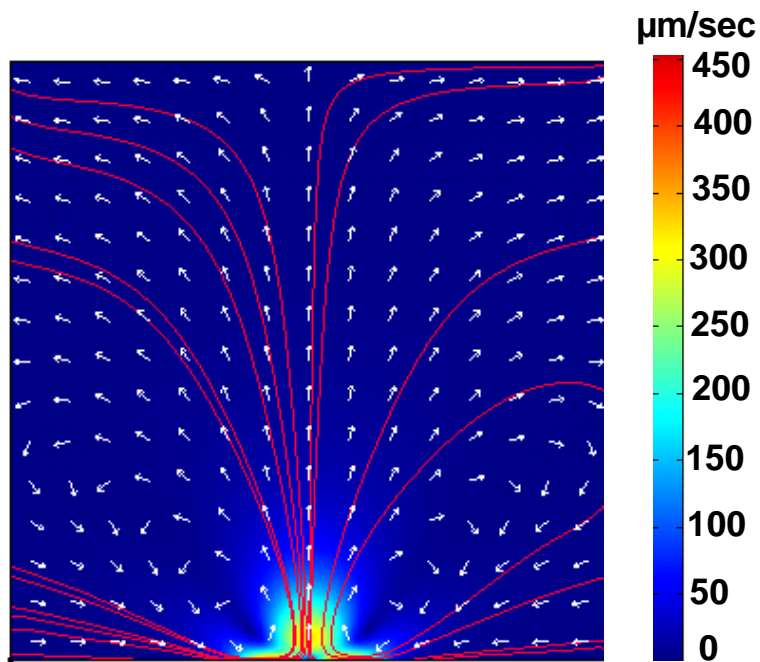


Fig.6-8 The streamlines of the light induced fluidic flow. A circulating fluidic flow symmetrical about the center of the virtual electrode is created by light-patterned ac electroosmosis.

To solve the microfluidic flow near the illuminated spot, the Navier-Stokes equation for incompressible flow is applied. The slip velocity distribution in Fig. 6-7 is used as the boundary condition at the double layer interface. The slip velocity at the ITO glass is assumed to be zero. Figure 6-8 shows the simulated flow pattern near the virtual electrode. The flow pattern is symmetric about the center of the virtual electrode. The liquid at the surface of the photoconductive layer flows into the virtual electrode and circulates upward at the center of the virtual electrode. This symmetric flow pattern forms a dead zone at the center of the virtual electrode surface. The experiment data in the next section will show that nanoparticles near the virtual electrode will be transported into the virtual electrode by the light-patterned fluidic flow, and remain in the dead zone of the flow pattern, resulting in a trapping function for nanoparticle manipulation.

Although the simulation uses a dc electrostatic model to calculate the electric field and the zeta potential, it provides a good approximation of the slip velocity acquired by the ac model. To estimate the error from the dc approximation, we use the equivalent circuit model proposed in section 6.2. Figure 6-9 shows the difference in the equivalent circuits of the dc and ac models. In the dc model, the impedance of the double layer capacitance is converted to a resistance. There is no phase difference between the tangential electric field and the voltage drop across the double layer.

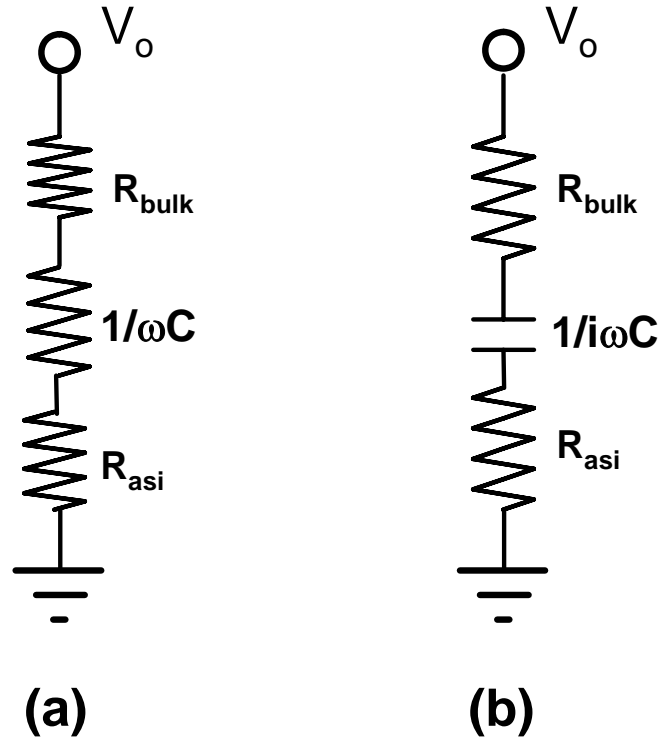


Fig.6-9 The dc equivalent circuit in our calculation. The double layer capacitance is represented by a resistance of $1/\omega C$. (b) The ac equivalent circuit model.

The slip velocity can be derived as the product of the zeta potential and the tangential electric field:

$$v_{slip,dc} = -\frac{\varepsilon}{\eta} E_t \xi \sim -\frac{g\varepsilon V_o^2}{\eta L} \times \frac{R_{bulk}\omega C}{(1 + R\omega C)^2} \quad (6.11)$$

where $R=R_{bulk} + R_{asi}$, ω is the applied angular frequency, and L is the gap between the top and the bottom surfaces. The slip velocity of the ac model is expressed by Eq. (6.10):

$$v_{slip,ac} \sim -\frac{g\varepsilon V_o^2 Z_1 Z_2}{2\eta L} \cos(\theta) \quad (6.12)$$

In the case where $R\omega C \gg 1$, Eqs. (6.11) and (6.12) become:

$$v_{slip,dc} \sim -\frac{g\varepsilon V_o^2}{\eta L} \times \frac{R_{bulk}}{R^2 \omega C} \quad (6.13)$$

$$v_{slip,ac} \sim -\frac{g\varepsilon V_o^2}{\eta L} \times \frac{R_{bulk}}{R^2 \omega C} \times \frac{\cos(\theta)}{2} \quad (6.14)$$

The magnitude of the slip velocities simulated by both models is small, since $R\omega C \gg 1$. However, the result of the ac model is smaller than that of the dc model, due to the extra phase term. When $R\omega C \gg 1$, the $\cos(\theta)$ term approaches zero. This occurs when R is large in the dark area or when ω is large in the high ac frequency regime.

In the case where $R\omega C \ll 1$, Eqs. (6.11) and (6.12) become:

$$v_{slip,dc} \sim -\frac{g\varepsilon V_o^2}{\eta L} \times R_{bulk} \omega C \quad (6.14)$$

$$v_{slip,ac} \sim -\frac{g\varepsilon V_o^2}{\eta L} \times R_{bulk} \omega C \times \frac{\cos(\theta)}{2} \quad (6.15)$$

The magnitude of the slip velocities simulated by both models is again small. Again, the slip velocity magnitude is smaller in ac model, due to the extra phase term. The $\cos(\theta)$ term also approaches zero when $R\omega C \ll 1$. This occurs when the ac frequency is low.

In the case where $R\omega C \sim 1$, Eqs. (6.11) and (6.12) become:

$$v_{slip,dc} \sim -\frac{1}{4} \frac{g\varepsilon V_o^2}{\eta L} \quad (6.15)$$

$$v_{slip,ac} \sim -\frac{1}{4} \frac{g\varepsilon V_o^2}{\eta L} \cos(\theta) \quad (6.16)$$

where $\cos(\theta) \sim 1$ when $R\omega C \sim 1$. In this case, the slip velocity calculated from both the ac and dc model is exactly the same. In this calculation, we assume $R \sim R_{\text{bulk}}$, which is the case when the virtual electrode is fully turned on and R_{asi} is much smaller than R_{bulk} .

In light-patterned ac electroosmotic flow, the slip velocity near the virtual electrode edge contributes most of the driving force for the fluidic flow. The optimal ac frequency is adjusted to result in $R\omega C \sim 1$ near the virtual electrode edge. Under this condition, the flow pattern produced by the dc model should be a good approximation to that of the ac model.

6.4 Light-patterned ac Electroosmosis for Nanoparticle Trapping

Particle trapping using DEP forces is effective when the size of the particles is large, as the magnitude of the DEP forces is proportional to the volume of the particles. To trap particles smaller than $1 \mu\text{m}$, a strong electric field gradient is needed to compensate for the reduced particle volume. In the OET devices, a stronger electric field can be achieved by reducing the gap between the top ITO glass and the bottom OET surface. However, this will increase the optical actuation power, because the impedance of the bulk liquid layer decreases as the gap is reduced. In Chap. 4, we have created an array of optical traps to transport single particles with diameters of $4.5 \mu\text{m}$. The trapping of particles smaller than $4.5 \mu\text{m}$ is not effective. One of the reasons is that the LED is not strong enough to fully turn on the virtual electrode, resulting in a non-maximal DEP force. Furthermore, the gap spacing between the top ITO and the bottom OET surface was $100 \mu\text{m}$ in this experiment. This is too large for strong enough electric field manipulating

smaller particles. However, we did observe the optical trapping of particles smaller than 4.5 μm , even down to the sub-micron range. When the OET is biased in an ac frequency range of 1 kHz to 10 kHz. This trapping phenomenon cannot be explained by DEP forces, and is due to the light-patterned ac electroosmotic flow described earlier.

Figure 6-9 demonstrates the parallel trapping and transporting of individual 2- μm polystyrene particles using light-patterned ac electroosmosis. The beads are swept into the bright spots by the light-actuated fluidic flow and trapped in the centers of the virtual electrodes. This is different from light-induced DEP, in which particles are trapped at the

The experiment setup is the same as in Fig. 4-1. Each bright spot consists of a single pixel of the DMD display; the spacing between bright pixels is 4 DMD pixels. On the OET surface, there are a total of 31,365 optical traps covering an area of 1.3 mm^2 . The spacing between virtual electrodes will affect the trapping forces. The microfluidic flows induced by two closely-positioned virtual electrodes will interfere with each other, reducing the flow speed into the center of the virtual electrodes. In this experiment, we apply a $2V_{pp}$, 1 kHz ac signal. The spacing between the top ITO glass and the bottom OET surface is 100 μm . The same optical pattern can also be used to trap single 1- μm particles. For particles smaller than 1 μm , more than one particle will be trapped in the same bright spot.

One interesting phenomenon is observed when multiple particles are concentrated to the center of the virtual electrode. The particles form a mono-layer crystalline structure on top of the OET surface as shown in Fig. 6-10. These crystalline structures are temporary, and are released when the optical pattern is turned off.

Light-patterned ac electroosmosis could be a powerful tool in manipulating nanoscopic particles. We have demonstrated the concentration of 500-nm polystyrene beads as shown in Fig. 6-10. The diameter of the virtual electrode is 30 μm , corresponding to 20 DMD pixels. The 500-nm particles cover half of the virtual electrode. Once filled, this area does not increase, even though the electrode remains on. We observed that the particles are still swept towards the center of the virtual electrode; however, they circulate upwards at the edges of the virtual electrodes instead of accumulating in the centers of the electrodes.

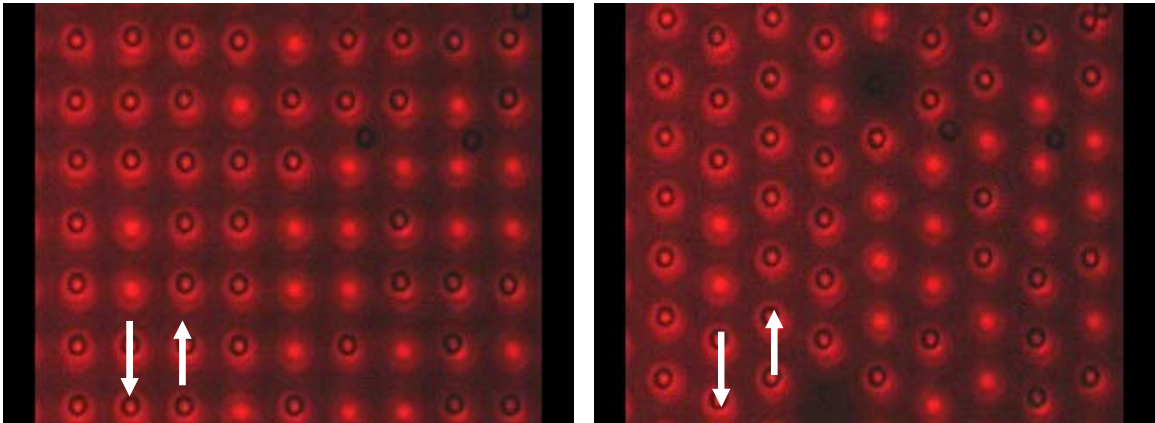


Fig. 6-9. Parallel trapping and transportation of 2- μm polystyrene beads on OET devices using light-patterned ac electroosmotic flow.

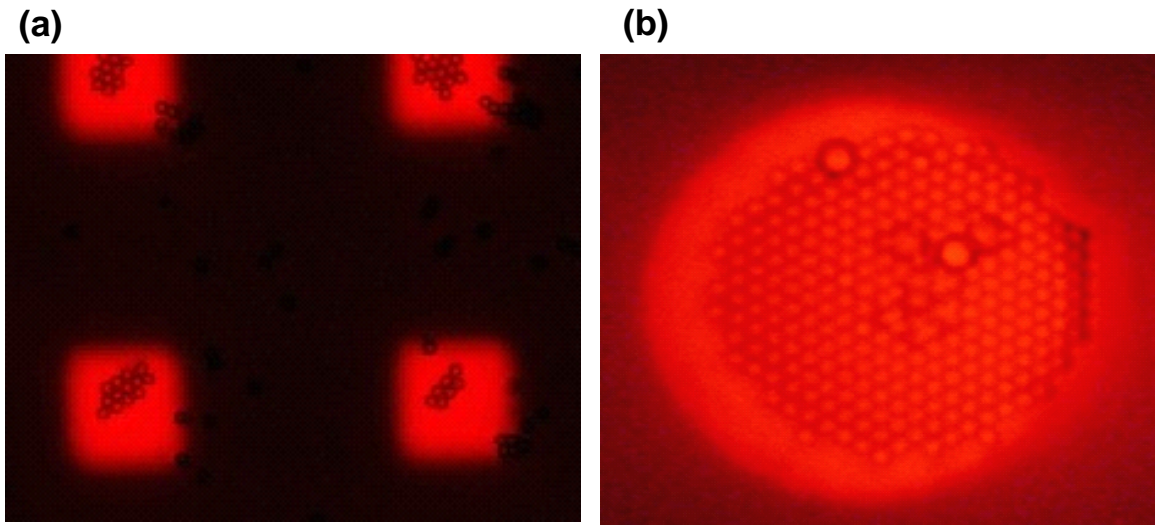


Fig. 6-10 The monolayer crystalline structure formed by the 2- μm polystyrene beads at the center of the virtual electrodes. The crystalline structure gradually disappears when the optical patterns are turned off.

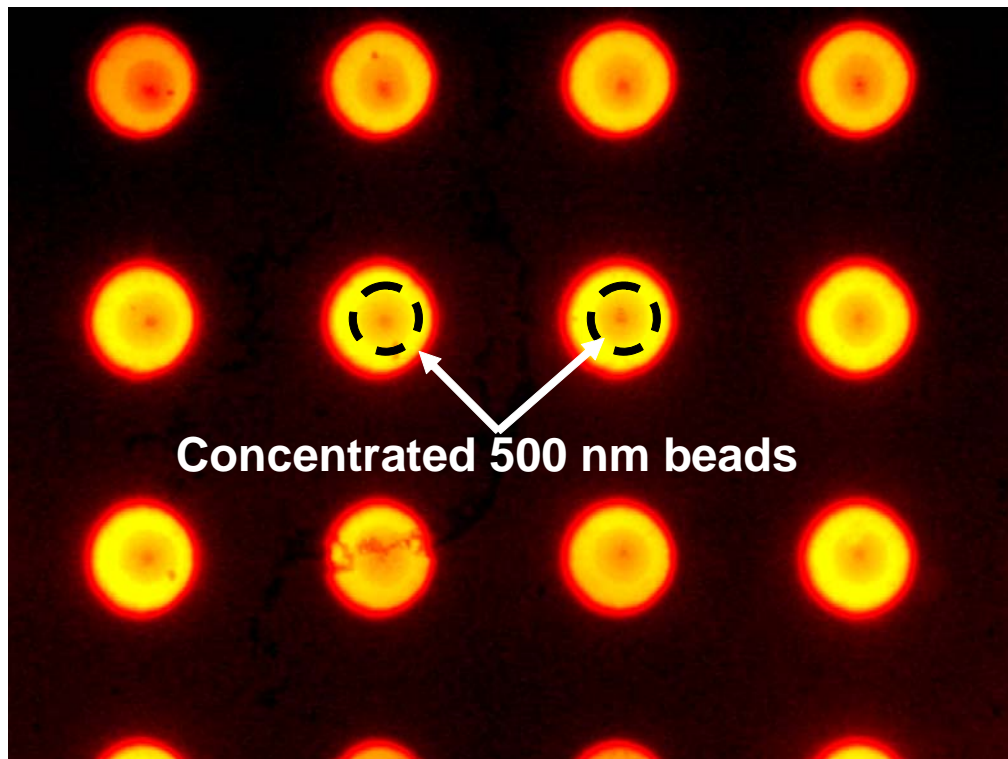


Fig. 6-11 Concentration of 500 nm polystyrene beads at the centers of the virtual electrodes.

To quantify the velocity of the light-patterned ac electroosmotic flow, the particle speed near the edge of the virtual electrode is measured at different ac frequencies. Due to limitations of our current CCD camera, the particle speed is measured at $\sim 17 \mu\text{m}$ radial distance from the center of a circular virtual electrode with a radius of $15 \mu\text{m}$. The particle velocity inside the edge of the virtual electrode is greater than $100 \mu\text{m/s}$, which is too fast to be captured by our current CCD camera. Figure 6-12 shows the measured result using $1\text{-}\mu\text{m}$ beads under a $4V_{pp}$ ac bias. The flow speed is frequency dependent as predicted by the analytical model in Sec. 6-2. The optimal frequency shown here is around 8 kHz . The data at frequencies above 12 kHz is not collected, since the DEP force become more effective at these higher frequencies, and starts to compete with the decreasing forces from light-patterned fluidic flow.

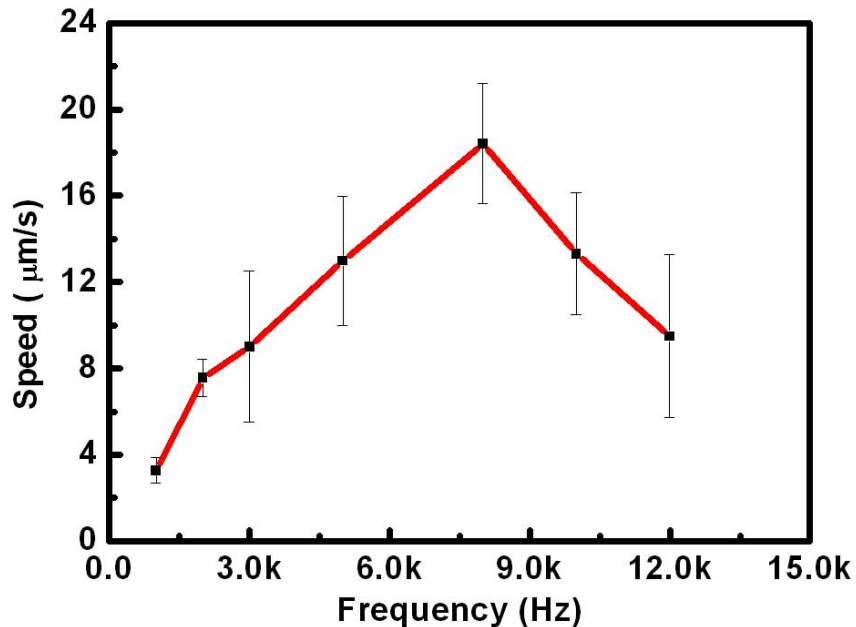


Fig. 6-12. The frequency response of the light-patterned ac electroosmotic flow near the edge of the virtual electrode.

6.5 Reference

- [1] A. Ramos, H. Morgan, N. G. Green, and A. Castellanos, "Ac electrokinetics: a review of forces in microelectrode structures," *Journal Of Physics D-Applied Physics*, vol. 31, pp. 2338-2353, 1998.
- [2] T. Muller, A. Gerardino, T. Schnelle, S. G. Shirley, F. Bordoni, G. DeGasperis, R. Leoni, and G. Fuhr, "Trapping of micrometre and sub-micrometre particles by high-frequency electric fields and hydrodynamic forces," *Journal Of Physics D-Applied Physics*, vol. 29, pp. 340-349, 1996.
- [3] N. G. Green, A. Ramos, A. Gonzalez, H. Morgan, and A. Castellanos, "Fluid flow induced by nonuniform ac electric fields in electrolytes on microelectrodes. III. Observation of streamlines and numerical simulation," *Physical Review E*, vol. 66, 2002.
- [4] A. Gonzalez, A. Ramos, N. G. Green, A. Castellanos, and H. Morgan, "Fluid flow induced by nonuniform ac electric fields in electrolytes on microelectrodes. II. A linear double-layer analysis," *Physical Review E*, vol. 61, pp. 4019-4028, 2000.
- [5] N. G. Green, A. Ramos, A. Gonzalez, H. Morgan, and A. Castellanos, "Fluid flow induced by nonuniform ac electric fields in electrolytes on microelectrodes. I. Experimental measurements," *Physical Review E*, vol. 61, pp. 4011-4018, 2000.
- [6] A. Ramos, A. Gonzalez, A. Castellanos, H. Morgan, and N. G. Green, "Fluid flow driven by a.c. electric fields in microelectrodes," in *Electrostatics 1999*, vol. 163, Institute Of Physics Conference Series, 1999, pp. 137-140.
- [7] R. J. Hunter, *Zeta Potential in Colloid Science*. New York: Academic Press Inc., 1981.

CHAPTER 7

Conclusion

We have proposed a novel optoelectronic tweezers (OET) that enables massively parallel optical manipulation of single cells, micro-particles, and nano-particles. It is realized by using light to pattern virtual electrode on a photoconductive surface and induce the dielectrophoretic force. Since the optical energy is not directly converted to the mechanical force, as in optical tweezers, OET can operate at extremely low optical power. We have demonstrated optical manipulation of microscopic particles with light intensity as low as 1 W/cm^2 , which is five orders of magnitude less than that in optical tweezers techniques. This opens up the possibility of optical manipulation using cheap incoherent light source such as a lamp or a LED.

Integrating a DMD spatial light modulator with 1024×768 pixels array, we can create 15,000 particle traps on a $1.3 \times 1 \text{ mm}^2$ area using a single LED light bulb. The resolution of the optically patterned virtual electrode is limited by the optical diffraction limit of the optics used for image projection and can achieve sum-micron resolution. Since the optical pattern is real-time reconfigured on the spatial light modulator, dynamic electric field landscape of any arbitrary shape can be created to perform multi-step and integrated manipulation functions. Further integration of OET with image feedback system, a fully automatic optical manipulation system can be achieved for high throughput manipulation.

The concept of light-addressed virtual electrodes can be extended to other electrokinetic mechanisms. We have demonstrated an light induced ac electroosmosis mechanism to pattern localized microfluidic flow near each virtual electrode. Nanoscopic particles, which is difficult to manipulate using dielectrophoretic forces, can be manipulated in the low flow region. This mechanism allows us to generate 31,000 single particle traps to transport 1- μm beads in parallel. We have also demonstrated the concentration of 500-nm particles. This technology has the potential to manipulate many interesting nanoscopic particles such as quantum dots, carbon nanotubes nanowires, and biomolecules such as DNAs and proteins.